Photophysical Properties of Rare-Earth Cluster-Based Metal–Organic Frameworks

Zvart Ajoyan

A Thesis

In

The Department

Of

Chemistry and Biochemistry

Presented in Partial Fulfillment of the Requirements

For the Degree of Master of Science (Chemistry) at

Concordia University

Montreal, Quebec, Canada

December, 2021

CONCORDIA UNIVERSITY

SCHOOL OF GRADUATE STUDIES

This is to certify that the thesis prepared

By: Zvart Ajoyan

Entitled: Photophysical Properties of Rare-Earth Cluster-Based Metal–Organic Frameworks

and submitted in partial fulfillment of the requirements for the degree of

Master of Science (Chemistry)

complies with the regulations of the University and meets the accepted standards with respect to originality and quality.

Signed by the final examining committee:

Dr. Melissa Passarelli _____ Chair

Dr. Rafik Naccache _____ Examiner

Dr. Marek B. Majewski _____ Examiner

Dr. Ashlee J. Howarth _____ Supervisor

Approved by _____

       Dr. Yves Gelinas, Graduate Program Director, Chemistry and Biochemistry

_____ 20___   _____

       Dr. Pascale Sicotte, Dean, Faculty of Arts and Science

Abstract

Photophysical Properties of Rare-Earth Cluster-Based

Metal–Organic Frameworks

Zvart Ajoyan

The work described herein explores the field of metal–organic frameworks (MOFs) with a particular emphasis on rare-earth (RE) cluster-based MOFs. MOFs are materials that are of interest due to their permanent porosity, high surface areas, and tunable structures. This thesis focuses on three different MOFs: RE-UiO-66 (UiO = University of Oslo), RE-CU-10 and RE-CU-27 (CU = Concordia University). The synthesis, characterization, and photophysical properties of these MOFs are presented.

Chapter 2 explores tuning of the RE-UiO-66 platform by synthesizing and characterizing mono-, bi- and tri-metal RE-UiO-66 analogues where RE = Tb(III), Gd(III), and Eu(III), ultimately leading to the formation of a white light emitting MOF. Furthermore, a study of the photophysical properties of this series of MOFs is conducted and as a proof of concept, Tb:Gd:Eu-UiO-66 is deposited on a UV light emitting diode (LED), leading to a white light emitting diode (WLED).

Chapter 3 describes a facile route for modulating the photoluminescent and radioluminescent properties of Tb(III) cluster-based MOFs. By using Tb(III)-cluster nodes as X-ray attenuators, and organic linkers with varying excited state energies as sensitizers, MOFs with metal-based, linker-based, and metal+linker-based photo- and radioluminescence are reported.

Acknowledgements

First and foremost, I would like to thank my supervisor, Dr. Ashlee J. Howarth who relentlessly supported me and made this all possible. With her kindness, patience, knowledge and overall great attitude and outlook on absolutely everything, she has been there to encourage me, guide me and keep me on the right track. She has been my go-to person for the last 2 years and I would be lost without her. I would not have known my love of MOFs if it wasn't for her, and I count my lucky stars every day for having stopped by her office in 2018. She has truly transformed my life and I am deeply indebted to her.

To Rafik Naccache, I am thankful for the guidance and advice. To Marek Majewski, who has played a pivotal role in my success with his helpful suggestions and always being available to advise me, I thank you for being a mentor to me, and I am honoured to have worked so closely.

Paola, with whom I started this journey with, and ending it with, I will be forever grateful for her friendship. I would like to thank Rafa for always attending to my needs, listening to me, and sharing his visions with me. He is the truest gem, and I could not have done this without him! With his fun-loving energy, Hudson has been there to brighten my days and help me out with everything I have needed. I cannot thank him enough. I would like to thank Chris for literally always being helpful, especially when a box of Pringles is involved. It has been wonderful having him as my fumehood neighbour. I am thankful for Victor for his kindness and willingness to help. It has not gone unnoticed by me. I would like to thank Felix, for sharing his love of reality TV with me; Lars for understanding me the most; Amna, for are always being there to lend a helping hand; Ximena for her bright and happy presence; Samantha, for always being so kind and friendly; Paria for always being positive and motivating; and Joey, from the beginning he made me believe that I could do it, and he was right. Thank you for supporting me.

I would like to thank all the Howarth and Majewski members for being like family to me. They have created this wonderful working environment and I could not have imagined a better group of people to be around.

To Hatem, who has been there for every step of this journey. He is always the first one we ask for help and is always willing and ready.

To Marina, Harout, Avo, Nene, Magy, the Bou-merhi's and the rest of my family and friends, you have supported me over these last two years, and I could not have done it without you.

To my sweet Benji, you kept reminding me that long morning walks are needed to start the day off right, and you are the MVP in all of this.

I would like to acknowledge every single person I have encountered during my master's degree as any experience that has come my way has led to my interpersonal growth and to character building.

Overall, the successful completion of my master's degree would not have been possible without everyone who has helped me and has been on my path. They all hold a special place near and dear to my heart and I will forever be grateful for all of them. I would like to say that I did it, but, in reality, *we* did it!

Contribution of Authors

In all chapters, Dr. Ashlee J. Howarth acted in a supervisory role. Chapter 3 involved a collaboration with Gabrielle A. Mandl and Dr. John A. Capobianco from Concordia University.

Chapter 2 is an advanced project which will soon be submitted to a peer-reviewed journal. I am the primary author of this work. Hudson A. Bicalho performed PXRD on all of the samples and SEM-EDS analysis. Rafael P. Donnarumma performed the synthesis of single-crystals of Gd-UiO-66 and Eu-UiO-66. Dr. Hatem M. Titi from McGill University performed single-crystal X-ray structure analysis on Gd-UiO-66(F), Gd-UiO-66(O), Eu-UiO-66(F) and Eu-UiO-66(O).

A version of chapter 3 is pending submission to a peer-reviewed journal as: Ajoyan, Z.; Mandl, G. A.; Donnarumma, P. R.; Quezada-Novoa, V.; Bicalho, H. A.; Titi, H. M.; Capobianco, J. A.; Howarth, A. J. *ChemRxiv*, **2021**, 10.26434/chemrxiv-2021-72ghc. I am the primary author of this work and Gabrielle A. Mandl is co-first author. Gabrielle A. Mandl performed the photoluminescence and radioluminescence experiments on the MOFs. Rafael P. Donnarumma performed the synthesis of initial batches of bulk and single crystals of Tb-UiO-66. Hudson A. Bicalho performed SEM imaging. Victor Quezada-Novoa performed the synthesis of the H_4TBAPy linker and Tb-CU-10. Dr. Hatem M. Titi performed single-crystal X-ray structure analysis of Tb-UiO-66(F), Tb-UiO-66(O), Tb-CU-27(F), Tb-CU-27(O) and Tb-CU-10(F).

Table of Contents

List of Figures

List of Tables

List of Abbreviations

^{1}H-NMR	Proton nuclear magnetic resonance
2,6-DFBA	2,6-Difluorobenzoic acid
2-FBA	2-Fluorobenzoic acid
3D	3-dimensional
BET	Brunauer Emmett Teller
BP	Boiling point
CIE	Commission International d'Eclairage
CSD	Cambridge Structural Database
d6R	Double six-membered ring
DCDPS	4,4'-dicarboxydiphenyl sulfone
DCM	Methylene chloride
DEF	*N,N*-Diethylformamide
DMA	*N,N*-Dimethylacetamide
DMF	*N,N*-Dimethylformamide
DMSO	Dimethyl sulfoxide
DRIFTS	Diffuse reflectance infrared Fourier transform spectroscopy
DR-UV-Vis	Diffuse reflectance ultraviolet visible
EDS	Electron-dispersive X-ray spectroscopy
ET	Energy transfer
EtOH	Ethanol
H$_2$BDC	1,4-benzendicarboxylic acid
H$_2$BPDC	biphenyl-4,4'-dicarboxylic acid
H$_4$TBAPy	1,2,4,5-tetrakis(p-benzoate)-pyrene
ICP-MS	Inductively coupled plasma mass spectrometry
ISC	Intersystem crossing
KBr	Potassium bromide
LED	Light emitting diode
Ln-MOF	Lanthanide metal–organic framework
MBB	Molecular building block

MeOH	Methanol
MOF	metal–organic framework
N$_2$	Nitrogen
NLDFT	Non-local density functional theory
PXRD	Powder X-ray diffraction
RCSR	Reticular chemistry structural resource
RE	Rare-earth
RE-MOF	Rare-earth metal–organic framework
RGB	Red green blue
SBU	Secondary building unit
ScCO$_2$	Supercritical carbon dioxide
SCXRD	Single crystal X-ray diffraction
SEM	Scanning Election Microscopy
T$_1$	Triplet excited state
TCPB	1,2,4,5-Tetrakis(4-carboxyphenyl)benzene
TCPP	tetrakis(4-carboxyphenyl)porphyrin
TGA	Thermogravimetric Analysis
UV-Vis	Ultraviolet-visible
WLED	White light emitting diode
YAG	Yttrium aluminum garnet

Chapter 1

Introduction

1.1. Metal–Organic Frameworks (MOFs)

Over the past three decades, there have been tremendous advances in the field metal–organic frameworks (MOFs) and they have received notable attention owing to their very interesting structural features. In 1989, Hoskins and Robson[1] designed and synthesized one of the first MOF-like materials, and in hindsight paved the way for the thousands of MOF structures that have followed.[2] The structure presented by Hoskins and Robson showed a scaffolding-like network, which contained an infinite and crystalline framework, with close resemblance to zeolites. To follow, Yaghi named the materials metal–organic frameworks, and described their synthesis through a hydrothermal method, which is still commonly used today.[3] In this work, they found that the crystalline materials contained extended channel systems, similar to the observations of Hoskins and Robson.[1, 3] That same year, Yaghi *et al.* studied MOFs as adsorptive materials and more specifically for the selective binding of aromatic compounds.[4] This led to the understanding that the adsorption of organic molecules or ions was not only shape- and size-selective, but that MOFs could be rationally designed in terms of shape, size, and pore functionalization leading to better performing materials. In that same regard, a 3-dimensional (3D) MOF with channeling cavities demonstrated reversible adsorption of gases, all while maintaining its structural integrity, as no structural deformation or collapse of the framework occurred.[5] Furthermore, MOF-5, containing the Zn(II) and 1,4-benzenedicarboxylate (BDC) building block, was found to have high crystallinity, structural stability, porosity and a relatively higher surface area in comparison to zeolites.[6]

These initial finding established the groundwork of MOFs. MOFs are a class of crystalline hybrid materials comprised of inorganic nodes and organic linkers, held together by strong coordination bonds (Figure 1.1). The inorganic nodes can be ion, chain or cluster nodes where the metal can be from the *s*-,[7, 8] *p*-,[9, 10] *d*-,[11-14] or *f*-block[15, 16] in the periodic table. When the inorganic building blocks are bridged to the multidentate organic linkers, they can form 2- or 3-dimensional structures with the ability to form pores, possess high surface area, and a high degree of structure tunability. As such, MOFs have received notable attention for their use in gas storage and separation,[17] catalysis,[12] luminescent sensing,[18] and biomedical imaging,[19] amongst others.
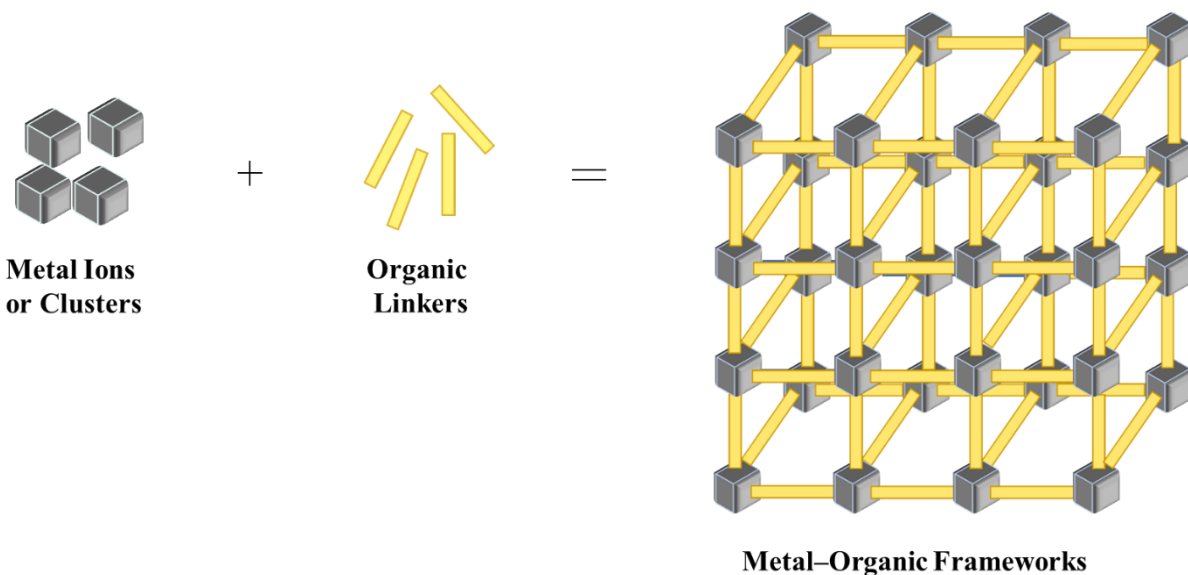
Figure 1.1. Schematic representation of the assembly of a MOF.

1.2. Fundamental Principles of MOF Synthesis

1.2.1. Reticular Chemistry

Given that the formation of MOFs requires an inorganic node and a multidentate organic linker, these building blocks can be strategically selected for the design, and ultimately the synthesis of, a predetermined structure giving rise to the concept of reticular chemistry which was introduced by Yaghi and O'Keeffe.[20] In their definition of reticular chemistry, also known as reticular synthesis, a logical approach is taken to identify the necessary building blocks to form predetermined robust structures, where there is the possibility of building the same net with different building blocks.[21-23] For example, carboxylate functionalities are often used to chelate metal ions, thus forming rigid metal-oxygen bonds throughout the network. This can also be seen in MOF-5, where the MOF has high structural stability owing to the network formed by the cationic clusters strongly bonded to the BDC linker.[6, 24] The notion of reticular chemistry is instilled to encourage materials design and to consider structures as a matter of geometry rather than only energetics.[25]

1.2.2. Topology

With MOFs, it is necessary to appoint a descriptor to the connectivity and the geometry of the network, and that can be referred to as topology. The net topology of a MOF can be found in the reticular chemistry structural resource (RCSR) database where it is depicted by a 3 letter code

written in lower case letters and bolded.[24] Every MOF has a topology, where depending on the networks' vertices and edges, it can be assigned one of the many possible topologies.[24, 26, 27] Another concept known as isoreticular chemistry refers to isostructural MOFs where the pore dimensions can be tuned and the chemical functionalities can be modified within the same topology. For example, the **fcu** topology (Figure 1.2) is associated with UiO-66 and UiO-67 (UiO = University of Oslo), where the MOFs only differ in their organic linkers. UiO-66 has BDC as its linker, and UiO-67 has biphenyl-4,4'-dicarboxylate (BPDC) as its linker, thus extending the pore size leading to the formation of a different MOF, while maintaining the same topology.
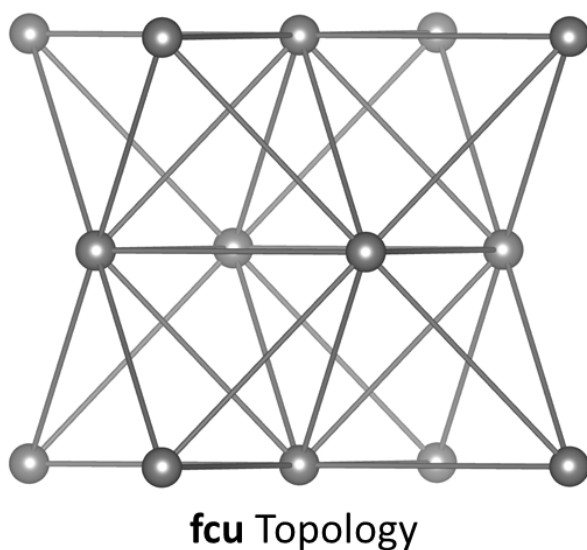
fcu Topology

Figure 1.2. Schematic of the **fcu** topology, which can be found in both UiO-66 and UiO-67.

1.3. Rare-Earth (RE) Metal–Organic Frameworks (MOFs)

The introduction of rare-earth (RE) metals in MOFs has allowed for the creation of a new subset in the MOF field termed RE-MOFs. Rare-earth metals include yttrium, scandium and the 15 lanthanoids from the *f*-block (Figure 1.3) Rare earth metals exist primarily in the +3 oxidation state with coordination numbers of 8 or 9.[28] In the +3 oxidation state, Sc and Y have similar coordination chemistry as lanthanoids. RE metals possess unique electronic, magnetic, and catalytic properties, which can be attributed to their electronic configuration where they have partially filled *f*-orbitals.[29, 30] In addition to these unique characteristics, RE-MOFs still possess the

same properties as all MOFs, meaning that they have the ability to form voids that can be tuned, possess high surface areas, and have accessible Lewis acidic binding sites.[31]
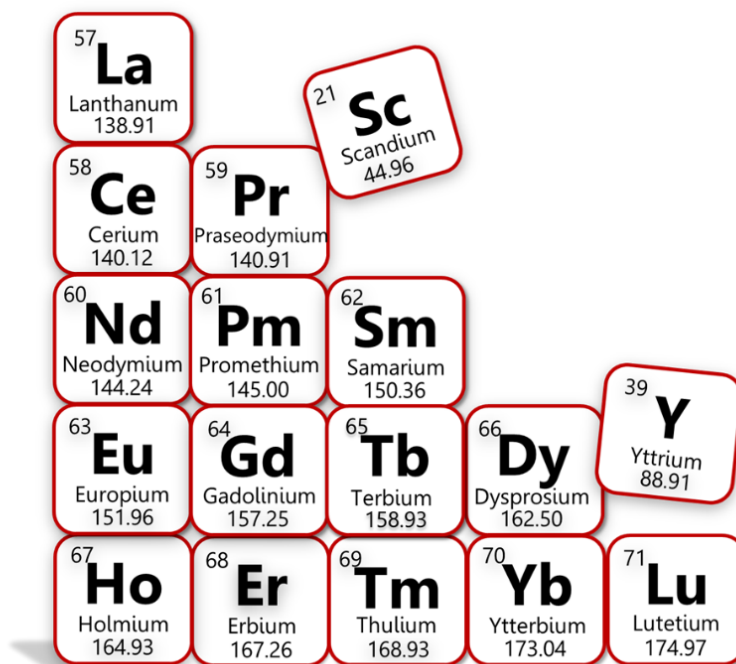
Figure 1.3. The rare-earth (RE) elements which include scandium, yttrium, and the lanthanoids from the *f*-block.

In the formation of RE-MOFs, the MOF nodes can be ion-nodes, chain-nodes,[32-44] or cluster-nodes. Cluster-nodes in a MOF can be multinuclear such as di-,[6, 45-52] tri-,[53-58] tetra-,[59-65] hexa-[15, 66-74] hepta-,[75, 76] and nonanuclear.[66, 77-80] In the work presented herein, cluster-based RE-MOFs will be the focus, with particular attention to those comprised of hexanuclear (RE_6) and nonanuclear (RE_9) clusters.

Common to all RE_6 and RE_9-MOF synthetic procedures is the use of 2-fluorobenzoic acid (2-FBA) or 2,6-difluorobenzoic acid (2,6-DFBA)[81] as a structure directing agent to aid in the generation of the RE cluster, an approach pioneered by Eddaoudi *et al.* in 2013.[15] It can be speculated that the hydrophobic nature of fluorine aids in the formation of the RE cluster. In literature, the majority of reports suggest that the cluster is a RE-oxy/hydroxy cluster, however more recently, it has been suggested that the cluster in fact contains bridging fluorine atoms as opposed to oxygen atoms.[82]

1.3.1. RE(III)-Hexanuclear Cluster-Based MOFs

Rare-earth metals such as Y(III), La(III), Nd(III), Eu(III), Gd(III), Tb(III), Dy(III), Ho(III), Er(III), Tm(III), Yb(III), and Lu(III) have been used in the synthesis of hexanuclear cluster-based MOFs (Figure 1.4).[31] Related RE_6 clusters have been isolated with six or eight nitrate capping ligands (as opposed to the normally observed twelve capping ligands), and these discrete clusters contain a μ_6-O^{2-} at the center of the octahedron constructed by the RE metals, different from the cluster observed in RE_6-MOFs.[83-85] Using linear ditopic linkers and 2-FBA, Eddaoudi *et al.* showed the first examples of RE_6-MOFs (RE = Y(III), Eu(III), and Tb(III)) with **fcu** topology.[15] The linkers in these examples include dicarboxylates as well as asymmetric linkers containing one carboxylate and one tetrazolate functionality. Following this report, a small library of RE_6-MOFs with **fcu** topology and varying ditopic linkers has now been reported.[81, 86-93]
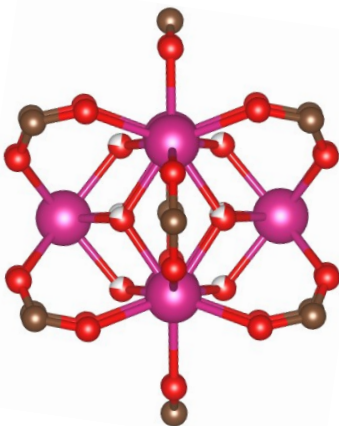
Figure 1.4. Schematic representation of a hexanuclear (RE_6) cluster. RE = pink, O = red, C = brown.

RE_6-MOFs are of interest, and have been studied, for a wide variety of potential applications. In addition to having similar features to Zr_6-MOFs such as thermal and chemical stability, Lewis acidic metal nodes, tunable topologies, and permanent porosity, rare earth elements impart the added feature of metal-based luminescence properties. Thus far, RE_6-MOFs have been studied for potential applications in gas storage,[15] chemical separations,[66, 74, 86, 89, 94, 95] catalysis,[91, 92, 96, 97] ion-exchange,[87] bioimaging,[81, 90] sensing,[91] and magnetic refrigeration.[93] The RE_6-**fcu**-MOF platform, for example, has been explored for potential applications in bioimaging. Near-IR emitting RE metals have some notable advantages for bioimaging since the sharp NIR emission bands with long emission lifetimes can be separated from tissue autofluorescence. Sava

Gallis *et al.* tuned the composition of Eu(III), Nd(III), and Yb(III) in a RE$_6$-**fcu**-MOF comprised of 2,5,-dihydroxyterephthalic acid linkers to achieve a series of MOFs demonstrating emission wavelengths ranging from 590-1325 nm, a wavelength range relevant to biological imaging.[90] By incorporating the LDS 750 chromophore in the pores of Yb$_6$-**fcu**-MOF with 1,1'-biphenyl-4,4'-dicarboxylic acid (BPDC) linkers, Rosi *et al.* obtained a material that absorbs (600-800 nm) and emits (980 nm) in the biological diagnostic window (650-1450 nm).[81]

Using the same 12-connected RE$_6$-cluster node, but employing tetratopic quadrangular linkers, a series of RE$_6$-MOFs (RE = Y(III), Tb(III), Yb(III)) with **ftw** topology were synthesized.[74, 94] It should be noted that RE$_6$-MOFs comprised of 12-connected nodes are anionic materials, often with the charges balanced by the incorporation of dimethylammonium cations generated by the decarbonylation and subsequent protonation of the DMF reaction solvent.

In a rare example, using conditions known to generate the RE$_6$ cluster and with the addition of an asymmetric tritopic linker, a MOF comprised of both RE$_6$ and RE$_9$ clusters was synthesized.[66] The highly connected "mixed-node" MOF, with 8-connected RE$_6$ and 12-connected RE$_9$ clusters, gives rise to a new topology, named **pek**. In 2018, Eddaoudi *et al.* further demonstrated the structural complexity that can be achieved using RE$_6$-clusters as molecular building blocks (MBBs) by rationally designing Tb$_6$-MOFs with merged nets (or topologies).[95] By using a symmetrical tritopic linker to give **spn** topology (6-connected node), and a hexatopic linker to give **hxg** topology (6-connected node), a MOF with merged **spn-hxg** topology (12-connected node) was generated, giving the new **sph** topology. In a somewhat related example, Zhou *et al.* prepared a series of mixed-linker MOFs, PCN-900, comprised of 12-connected RE$_6$-clusters with tetratopic tetrakis(4-carboxyphenyl)porphyrin (TCPP) and ditopic bent (4,4'-dicarboxydiphenyl sulfone, DCDPS) linkers.[97] The combination of the RE$_6$-cluster with a square tetratopic porphyrin-based linker (TCPP) is expected to give **csq** (8-connected node) or **she** (6-connected node) topology, but the addition of bent ditopic linkers fills the empty coordination sites on the RE$_6$-cluster node to give the new **tam** (12-connected node) topology.

1.3.2. RE(III)-Nonanuclear Cluster-Based MOFs

In 2014, the first nonanuclear cluster-based MOF was reported by Eddaoudi, where he introduced the new **gea** topology MOF, MOF-1.[77] **gea**-MOF-1 is comprised of an 18-connected molecular building block (MBB), termed as **eto** with the formula [RE$_9$(μ_3-OH)$_8$(μ_2-OH)$_3$(O$_2$C–)$_{18}$] (RE = Y(III), Tb(III), Er(III), Eu(III)) bridged by a symmetric tritopic ligand, 1,3,5-

benzene(tris)benzoate (BTB), thus forming the (3,18)-connected net.[77] Furthermore, differentiating symmetry in linkers can also affect topology. For example, the BTB linker in MOF-1 has a 120 ° angle between the carboxylates, whereas by using a less symmetrical linker with a 90 ° angle between the carboxylates, the (3,8,12)-c **aea** topology MOF is obtained, **aea**-MOF-1.[66]

The use of tetratopic and hexatopic ligands has also been demonstrated in the synthesis of RE_9-MOFs (Figure 1.5). The **shp** (square and hexagonal prism) topology, for example, was formed with Y(III) and Tb(III) using a tetratopic linker, TCPP,[98] and with Y(III) and 1,2,4,5-tetrakis(4-carboxyphenyl)benzene (TCPB).[78] Using Y(III) and Tb(III) with 1,3,6,8-tetrakis(p-benzoic acid)pyrene (H_4TBAPy), the **shp** topology was also obtained giving rise to RE-CU-10.[99] RE-CU-10 was studied as a heterogenous photocatalyst for selective oxidation and detoxification of a sulfur mustard simulant, 2-chloroethyl ethyl sulfide (2-CEES).[99] RE-CU-10 was also later reported with La(III), Nd(III), Eu(III), Tb(III), Er(III), Tm(III), and Yb(III) through the use of transmetallation.[100]
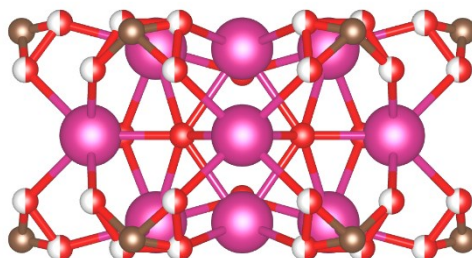
Figure 1.5. Schematic representation of a nonanuclear (RE_9) cluster. RE = pink, O = red, C = brown.

1.4. Overview of Methods in MOF Synthesis

1.4.1. Synthesis of MOFs

The synthesis of MOFs can be achieved by solvothermal,[101] electrochemical,[102, 103] mechanochemical,[104-109] sonochemical,[110] and microwave-assisted methods.[110, 111] Conventionally, the solvothermal synthesis method is used. To optimize a synthesis, synthetic factors may need to be adjusted to get the desired MOF including, but not limited to, temperature,[112, 113] pressure,[114] modulator amount and type,[115] solvent amount and type,[113, 116] pH,[113] and synthesis time.[117]

1.4.1.1. Solvothermal synthesis

In the method of solvothermal synthesis, a metal salt and a multitopic linker are mixed in the presence of a high boiling point solvent, placed in the oven.[101] The high boiling point solvents include *N,N*-dimethylformamide (DMF) (BP = 153 °C) and *N,N*-dimethylacetamide (DMA) (165 °C), amongst others. The decomposition of the high BP solvents at high temperature stabilizes the metal precursor. For example, the decomposition of DMF at high temperatures leads to the formation dimethylamine and formate. The dimethylamine is a base that can help in the deprotonation of the carboxylic acid functionality on the linker, and the formate can help in stabilizing the metal precursor by binding to it. Similarly, the decomposition of DMA leads to formation of dimethylamine and acetate.

In addition, modulators can be used for the formation of dynamic bonds. Modulators are non-structural monotopic ligands that compete with the organic linker in the binding to the metal node and generally have a carboxylic acid functionality, though can include strong acids as well (e.g., HCl) (Figure 1.6). It is noteworthy that the presence of dynamic bonds is of high importance in forming long-range ordered and crystalline materials, ideally leading to a stable structure. As previously mentioned (Section 1.3), fluorinated modulators, such a 2-FBA and 2,6-DFBA favour the formation of RE cluster nodes due to the hydrophobic surrounding that protects the cluster during assembly.

Benzoic Acid   Acetic Acid   Formic Acid   Hydrochloric Acid
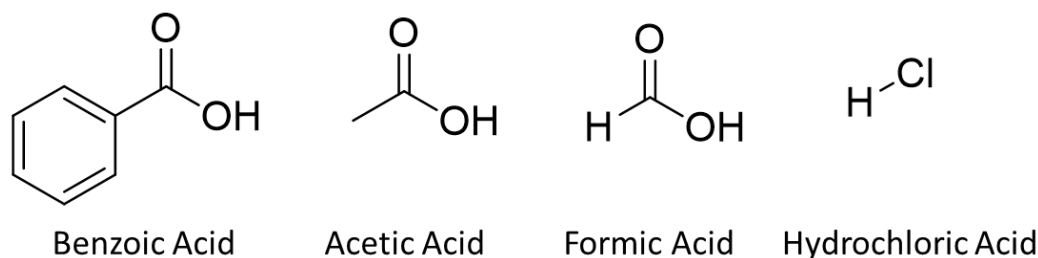
Figure 1.6. The different modulators that may be used in the synthesis of MOFs.

1.4.2. Activation of MOFs

One of the properties that make MOFs so attractive, is their ability to have permanent porosity in their structures. Activation is a strategy used to remove guest molecules from the pores of the material thus allowing for free pores that can be utilized in a number of applications. Activation can be done through vacuum with heating,[118, 119] solvent-exchange,[6, 101, 119] supercritical CO_2 (scCO$_2$),[119, 120] freeze-drying,[119] and chemical treatment.[119]

Solvent exchange and heat with vacuum drying is usually performed together. When synthesizing MOFs with high boiling point solvents such as DMF and DMA, to access free pores, the mother solvent needs to be exchanged with solvents that possess lower boiling point and lower surface tension prior to drying under vacuum with heat. Essentially, in solvent-exchange, the MOF is centrifuged down allowing for the MOF particles to sediment at the bottom the centrifuge tube, thus allowing for easy removal of the mother solvent. Next, fresh mother solvent is added to the MOF particles, allowing for the removal of guest molecules and impurities that are in fact soluble in the mother solvent. This is repeated several times over the course of a few hours to a few days. The solvent is then exchanged with a volatile solvent (e.g., acetone, methanol, ethanol) allowing for the MOF to be soaked in it for a few hours to a few days, with repetition of removing "old" solvent and adding "fresh" solvent. Lastly, the final removal of the solvent is performed by placing the sample under vacuum with heating.

1.5. Characterization of MOFs
1.5.1. Powder X-ray Diffraction (PXRD)

PXRD is the one of the most important characterization techniques in the field of MOFs. It allows for the detection of bulk crystallinity in a sample and the phase purity of the material.[101, 121] In addition, it can be used as a means of comparison of the unit cell sizes of isostructural MOFs. The unit cell size is defined by the d-spacing (the distance between planes of atoms), which in turn affects the angle of the reflections observed in the PXRD pattern. In the instance that there is an isostructural MOF (both containing the same topology), the PXRD pattern will likely be the same, however shifting may occur depending on the d-spacing (larger unit cell will have smaller d-spacing) (Figure 1.7).
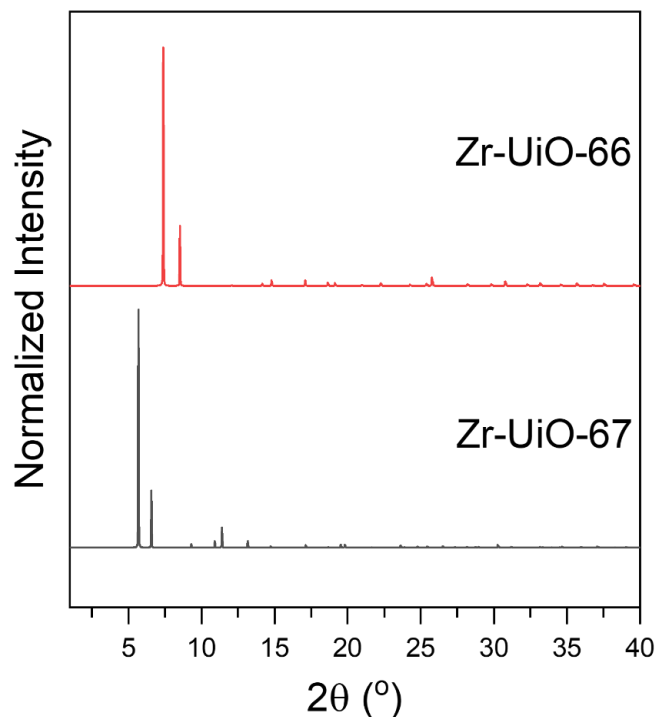
Figure 1.7. PXRD pattern of isostructural MOFs, Zr-UiO-66 and Zr-UiO-67.

Using Bragg's law (2d sinθ= nλ), the wavelength of the X-ray (λ) remains constant as it depends on the instrument, whereas the d-spacing (d) and the order of reflection (n) affect the location of the angle of reflections (2θ).[122, 123] In PXRD, Bragg's law must be satisfied for a diffraction peak to occur, and thus the angle is scanned, leading to the occurrence of reflections that correspond to crystallographic planes. The same phase pure material may have slight changes in its PXRD pattern, which can be due to preferred orientation, where the loading of the sample on the zero-background holder may be packed differently, but this can be avoided by allowing for the rotation of the sample while the instrument is collecting data. [123]

1.5.2. Single-crystal X-ray Diffraction (SCXRD)

In the event of forming single crystals of MOFs where the size exceeds 50 μm and the material can diffract X-rays, SCXRD can be performed. To obtain large enough crystals, synthetic optimization may be needed including, but not limited to, an increase in reaction temperature, decrease in solvent volume, and introduction of a modulator. Currently, SCXRD allows for the most accurate and thorough representation of the MOF structure, although some reliability issues are also present.[121, 124] When a novel MOF is synthesized and the SCXRD data is collected, a code

is generated, and the structure is added to the Cambridge Structural Database (CSD) crystallographic database.[2]

1.5.3. Nitrogen (N₂) Adsorption and Desorption Isotherms

Nitrogen (N_2) adsorption and desorption isotherms can be used to determine the surface area of a MOF material, including the pore volume and pore size distribution. The surface area of MOFs is calculated using Brunauer, Emmett and Teller (BET) theory.[125] BET theory is based on physical sorption, where it is a reversible sorption through van der Waals/dipole interaction leading to multi-layer saturation.[126, 127] Essentially, the surface of the MOF is covered with nitrogen gas molecules in the first layer and these molecules act as sites for nitrogen molecules in the second layer, followed by the third layer and so on and so forth and finally, the number of gas molecules are calculated where a higher surface area is correlated to more molecules forming a monolayer on the surface (Figure 1.8).[128] Nitrogen sorption isotherms are collected at 77K, which is the boiling point of nitrogen.[101] The adsorption occurs initially reaching a maximum quantity adsorbed, then to a relative pressure of 1.0, at which point the desorption begins.
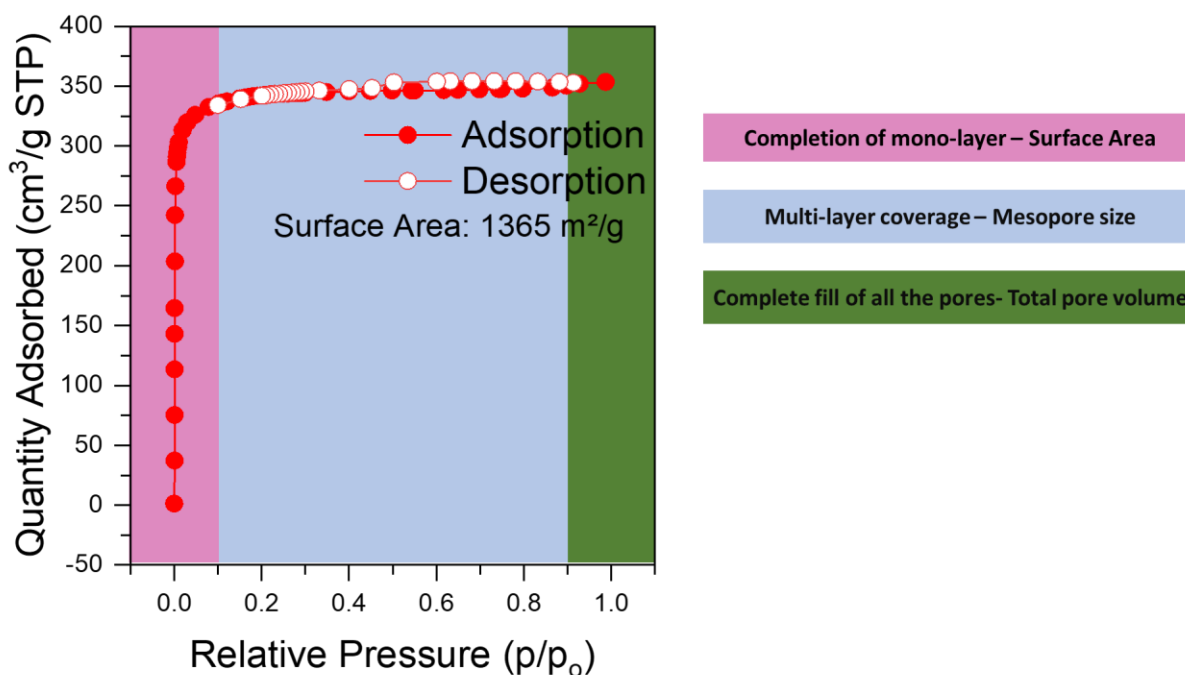
Figure 1.8. A representative nitrogen gas adsorption isotherm run at 77K, which includes the adsorption of the monolayer surface, followed by the multilayer coverage and the filling of all of the pores, and finally the desorption.

There are 6 isotherm types, which are given in roman numeral numbering (I-VI)[126] (Figure 1.9). Type I, II and IV are the most common among MOFs, Type III and V are less common. In this thesis, only Type I isotherms are presented for the synthesized materials, indicative of MOFs with micropores. There are two subcategories in Type I isotherms, where Type I(a) is indicative of smaller micropores in comparison to Type I(b), which is observed for relatively larger micropores. All isotherms are plotted as quantity adsorbed (cm^3/g STP) vs. relative pressure (P/P_0) at constant temperature where the pressure is vacuum to near atmospheric, and the surface area is given by m^2/g.
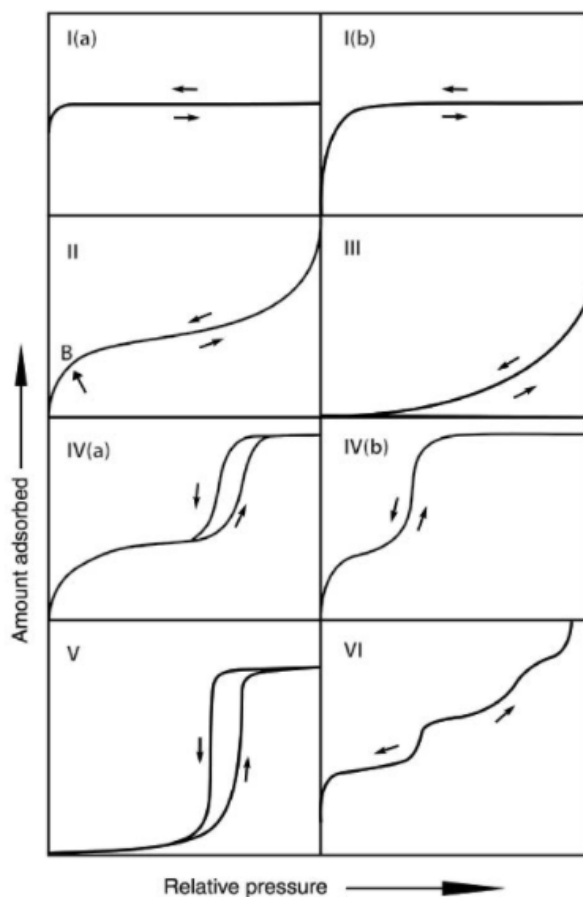
Figure 1.9. The 6 isotherm types (Type I-VI) for physisorption isotherms.[126]

In addition to surface area measurements, the pore volume and pore size distribution can be calculated from adsorption isotherms as well. Materials can have micropores (<2 nm), mesopores (2-50 nm) or macropores (>50 nm).[126] The pore volume measures the total internal void volume per unit mass of adsorbent (cm^3/g). Generally, the non-local density functional theory (NLDFT) model is used for pore volume and pore size distribution analysis of MOFs.

1.5.4. Thermogravimetric Analysis (TGA)

Thermogravimetric analysis (TGA) is a technique that is used to view the thermal decomposition of a MOF to give information about its thermal stability. The change in weight % of a MOF is measured with increasing temperature in the presence of carrier gas species (e.g., air, Ar, N_2).[101] Generally, there is a percentage associated with the loss of solvent, followed by the decomposition of organic linkers, and finally there is the remaining metal oxide once the decomposition is complete. By using TGA along with other characterization techniques, such as inductively coupled plasma – mass spectrometry (ICP-MS), the chemical formula of a MOF can be determined.

1.5.5. Scanning Electron Microscopy (SEM)

Scanning electron microscopy (SEM) is a characterization technique that provides the particle size and the particle shape of a MOF (Figure 1.10).[101] MOFs are generally non-conductive materials, thus electric charging occurs, which does not allow for optimal analysis of the material. Therefore sputter-coating can be used to eliminate or reduce this occurrence.[129] Sputter-coating increases the conductivity of the sample by adding a layer of conductive material (e.g., gold). SEM can be used with energy dispersive X-ray spectroscopy (EDS) to obtain quantitative and qualitative data determining the presence of particular elements.[101] In addition, it is possible to determine if the distribution of an element is even or if it is localized in certain regions of the material. Through mapping, the elements of interest are often colored to view their distribution.
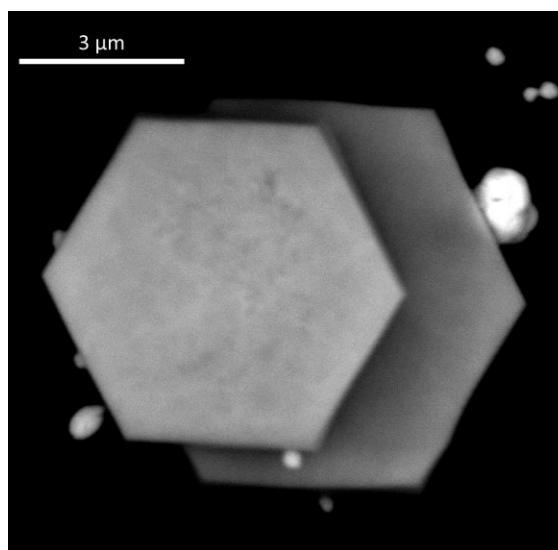
Figure 1.10. SEM micrograph of a MOF exhibiting hexagonal shaped particles.

1.5.6. Proton Nuclear Magnetic Resonance (^{1}H-NMR) Spectroscopy

Proton nuclear magnetic resonance (^{1}H-NMR) spectroscopy is used to determine the linker purity in a MOF.[101] In order to collect ^{1}H-NMR spectroscopy data, a MOF must first be digested in deuterated acid (e.g., D_2SO_4) prior to being dissolved in another deuterated NMR solvent (e.g., DMSO-d_6). Using this technique, it is possible to determine if reactants, modulator, or solvent molecules remain in the MOF.[101]

1.5.7. Inductively Coupled Plasma - Mass Spectrometry (ICP-MS)

ICP-MS can be used to determine the elemental ratio of metals or heteroatoms present in a MOF. By accurately weighing out a MOF sample prior to ICP-MS analysis, the technique can also be to help determine the chemical formula of a MOF.[101] Similar to ^{1}H-NMR spectroscopy, the sample must first be digested with a strong acid (e.g. HNO_3, H_2SO_4), in the presence of H_2O_2 to oxidize the organic components, prior to diluting the sample with water.[101]

1.5.8. Diffuse Reflectance Infrared Fourier Transform Spectroscopy (DRIFTS)

Diffuse reflectance infrared Fourier transform spectroscopy (DRIFTS) allows for the determination of IR active functional groups.[101] In order to run DRIFTS successfully, the MOF sample must first be dried in order to avoid the broad -OH band (3500-3800 cm^{-1}) that is indicative of the presence of water.[101] The broad water band overlaps with the sharp, well-defined peaks from the bridging and terminal -OH groups that are found on MOF metal cluster nodes. To prepare a MOF sample for DRIFTs, once the MOF is dry, it is very gently mixed with KBr to dilute the sample, where KBr is also used as the background for the measurement. Common IR active functional groups in MOFs include C=O, bridging and terminal O-H, and C-H.

1.5.9. Ultraviolet-Visible (UV-Vis) Spectroscopy

Ultraviolet-Visible (UV-Vis) spectroscopy is a characterization technique used to measure the light a material absorbs with respect to a blank or a reference.[130] In solution state UV-Vis spectroscopy, MOF starting materials (metal precursor and linker) can be measured by dissolving them in solvents in which they are soluble (e.g., DMF). However, to obtain an absorption spectrum of a MOF itself, solid-state UV-Vis must be performed, where the MOF can be dispersed in a volatile solvent (e.g., methylene chloride (DCM), ethanol (EtOH), methanol (MeOH)), or can be drop-cast onto a glass or quartz slide.

1.5.10. Diffuse Reflectance (DR) UV-Vis Spectroscopy

Diffuse reflectance (DR) UV-Vis spectroscopy is a characterization technique that is used to collect light reflected from a MOF, which can then be transformed through Kubelka-Munk transformation to give an absorbance spectrum of the material.[131] The diffuse reflectance of a material is proportional to its absorption coefficient. The sample can be prepared by drop-casting onto a quartz slide and placing it into an integrating sphere (coated with barium sulfate) or by using a powder sample holder in a specialized diffuse reflectance accessory.

1.5.11. Photoluminescence Spectroscopy

In photoluminescence spectroscopy, when a MOF is excited by light, meaning that is absorbs photons, an electron from the singlet ground state is moved to a higher electronic state known as the excited singlet state. Once at this state, the electron can go back down to the lower energy singlet ground state through a radiative process known as fluorescence.[132] Alternatively, the electron from the singlet excited state can also move to the triplet excited state through intersystem crossing and return to the singlet ground state through a spin-forbidden radiative process known as phosphorescence.[133] If the triplet excited state of an organic chromophore (e.g., MOF linker) has sufficient energy, that energy can be transferred to the excited state energy levels of lanthanide ions (e.g., MOF node) through Dexter[134] or Förster[135] mechanisms,[136] leading to the antenna effect[137] which is the sensitization of the metal through energy transfer from the organic linker.

Similar to solid-state UV-Vis, a MOF can be dispersed in a volatile solvent (e.g., DCM) or drop-cast onto a quartz or glass slide to collect photoluminescence data. A luminescent MOF sample (Figure 1.11) should be excited at one of the wavelengths at which it absorbs, from which an emission spectrum is generated. Essentially, the photoexcitation of a MOF leads to an electron moving to a higher energy electronic state, at which point the energy can be released in the form of a photon.
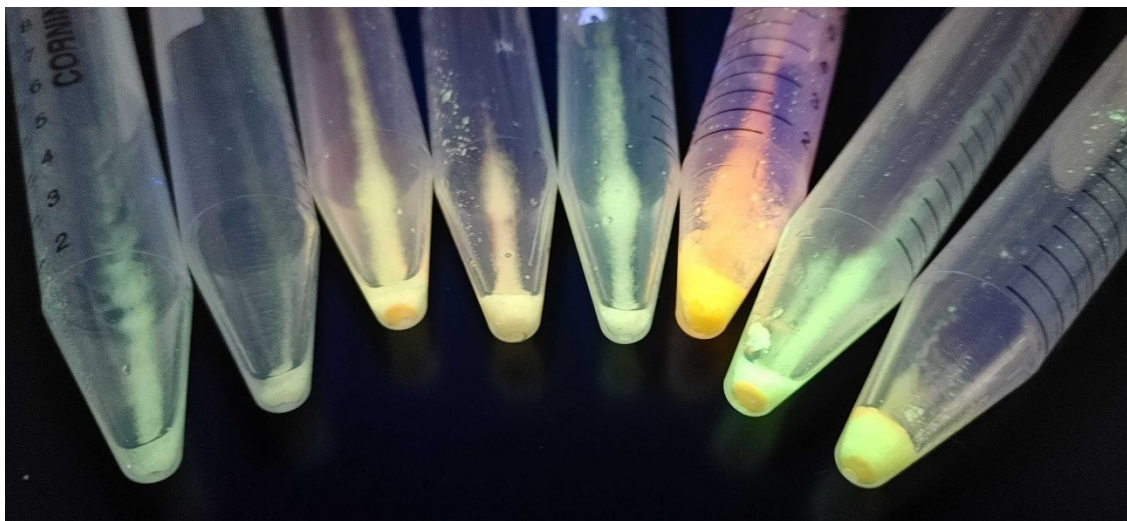
Figure 1.11. Luminescent MOF samples in centrifuge tubes under a handheld UV lamp (365 nm).

1.6. Luminescence

1.6.1. Photoluminescence

When a material is exposed to energy (e.g., photons) and leads to the emission of light, this can be referred to as photoluminescence.[138] The terms fluorescence and phosphorescence fall under the category of photoluminescence. In fluorescence, the electronic transitions are spin allowed with lifetimes typically in the nanosecond (ns) range, whereas phosphorescence has spin forbidden transitions, which lead to longer lifetimes that can be several seconds.[139]

Luminescence in MOFs is a fairly recent notion as it was first reported in 2002.[140] Lanthanoid MOFs have been widely studied for luminescence applications[141, 142] and this can be credited to their large Stokes shift, long lifetimes, and narrow and sharp emissions.[18, 143] The linker-based and metal-based components can give rise to emission in lanthanoid MOFs.[18] Linker-based luminescence in MOFs occurs through the use of conjugated organic linkers (rich in π-electrons) which typically absorb light in the UV-Vis region (200-800 nm) and once excited, linker-based emission can occur.[139] When both ligand- and metal-based emission occurs in lanthanoid MOFs, this is most often attributed to the antenna effect.[137] In lanthanoid MOFs, the antenna effect occurs upon linker excitation which leads to generation of the triplet state of the organic linker, which can transfer energy to the lanthanoid leading to metal-based emission from the lanthanoid ion (Figure 1.12). According to Laporte's rule, the *f-f* transitions of lanthanoids are symmetry forbidden transitions, and they are well-shielded by the $5s^25p^6$ subshells,[144] thus leading to weak emission.[139] Through the antenna affect, the transfer of energy from the linker to the lanthanoid ion allows for

a stronger and more intense emission, overcoming the low absorption efficiency of the *f-f* transitions.[139, 145] In addition, Latva's rule states that there is an ideal energy separation between the organic linker's excited triplet state ($^3\pi^*$) and the lanthanide ion's emitting state which is found to be between 2000 to 4000 cm^{-1} for optimal sensitization.[146] In the antenna effect, when the linker is exciting into the lanthanide, the energy transfer generally occurs from the linker triplet state to the lanthanoid emitting state.[146]
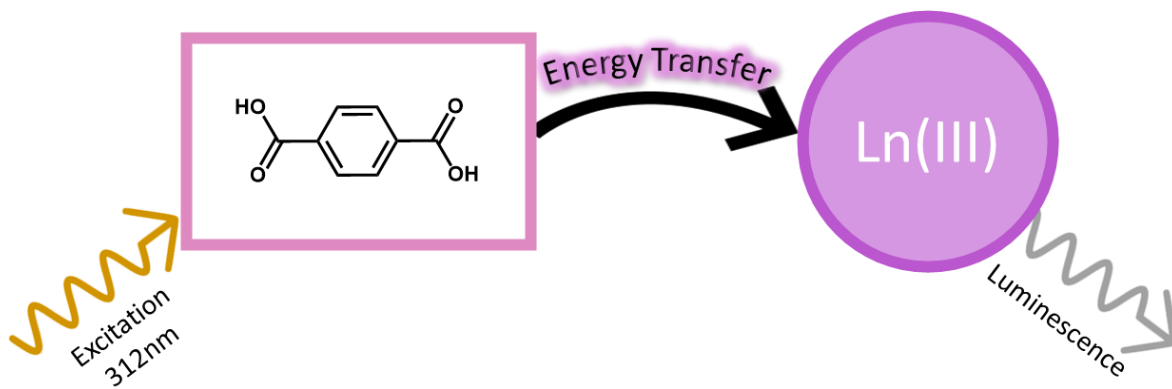
Figure 1.12. The antenna effect with a conjugated ligand for Ln(III) sensitization.

1.6.2. Radioluminescence

When a material is exposed to ionizing radiation and it leads to the emission of light, the phenomenon is referred to as a radioluminescence.[138] To date, the majority of reported RL MOFs utilize high-Z metal nodes for X-ray attenuation, and organic linkers as the emitting species. [147-152] More recently, lanthanoid-based MOFs comprised of metal ion nodes have been shown to demonstrate radioluminescence arising from Eu^{3+} and Tb^{3+}, the most efficient radioluminescent ions that display 4f-4f transitions. In particular, the use of emissive lanthanoids has been shown to increase the luminosity of the material[153] and has led to metal-based radioluminescence, as opposed to relying solely on emissive organic linkers.[154] Lanthanoid cluster-based MOFs, which have not yet been studied for their radioluminescent properties, are of particular interest as platform materials for X-ray scintillation owing to the high density of high-Z metals present in multinuclear lanthanoid cluster nodes coupled with the diversity of structures that can be obtained using clusters as SBUs.

1.7. Scope of Thesis

The following two chapters will discuss the synthesis, characterization and photophysical properties of three-distinct RE cluster-based MOFs, including a deeper analysis of their photophysical properties pertaining to photoluminescence and radioluminescence.

Chapter 2 describes tuning of the photoluminescent behaviour of RE-UiO-66 through the incorporation of bi-metal and tri-metal RE_6-nodes, ultimately leading to the formation of a white-light emitting MOF.

Chapter 3 describes a facile route for modulating the photoluminescent and radioluminescent properties of Tb(III)-based MOFs. In addition, a novel terbium-based MOF, Tb-CU-27 (CU = Concordia University), isostructural to Y-**shp**-MOF-5, is presented, where single-crystal X-ray diffraction data allows for a full understanding of the structure of the MOF. It was found that by using different Tb(III)-cluster nodes as X-ray attenuators, and an organic linker as a sensitizer, metal-based (Tb-UiO-66), linker-based (Tb-CU-10), and metal+linker based (Tb-CU-27) photoluminescence is observed.

Chapter 2

Tuning the RE-UiO-66 Platform for White Light Emission

2.1. Introduction

The development of energy efficient lighting technologies is important for reducing global electricity consumption, and thus greenhouse gas emissions.[155] As such, the replacement of traditional, low energy efficiency lighting sources such as incandescent and fluorescent lamps, is required for mitigating the global energy crisis.[156] As one of the most promising solutions, light emitting diodes (LEDs) have gained interest due to their relatively long lifespan,[157] high energy efficiency,[158, 159] and accessibility to a wide range of colours and temperatures.[160] By tuning the colour and temperature of specific phosphors, white LEDs (WLEDs) can be produced and used for applications in solid state lighting and displays.[158]

Currently, there are three popular strategies for the production of WLEDs; (i) utilizing multiple LED chips where each chip emits red, green, and blue (RGB) light that is mixed to give white[158, 161], (ii) coating UV-LED chips with phosphors that absorb UV light and emit triple wavelength RGB,[162, 163] (iii) coating blue LED chips with phosphors that absorb a portion of blue light, and emit green and red.[158, 164] When designing a material for approach ii, the Commission International d'Eclairage (CIE) chromaticity diagram is often used to determine and compare the colour purity of the RGB emitting phosphor.[165] Two coordinates from the visible region are calculated, where pure white is defined as x, y = 0.33, 0.33.

Significant effort has gone into the development of new white light (RGB) emitting materials with the use of organic molecules or polymers, [166, 167] metal-doped materials,[168, 169] metal complexes,[170] and nanomaterials as phosphors.[171, 172] In the solid-state, pure organic molecules and polymers are prone to luminescence quenching, posing a challenge for long term lighting applications.[173] On the other hand, inorganic LEDs have higher efficiencies and longer lifetimes relative to organic LEDs, but often suffer from challenges related to solution proccessability.[174]

Metal–organic frameworks (MOFs) are a class of coordination polymers that are comprised of inorganic metal nodes and organic linkers, forming 2- or 3-dimensional network structures.[1, 3-6, 175] Currently, only a handful of white light emitting MOFs have been reported in literature,[176-182] with some emitting from the organic component[176] inorganic component,[183] both metal and organic components,[177-179, 184] and others requiring doping with coordination

compounds,[180] perovskites,[181] or rare-earth (RE) elements[185] MOFs comprised of RE elements commonly have trivalent RE ions as part of their metal node, which are separated from each other by organic linkers, preventing self quenching and photobleaching,[186] and thus making RE-MOFs very interesting candidates for WLEDs. RE-MOFs comprised of multinuclear cluster nodes allow for the incorporation of multiple RE elements at high concentrations, giving rise to a high degree of colour tunability in these materials.

The archetypal MOF, Zr-UiO-66, has been reported numerous times in literature for its robust structure,[187, 188] high surface area,[189, 190] and porosity.[191] More recently, we reported RE analogues of UiO-66 comprised of RE_6-cluster nodes bridged by 1,4-benzenedicarboxylate (BDC^{2-}) linkers (Figure 2.1).[192] Given that Eu(III) and Tb(III) ions emit red and green light, respectively,[193, 194] and BDC^{2-} emits in the blue region,[195] we hypothesized that the RE-UiO-66 platform would be ideal for the design of a white light emitting MOF. In addition to emitting blue light, the BDC^{2-} linker in RE-UiO-66 plays a key role in the sensitization of the RE metals via the antenna effect.[196-201] Herein, we evaluate the photoluminescent behaviour of mixed metal RE-UiO-66 analogues (RE = Tb(III), Eu(III), and Gd(III)) by tuning the ratio of RE ions to give bi-metal and tri-metal RE_6-nodes, ultimately leading to the formation of a white light emitting MOF.
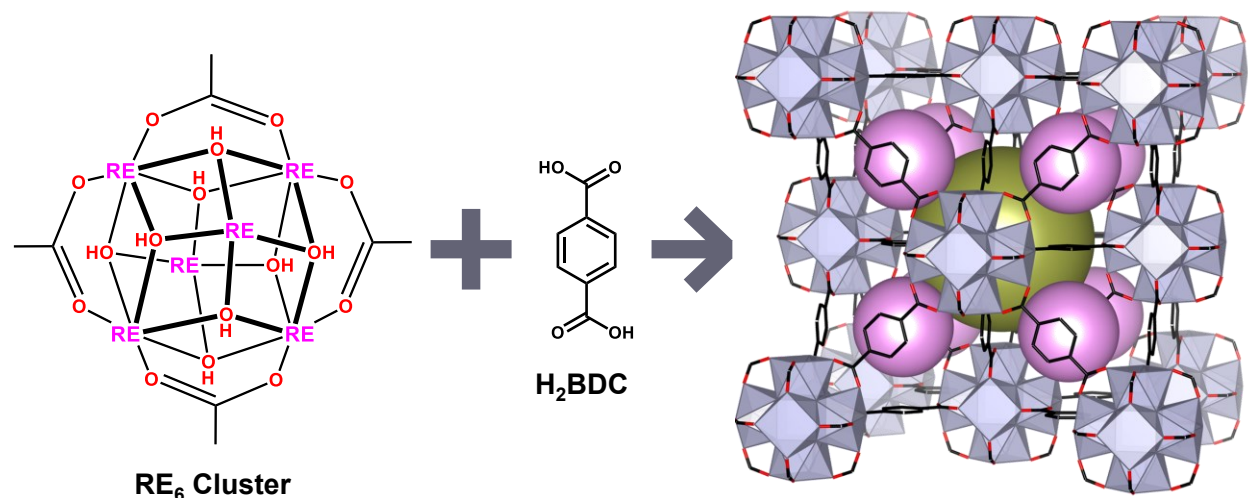
Figure 2.1. Structure of Tb-UiO-66 depicting the RE_6 cluster with the H_2BDC linker forming the **fcu** net with the tetrahedral cage (pink spheres) and octahedral cage (gold sphere).

2.2. Experimental Procedures

2.2.1. General Materials and Methods

All chemicals were used as received from commercial sources. *N,N'*-dimethylformamide (DMF), *N,N'*-dimethylacetamide (DMA), and acetone were purchased from Fisher Scientific (Fisher Chemical). 2,6-Difluorobenzoic acid (2,6-DFBA) was purchased from AmBeed. Terbium(III) nitrate hydrate ($Tb(NO_3)_3 \cdot xH_2O$), europium(III) nitrate hydrate ($Eu(NO_3)_3 \cdot xH_2O$ and gadolinium(III) nitrate hydrate ($Gd(NO_3)_3 \cdot xH_2O$) were purchased from Alfa Aesar. Terephthalic acid (H_2BDC) was purchased from Acros Organics.

Powder X-ray diffraction (PXRD) patterns were collected on a Bruker D2 Phaser diffractometer (measurements made over a range of $4° < 2\theta < 40°$ in $0.02°$ step with a 0.200 s scanning speed) equipped with a LYNEXE linear position sensitive detector (Bruker AXS, Madison, WI). Neat samples were smeared directly onto the silicon wafer of a propriety low-zero background sample holder. Data was collected using a continuous coupled $\theta/2\theta$ scan with CuKα ($\lambda = 1.54178$ Å) radiation source.

MOF samples were activated using a Micromeritics SmartVacPrep instrument equipped with a hybrid turbo vacuum pump. Nitrogen adsorption-desorption isotherms were measured at 77K on a Micromeritics TriStar II Plus instrument.

Inductively coupled plasma mass spectrometry (ICP-MS) data was measured on an Agilent 7500 Series. ~0.5 mg of RE-UiO-66 was digested in 750 μL H_2SO_4 at 100 °C in a sand bath for 24 h. This solution was diluted with deionized H_2O to a final volume of 10 mL.

Diffuse reflectance infrared Fourier transform spectroscopy (DRIFTS) data was recorded using a Thermo Scientific Nicolet 6700 FT-IR equipped with a MCT detector with a resolution of 1 cm^{-1} in the range of 4000-450 cm^{-1}. The samples were run after activation with no further treatment.

Scanning electron microscopy (SEM) images and energy dispersive X-ray spectroscopy (EDS) data were collected on a Phenom ProX desktop SEM.

Thermogravimetric analysis (TGA) was carried out in a TGA 5500 thermogravimetric analyzer by TA from room temperature to 800 °C at a rate of 10 °C/min under air.

Diffuse Reflectance UV-Vis absorbance spectroscopy data were collected on a Cary 5 Series UV-Vis-NIR Spectrophotometer (Agilent Technologies) with the EasiDiff^{TM} accessory. A

1 nm bandwidth and wavelength changeover at 350 nm were used for data collection. Activated samples were loaded into a sample cup with potassium bromide.

Photoluminescence spectra were collected using a PTI QuantaMaster 8075 spectrofluorimeter (Horiba). Samples of RE-UiO-66 were suspended in dichloromethane and drop-cast on quartz slides

2.2.2. Synthesis

Tb-UiO-66 was synthesized through a solvothermal synthesis where a suspension of $RE(NO_3)_3 \cdot xH_2O$ (see Table 2.1 for details), terephthalic acid (0.171 mmol, 28.5 mg) and 2,6-difluorobenzoic acid (2.78 mmol, 440 mg) was prepared in 8 mL of DMA in a 6-dram vial. The solution was sonicated until all reagents dissolved and was placed in a 120 °C oven for 72 hours. Once out of the oven, the solution was cooled down to room temperature before centrifugation and subsequent removal of the DMA reaction solvent. The solid material was then washed with fresh DMF (3 x 5 mL) over the course of 24 hours and later with fresh acetone (3 x 5 mL) over the course of 2 days. The material was set to dry in a vacuum oven at 80 °C for 1 hour and was then activated at 120 °C for 20 hours using a Micromeritics Smart VacPrep instrument.

Table 2.1. The amounts of rare-earth metals used in the synthesis of single, bi- and tri-RE-UiO-66.

Sample	Measured Amounts (mg)			Measured Amounts (mmol)		
	Tb	Eu	Gd	Tb	Eu	Gd
Tb–UiO-66	78.9	-	-	0.174	-	-
Eu–UiO-66	-	77.6	-	-	0.174	-
Gd–UiO-66	-	-	78.5	-	-	0.174
Gd:Eu-UiO-66	-	8.2	70.6	-	0.0183	0.1564
Tb:Gd-UiO-66	20.9	-	61.1	0.0461	-	0.1353
Tb:Eu-UiO-66	63.9	20.2	-	0.1410	0.0452	-
Tb:Gd:Eu-UiO-66	17.8	5.4	52.0	0.0399	0.0123	0.1183

2.3. Results and Discussion

RE-UiO-66 analogues with bi-metal (Eu:Gd, Tb:Gd, Tb:Eu) and tri-metal nodes (Tb:Gd:Eu) are synthesized using a mixture of $RE(NO_3)_3 \cdot xH_2O$ precursors (see Table 2.1 for

details) with the ditopic linker H_2BDC in the presence of a fluorinated modulator, 2,6-difluorobenzoic acid (2,6-DFBA) in *N,N*-dimethylacetamide (DMA) solvent. In order to confirm the bulk crystallinity and phase purity of bi-metal and tri-metal RE-UiO-66 analogues, powder X-ray diffraction (PXRD) data were collected. As can be observed in Figure 2.2a and Figure 2.3 all reflections are consistent with the expected **fcu** topology of RE-UiO-66. N_2 adsorption-desorption analysis of Tb:Gd:Eu-UiO-66 shows a reversible Type I isotherm, as expected for RE-UiO-66, with an experimental Brunauer–Emmett–Teller (BET) surface area of 930 m^2 g^{-1} (Figure 2.2b).
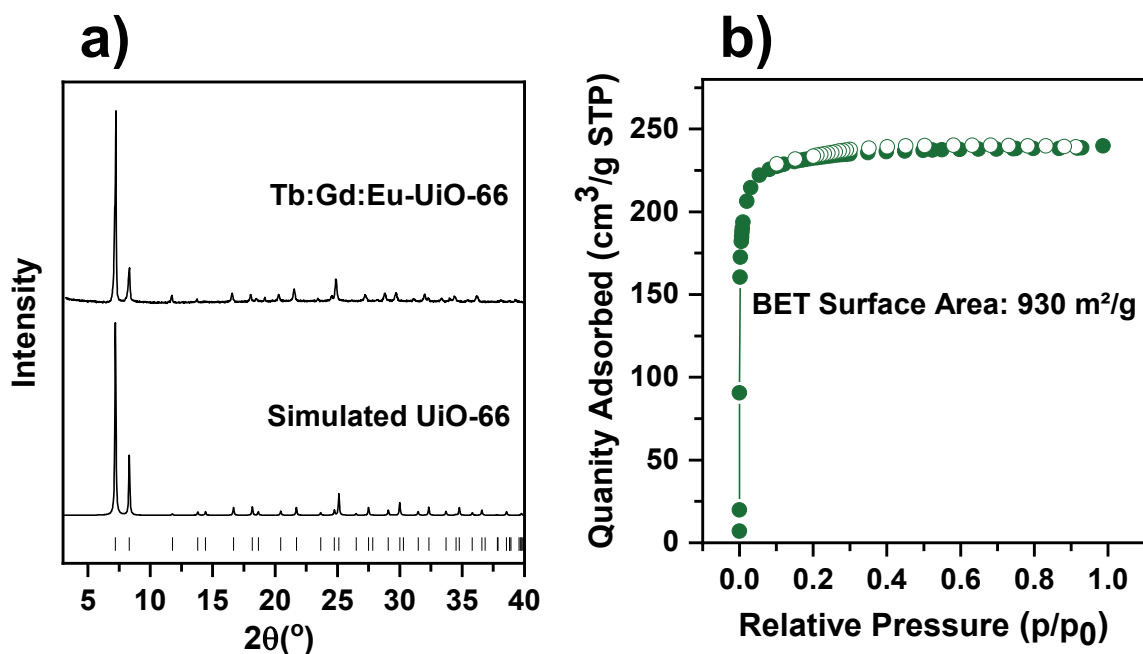
Figure 2.2. (a) Powder X-ray diffraction (PXRD) pattern of synthesized Tb:Gd:Eu-UiO-66 and the simulated pattern, and (b) nitrogen sorption isotherm analysis of Tb:Gd:Eu-UiO-66.
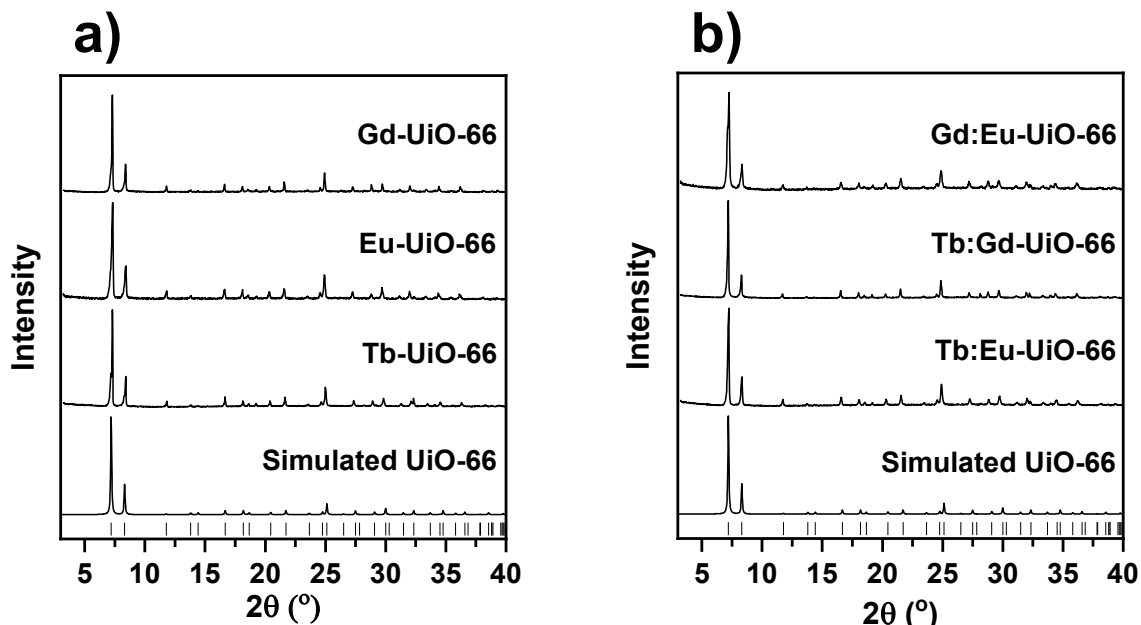
Figure 2.3. PXRD pattern for (a) as-synthesized Gd-UiO-66, Eu-UiO-66, and Tb-UiO-66 and the simulated pattern of RE-UiO-66, and (b) as-synthesized Gd:Eu-UiO-66, Tb:Gd-UiO-66, and Tb:Eu-UiO-66 and the simulated pattern of RE-UiO-66

Diffuse reflectance infrared Fourier transform spectroscopy (DRIFTS) of Tb:Gd:Eu-UiO-66 confirms the presence of some μ_3-OH groups in the RE$_6$-cluster nodes (Figure 2.4), however it should be noted that there is the possibility for μ_3-OH and μ_3-F ligands due to the use of a fluorinated modulator during MOF synthesis.[82]
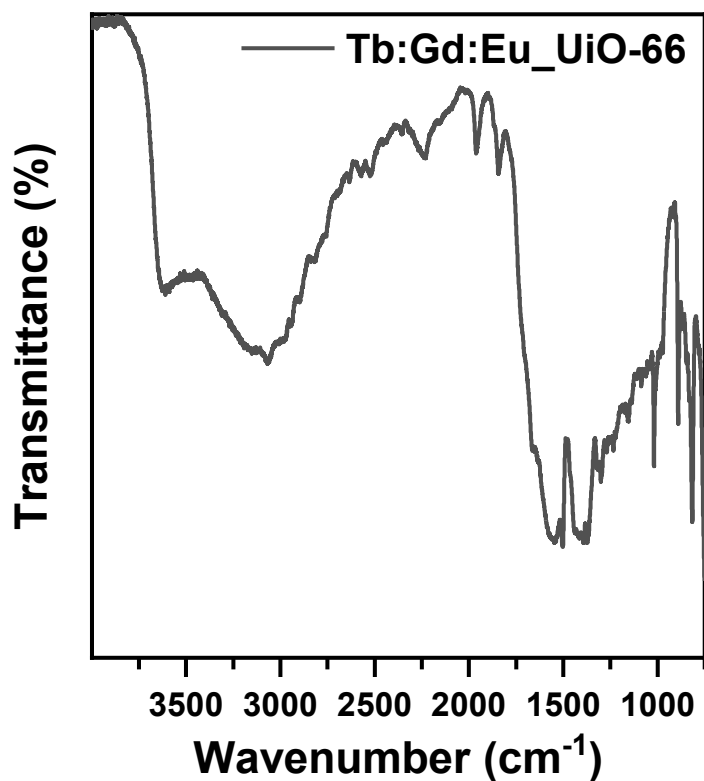
Figure 2.4. Diffuse reflectance infrared Fourier transform spectrum of Tb:Gd:Eu-UiO-66.

Scanning electron microscopy (SEM) micrographs reveal the expected octahedral morphology of Tb:Gd:Eu-UiO-66 with an average crystallite size of 21 μm (Figure 2.5). Additionally, energy dispersive X-ray spectroscopy (EDS) shows a homogeneous distribution of Tb(III), Gd(III), and Eu(III) metals with atomic percentages of 19.2 % (Gd), 8.7% (Tb), and 2.0% (Eu) (Figure 2.6), giving a 9.6 : 4.4 : 1 ratio for Gd:Tb:Eu. This ratio is in agreement with the ratio obtained by inductively coupled plasma-mass spectrometry (ICP-MS), which is 9.7 : 3.6 : 1 (Table 2.2).
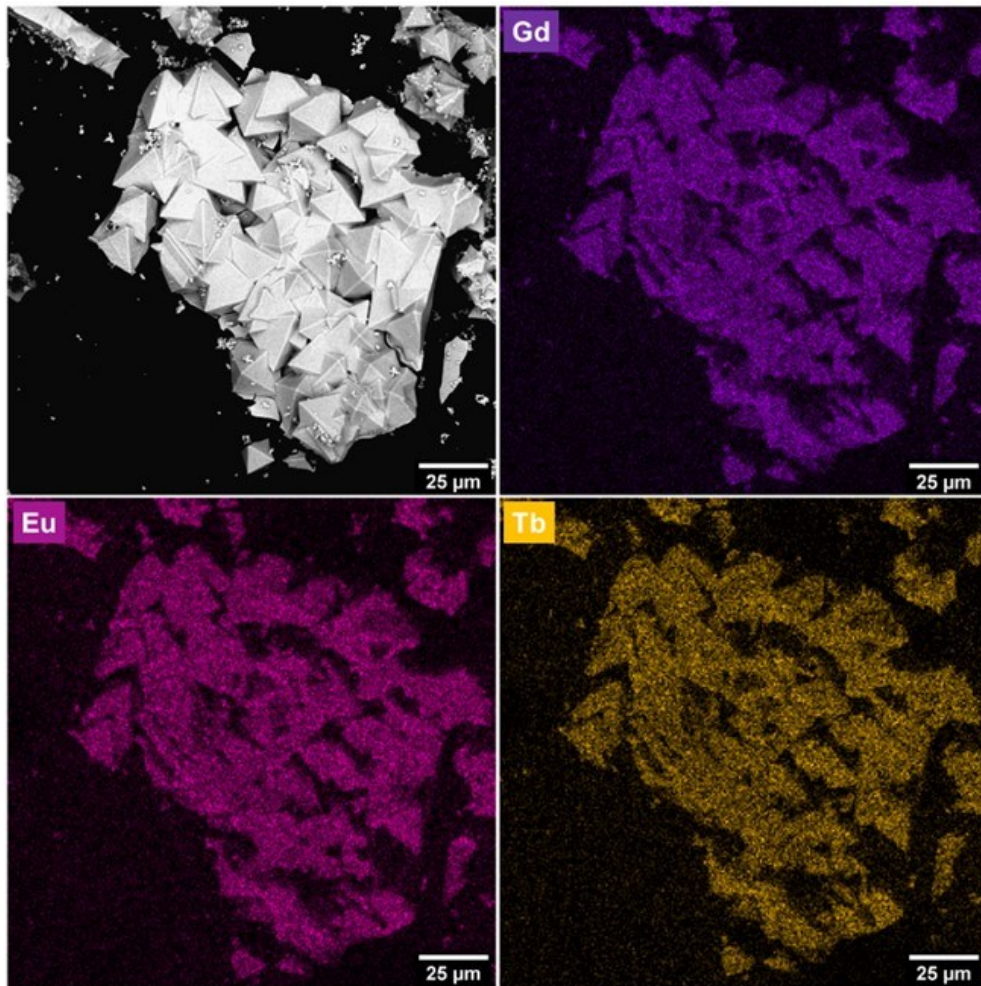
Figure 2.5. SEM micrographs and EDS mapping of Gd:Eu:Tb-UiO-66.
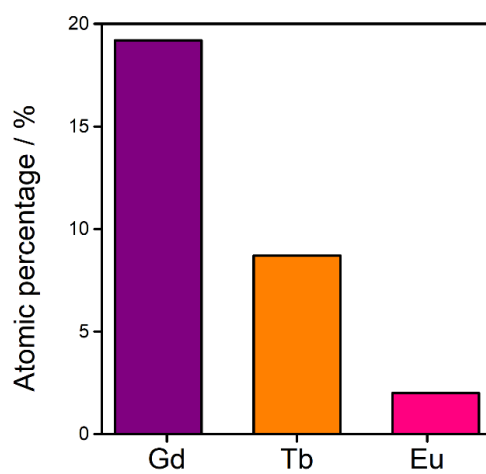
Figure 2.6. Atomic percentages of Gd(III), Tb(III) and Eu(III) in Tb:Gd:Eu-UiO-66

Table 2.2. ICP analysis of the metals in Tb:Gd:Eu-UiO-66.

Sample	ICP (molar ratio)			Measured Amounts (molar ratio)			Adjusted for Hexanuclear Cluster		
	Tb	Eu	Gd	Tb	Eu	Gd	Tb	Eu	Gd
6 – RD24 (Tri-metal)	3.6	1	9.7	2.9	1	9.5	1.5	0.5	4
7 – RD44 (Bi-metal)	-	1	8.5	-	1	8.5	-	0.6	5.4
8 – RD43 (Bi-metal)	1	-	2.8	1	-	2.9	1.6	-	4.4
9 – RD25 (Tri-metal)	3.6	1	9.5	3.0	1	9.6	1.6	0.4	4
10 – RD42 (Bi-metal)	3.5	1	-	3.1	1	-	4.6	1.4	-

Eu(III) and Tb(III) ions emit from their $^5D_0$ and $^5D_4$ states with energies of 17 250 and 20 500 cm^{-1}, respectively.[202] Tb(III) emission can be sensitized via the antenna effect through energy transfer from the triplet excited state (T_1) of an organic ligand to the $^5D_4$ state (20 500 cm^{-1}), whereas Eu(III) emission can be sensitized through energy transfer to the $^5D_0$ state (17 250 cm^{-1}), or higher lying ^5D_J states ($^5D_1$ = 19 000 cm^{-1}, and $^5D_2$ = 21 450 cm^{-1})[146]. As such, sensitization of the two lanthanoids via the antenna effect requires a linker T_1 energy of at least 22 350 cm^{-1}.[146, 202] If the T_1 energy of the linker is too close to the acceptor state of the lanthanoid, energy back-transfer to the linker can occur, leading to quenching of the lanthanoid emission.[146] Alternatively, if the T_1 energy of the linker is too high (>26 000 cm^{-1}), there will be inefficient energy transfer to the lanthanoid.[203, 204] BDC^{2-} has a T_1 energy of 25 641 cm^{-1}, which is sufficient for sensitizing both Eu(III) and Tb(III) emission. Given that Eu(III) and Tb(III) ions may be present in the same RE$_6$-cluster of RE-UiO-66, and therefore 3.92 Å apart, energy transfer from Tb(III) to Eu(III) is also possible.[205] Tb(III) ions give rise to green emission with peaks at 489, 544, 582 and 617 nm, $^5D_4$ → $^7F_{3,4,5,6}$ as can be seen in Tb-UiO-66 (Figure 2.7a). Eu(III) ions gives rise to red emission with peaks at 590, 615, 655, 696 nm, $^5D_0$ → $^7F_{1,2,3,4}$ as can be observed in Eu-UiO-66 (Figure 2.7b). Eu-UiO-66 also exhibits a broad blue emission band from 350-500 nm from the singlet state of the BDC^{2-} linker. In order to further increase the contribution of the linker emission in RE-UiO-66, a RE(III) ion with high energy $4f$ excited states is required to avoid the linker T_1 to RE(III) energy transfer pathway. Given that Gd(III) has very high energy $4f$ excited states (> 32 000 cm^{-1}), strong BDC^{2-} linker singlet state emission is observed in Gd-UiO-66, giving rise to a broad band centered at 425 nm in the blue (Figure 2.7c).
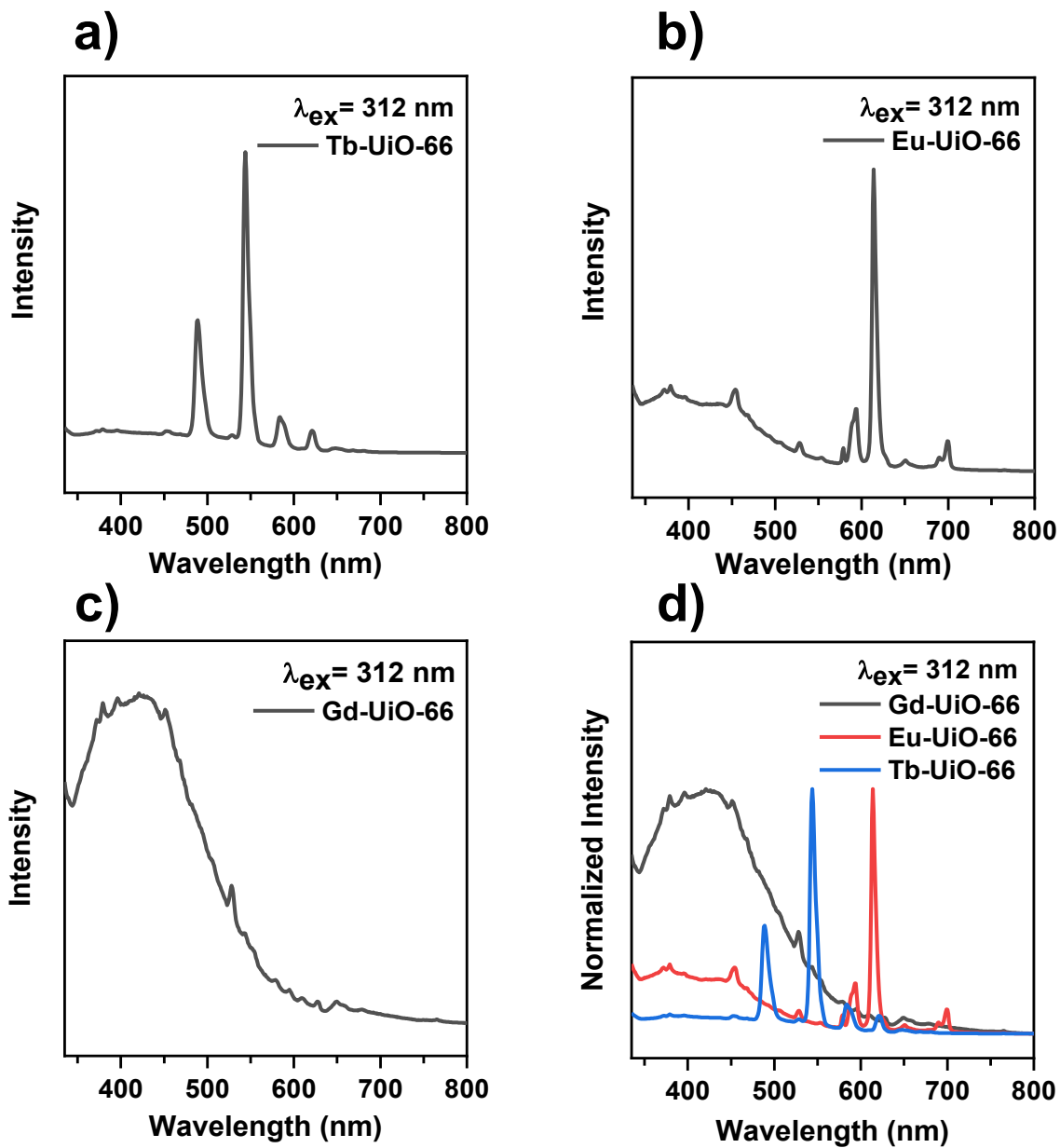
Figure 2.7. Photoluminescence emission spectra of (a) Tb-UiO-66, (b) Eu-UiO-66, (c) Gd-UiO-66, and (d) the normalized emission spectra of (a), (b) and (c).

The excited state energy, energy transfer pathways, and emissive states in RE-UiO-66 analogues can be visualized in Figure 2.8.
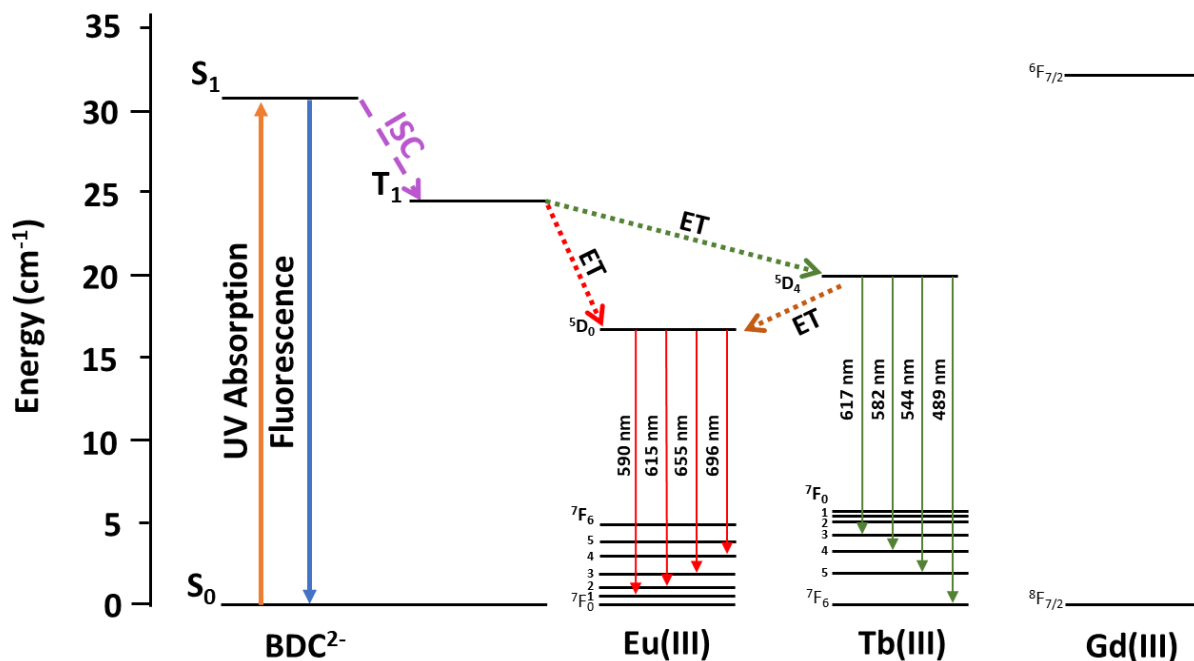
Figure 2.8. Jablonski diagram depicting the excited state energies and the transfer of energies for Eu(III), Tb(III), and Gd(III) and BDC^{2-}.

The BDC^{2-} linker acts as the light harvester, with absorbance spanning 200-400 nm (Figure 2.9a), giving rise to an excited singlet state of the linker. Owing to the presence of heavy RE(III) ions, intersystem crossing (ISC) occurs and gives rise to the T_1 state of BDC^{2-}. This is followed by non-radiative energy transfer, also known as the antenna effect, from the BDC^{2-} T_1 state to the 4f excited states of RE(III) ions.
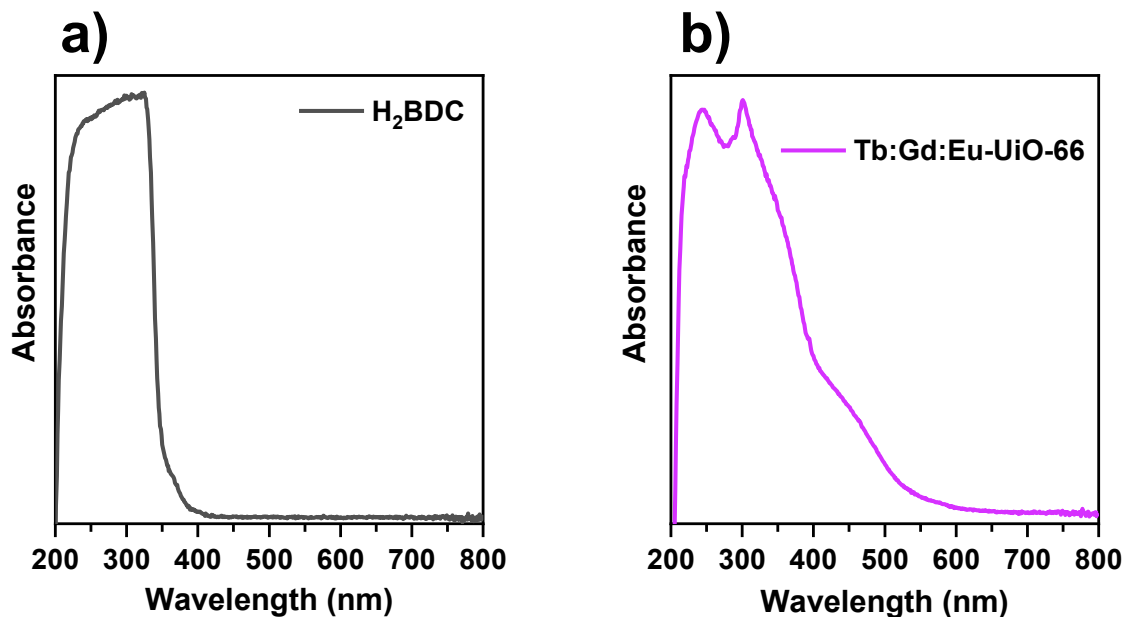
Figure 2.9. Diffuse reflectance UV-Vis spectrum of (a) H_2BDC and (b) Tb:Gd:Eu-UiO-66.

Working towards a white light emitting (RGB) RE-UiO-66, bi-metal analogues of the MOF were first studied to gain information about the antenna effect in mixed metal RE-UiO-66. In Eu:Gd-UiO-66 (Figure 2.10a), the blue emission (λ_{em} = 350-500 nm) from the linker is more intense than that observed for Eu-UiO-66 (Figure 2.7b), thus demonstrating that the presence of Gd(III) gives rise to less efficient energy transfer from the BDC^{2-} linker T_1 state to the Eu(III) $^5D_0$, $^5D_1$ and $^5D_2$ states. Tb:Gd-UiO-66 (Figure 2.10b) exhibits the same photoluminescence emission as Tb-UiO-66 (Figure 2.7a), meaning that the presence of Gd(III) does not significantly alter the efficiency of the energy transfer from the BDC^{2-} linker T_1 state to the Tb(III) $^5D_4$ state. The photoluminescence emission spectrum of Tb:Eu-UiO-66 (Figure 2.10c) has a weak blue emission (λ_{em} = 350-500 nm) from the linker, in contrast to Tb-UiO-66 and Tb:Gd-UiO-66, which suggests that energy transfer from Tb(III) to Eu(III) might be more efficient than that of the BDC^{2-} linker T_1 state to Tb(III). Both Eu(III) and Tb(III) transitions are observed in the emission spectrum of Tb:Eu-UiO-66 with an overlap of the $^5D_4 \rightarrow {}^7F_3$ transition of Tb(III) and $^5D_0 \rightarrow {}^7F_1$ transition of Eu(III), hence displaying emission in the blue, green, and red regions.
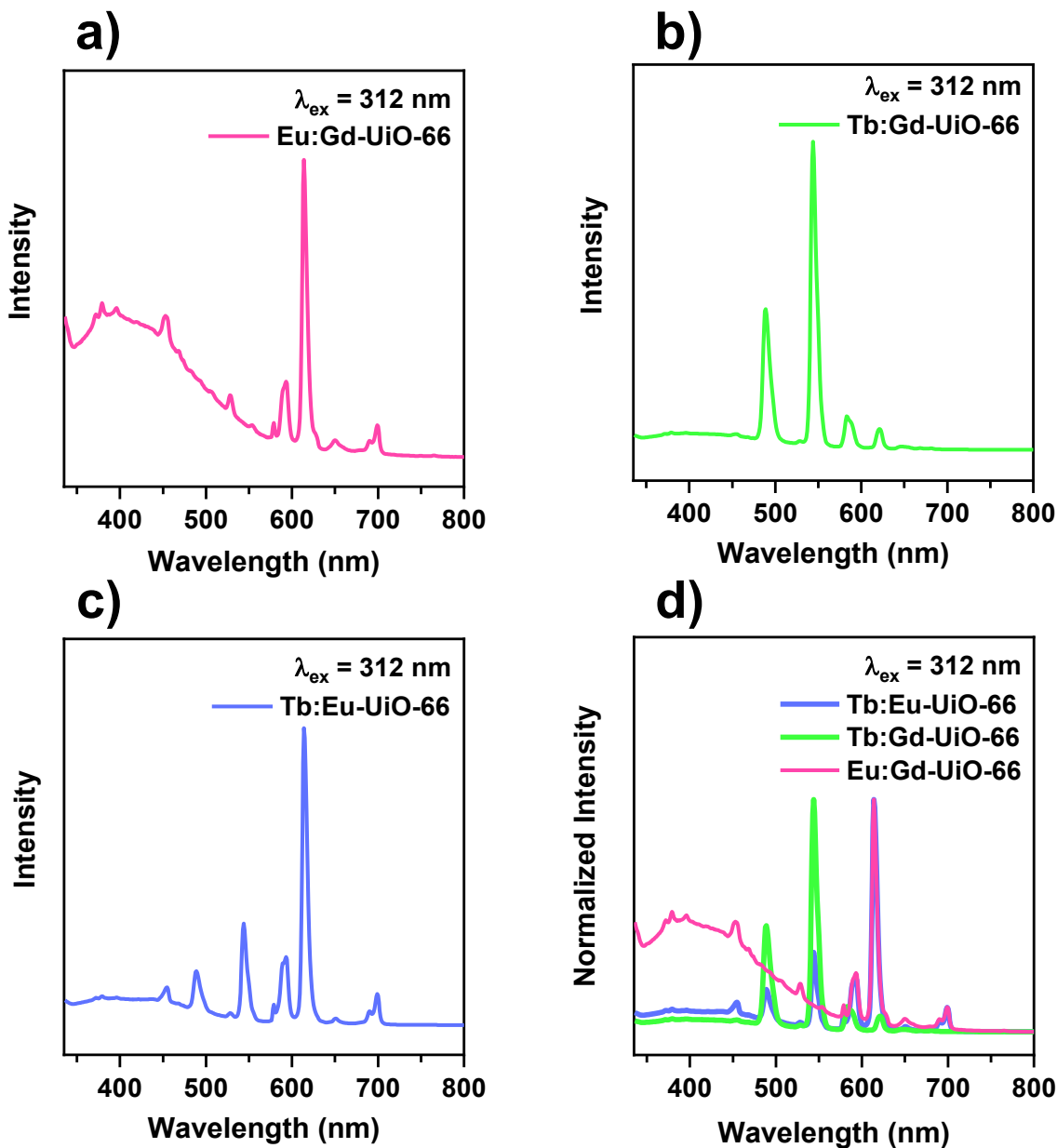
Figure 2.10. Photoluminescence emission spectra of (a) Tb:Gd-UiO-66, (b) Tb:Eu-UiO-66, (c) Eu:Gd-UiO-66, and (d) the normalized emission spectra of (a), (b) and (c).

Given that green, blue, and red emission is observed in Tb-UiO-66, Gd-UiO-66, and Eu-UiO-66, respectively, as well as in the bi-metal RE-UiO-66 analogues, we reasoned that a judicious mixture of Tb:Gd:Eu should give rise to white light emission. Indeed, the tri-metal RE-UiO-66 analogues composed of Tb(III), Gd(III) and Eu(III) (Tb:Gd:Eu-UiO-66), demonstrate strong blue emission from the linker, narrow green emission from Tb(III), and narrow red emission from

Eu(III) (Figure 2.11a) when excited into the BDC^{2-} linker at 312 nm. Tuning the composition of Tb:Gd:Eu to 3.3:9.6:1 gives an even distribution of green, blue, and red emission simultaneously, giving rise to white-light emission with the CIE 1931 color coordinate of x = 0.3103, y = 0.3901, corresponding to a cool white colour (Figure 2.11b,c).
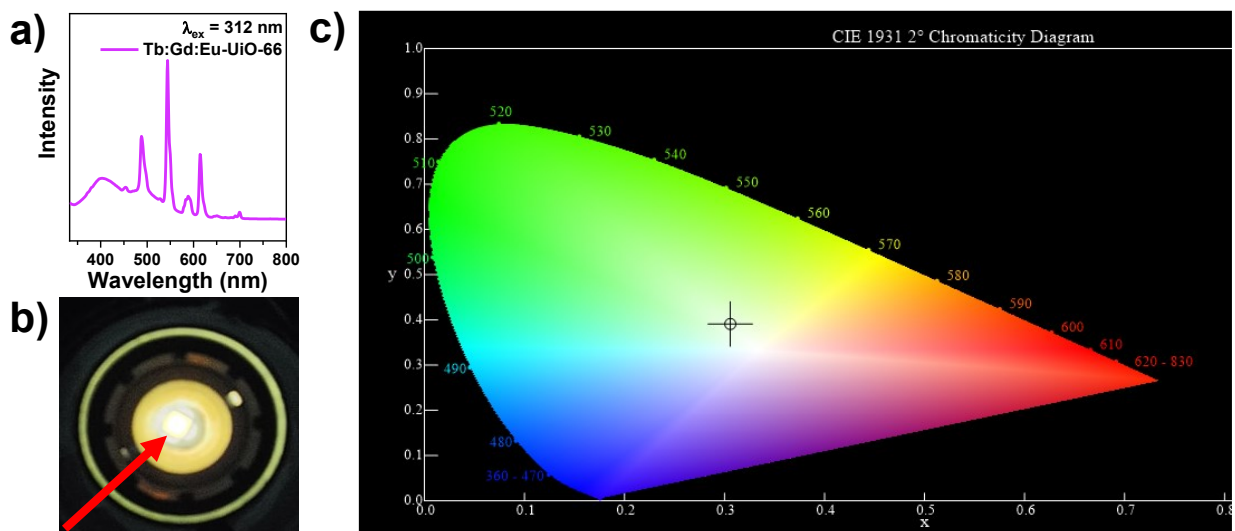
Figure 2.11. (a) Photoluminescence spectrum of Tb:Gd:Eu-UiO-66. (b) Photograph of Tb:Gd:Eu-UiO-66 on a LED flashlight exciting at 310nm. (c) CIE diagram of the photoluminescence coordinated of Tb:Gd:Eu-UiO-66.

2.4. Conclusions

In conclusion, the photoluminescence behaviour of RE-UiO-66 is tuned through the incorporation of bi-metal and tri-metal RE$_6$-nodes, ultimately leading to the formation of a white light emitting MOF. The structure and phase purity of the MOF is confirmed with PXRD, and the experimental BET demonstrates relatively high surface areas. The elemental ratios were further investigated with ICP-MS and was found to be in agreement with the ratios from SEM-EDS. In addition, a ternary system (Tb:Gd:Eu-UiO-66) was found to be necessary for the production of a white light emitting MOF.

Chapter 3

Modulating Photo- and Radioluminescence in Tb(III) Cluster-Based Metal–Organic Frameworks

3.1. Introduction

Luminescent materials are of interest for sensing,[206] security,[207] bioimaging,[19] solid-state lighting,[208] and other applications. Radioluminescent (RL) materials, in particular, emit light upon excitation with ionizing radiation. Radioluminescence arising from X-ray excitation is of interest for applications in dosimetry,[209] theranostics,[147] and security.[210] RL materials can be categorized as inorganic or organic.[211] In pure inorganic materials, radioluminescence is a property of the host material, with high Z elements used to attenuate X-rays through the photoelectric effect to give luminescence. In contrast, radioluminescence of organic materials arises from individual molecules, and the low Z nature of these materials results in inherently low X-ray absorption efficiencies. Thus, inorganic RL materials tend to have higher light output, while organic RL materials have more opportunity for color tunability through functional group modulation.[212]

Metal–organic frameworks (MOFs) are porous, often crystalline, materials[1, 5, 6, 213] that have the potential to bridge the properties of traditional inorganic and organic RL materials. The metal nodes in MOFs can either be ion[33, 214], chain,[175, 215] or cluster-based[74, 216] with varying nuclearity, geometry, and connectivity. By controlling the identity of the metal node and organic linker, MOFs with tuneable luminescent properties can be obtained.[139, 217] To date, the majority of reported RL MOFs utilize high-Z metal nodes for X-ray attenuation, and organic linkers as the emitting species.[147, 149-152, 209] More recently, lanthanoid-based MOFs comprised of metal ion nodes have been shown to demonstrate metal-based radioluminescence.[153,154]

Herein, we report the photoluminescent and radioluminescent properties of three lanthanoid cluster-based MOFs, Tb-UiO-66 (Figure 3.1a)[192], Tb-CU-10 (Figure 3.1b),[99] and the novel Tb-CU-27 (Figure 3.1c), which demonstrate metal-based, linker-based, and metal+linker based radioluminescence, respectively. The presence of multinuclear cluster nodes in these MOFs allows for strong X-ray attenuation while the varying triplet state energies of the linkers result in drastically different photo- and radioluminescence spectra. A comparison of their photophysical properties is presented, including an evaluation of radiation hardness up to 200 Gy.
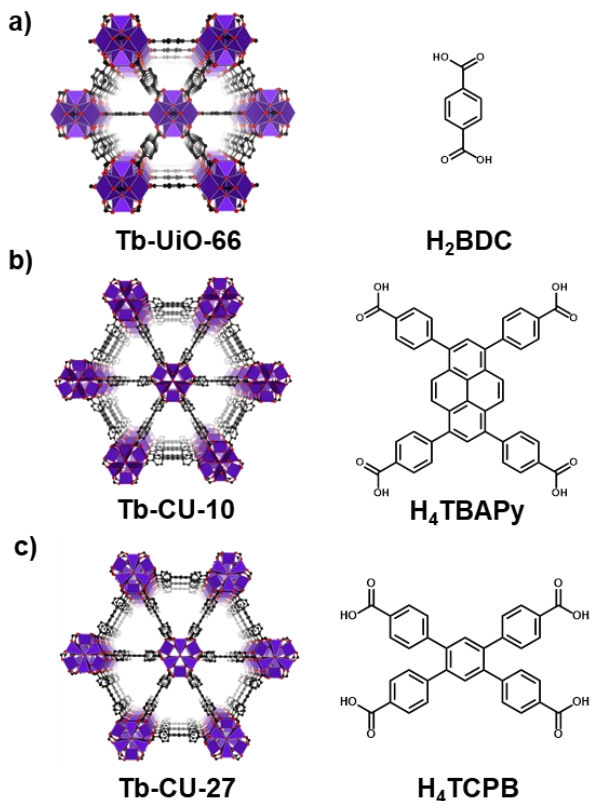
Figure 3.1. Structures and organic linker component of (a) Tb-UiO-66, (b) Tb-CU-10, and (c) Tb-CU-27.

3.2. Experimental Procedures

3.2.1. General Materials and Methods

All chemicals were used as received from commercial sources. *N,N'*-dimethylformamide (DMF), *N,N'*-dimethylacetamide (DMA), acetone, methanol, nitric acid, glacial acetic acid (HAc) were purchased from Fisher Scientific (Fisher Chemical). 2-Fluorobenzoic acid (2-FBA) and 2,6-difluorobenzoic acid (2,6-DFBA) were purchased from AmBeed. Terbium(III) nitrate hydrate (Tb(NO$_3$)$_3$•xH$_2$O) was purchased from Alfa Aesar. 1,4-Benzenedicarboxylic acid (H$_2$BDC) was purchased from Acros Organics. 1,2,4,5-tetrakis(4-carboxylphenyl)benzene (H$_4$TCPB) was purchased from Combi-Blocks. The 4,4',4'',4'''-(pyrene-1,3,6,8-tetrayl)tetrabenzoic acid (H$_4$TBAPy) linker was synthesized following a reported procedure.[218]

Single-crystal X-ray diffraction (SCXRD) data of Tb-CU-27, and Tb-UiO-66 were collected on a Bruker D8 Venture diffractometer equipped with a Photon 200 area detector and *IμS* microfocus X-ray source (Bruker AXS, Cu*K*α source). The crystals were coated with a

thin layer of amorphous oil to decrease crystal deterioration, structural disorder, or any related thermal motion effects and improve the accuracy of the structural results. Crystals were mounted at room temperature (298K). Structure solution was carried out using the SHELXTL package from Bruker.[219] The parameters were refined for all data by full-matrix-least squares or F^2 using SHELXL.[220] The crystals of Tb-CU-27 exhibited strong diffuse scattering in the form of diffuse Bragg peaks and scattering between them. The presence of diffuse scattering created defects in the crystal structures from complex disorder, particularly on the nonanuclear cluster that could not be modeled. Disordered phenyl rings and their corresponding carboxylate functionalities were split and successfully modeled. Strong diffuse scattering was also observed in Tb-UiO-66 in the precession images, and it is located in between Bragg reflections. Structures Tb-CU-27 and Tb-UiO-66 contain disordered molecules in the MOF pores, which could not be reliably modeled using discrete atoms, were subtracted by SQUEEZE, using the PLATON software.[221] In addition, both crystals were tested for possible twinning in the structure; however, no suitable twin law was found. Finally, the crystals consist of small thermal displacement ellipsoid parameters around the bridging atoms between the Tb-atoms in the cluster. This observation agrees with the recent report by Vizuet *et al.*[82] Therefore, we re-examined the crystals and replaced the bridging O-atoms with F-atoms. As a result, we generated new CIF files of Tb(F)-CU-27, and Tb(F)-UiO-66, and of our previously reported Tb(F)-CU-10,[99] see Table A.1. The crystallographic models remain intact, and we obtained more reasonable thermal displacement ellipsoids at the bridging position. All the nonhydrogen atoms were refined with anisotropic thermal parameters. Hydrogen atoms were placed in calculated positions and allowed to ride on the carrier atoms. All hydrogen atom thermal parameters were constrained to ride on the carrier atom. The crystal structure of Tb-CU-10 with bridging atoms was previously reported by our group (CSD: 1998091).[99]

Powder X-ray diffraction (PXRD) patterns were collected on a Bruker D2 Phaser diffractometer (measurements made over a range of 4° < 2θ < 40° in 0.02° step with a 0.200 s scanning speed) equipped with a LYNEXE linear position sensitive detector (Bruker AXS, Madison, WI). Neat samples were smeared directly onto the silicon wafer of a propriety low-zero background sample holder. Data was collected using a continuous coupled θ/2θ scan with Cu*K*α (λ = 1.54178 Å) radiation source. PXRD patterns were collected on a Bruker D8 Advance diffractometer (measurement made over a range of 3° < 2θ < 40° in 0.02° step with a 0.200 s scanning speed) equipped with a LYNXEYE linear position sensitive detector (Bruker AXS,

Madison, WI). Neat samples were smeared directly onto the silicon wafer of a propriety low-zero background sample holder. Data was collected using a continuous coupled $\theta/2\theta$ scan with Ni-filtered CuKα (λ = 1.54178 Å radiation operating at 40 kV and 40 mA).

MOF samples were activated using a Micromeritics Smart VacPrep instrument equipped with a hybrid turbo vacuum pump. Nitrogen adsorption-desorption isotherms were measured at 77 K on a Micromeritics TriStar II Plus instrument.

Diffuse reflectance infrared Fourier transformed spectroscopy (DRIFTS) data were recorded using a Thermo Scientific Nicolet 6700 FT-IR equipped with a MCT detector with a resolution of 1 cm^{-1} in the range of 4000-450 cm^{-1}. The samples were run after activation with no further treatment.

Scanning electron microscopy (SEM) images were collected on a Phenom ProX desktop SEM.

^{1}H-NMR spectroscopy data were collected on a 300 MHz Bruker spectrometer and the chemical shifts were referenced to the residual solvent peaks. Samples were digested by adding 10 drops of D_2SO_4, followed by sonicating for 10 minutes. Furthermore, 1.0 mL of DMSO-D_6 was added and the sample solution was loaded into the NMR tube.

Thermogravimetric analysis (TGA) was carried out in a TGA 5500 thermogravimetric analyzer by TA Instruments from room temperature to 800 °C at a rate of 10 °C/min under air.

Diffuse reflectance UV-Vis absorption spectroscopy data were collected on a Cary 5 Series UV-Vis-NIR Spectrophotometer (Agilent Technologies) with the EasiDiff^{TM} accessory. A 1 nm bandwidth and wavelength changeover at 350 nm were used for data collection. Samples were loaded into a sample cup with potassium bromide.

3.2.2. Synthesis

Tb-UiO-66 was synthesized through a solvothermal synthesis with a suspension of Tb(NO$_3$)$_3$•xH$_2$O (0.174 mmol, 75.5 mg), H$_2$BDC (0.171 mmol, 28.5 mg) and 2,6-difluorobenzoic acid (2.78 mmol, 440 mg) in 8 mL of *N,N*-dimethylacetamide (DMA) in an 8-dram vial. The mixture was sonicated until the reagents dissolved and was placed in a 120 °C oven for 72 hours. Once out of the oven, the solution was cooled to room temperature before centrifugation followed by washing with fresh DMF over the course of 24 hours and later with fresh acetone over the course of 2 days. The material was dried in a vacuum oven at 80 °C for 1 hour and then activated at 120 °C for 20 hours using a Micromeritics Smart VacPrep instrument.

Tb-CU-10 was synthesized through a solvothermal synthesis with a suspension of Tb(NO$_3$)$_3$•xH$_2$O (0.147 mmol, 63.8 mg), H$_4$TBAPy (0.0367 mmol, 25 mg) and 2-fluorobenzoic acid (18.3 mmol, 2567.9 mg) was prepared in 12.8 mL of DMF and 2.94 mL acetic acid in an 8-dram vial. The mixture was sonicated for 10 minutes to obtain a fine suspension and was paced in a 120 °C oven for 72 hours. Once out of the oven, the solution was cooled to room temperature before centrifugation followed by washing with fresh DMF over the course of 24 hours and later with fresh methanol over the course of 24 hours, and later with acetone over the course of 24 hours. The material was dried in a vacuum oven at 80 °C for 1 hour and then activated at 120 °C for 24 hours using a Micromeritics Smart VacPrep instrument.

Tb-CU-27 was synthesized through a solvothermal synthesis with a suspension of Tb(NO$_3$)$_3$•xH$_2$O (0.0737 mmol, 32 mg), 1,2,4,5-tetrakis-4-carboxyphenyl(benzene) (0.0179 mmol, 10.0 mg) and 2-fluorobenzoic acid (14.7 mmol, 2062.7 mg) was prepared in 6.6 mL of DMF and 1.53 mL acetic acid in an 8-dram vial. The mixture was sonicated until the reagents dissolved and was placed in a 120 °C oven for 72 hours. Once out of the oven, the solution was cooled to room temperature before centrifugation followed by washing with fresh DMF over the course of 24 hours and later with fresh methanol over the course of 2 days. The material was dried in a vacuum oven at 80 °C for 1 hour and then activated at 120 °C for 20 hours using a Micromeritics Smart VacPrep instrument.

3.3. Results and Discussion

Three Tb(III)-MOFs were chosen for the present study owing to the variation in triplet excited state energy (T$_1$) of the structural organic linker. Tb-UiO-66, Tb-CU-10, and Tb-CU-27 are formed using 1,4-benzenedicarboxylic acid (H$_2$BDC), 1,3,6,8-tetrakis(p-benzoate)-pyrene (H$_4$TBAPy), and 1,2,4,5-tetrakis(4-carboxyphenyl)benzene (H$_4$TCPB), which have T$_1$ energies of 25 641,[133, 195] 16 938,[222] and 21 589 cm^{-1},[223] respectively (Figure 3.2). Given that these linker energies are higher, lower, and resonant with the ^{5}D$_4$ state of Tb(III) (20 490 cm^{-1}), in conjunction with the high density of Tb(III) ions in the metal cluster nodes, we anticipated a range of photoluminescent and radioluminescent properties across the series.
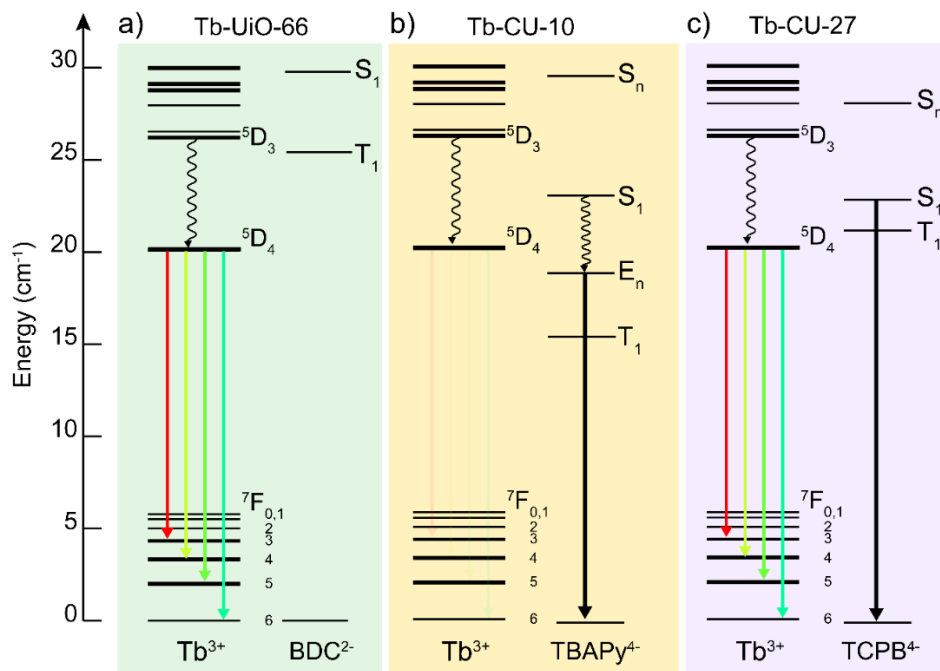
Figure 3.2. Jablonski diagram depicting the excited state energies for Tb^{3+} and each organic linker for (a) Tb-UiO-66, (b) Tb-CU-10 and (c) Tb-CU-27

Tb-UiO-66 and Tb-CU-10 have been previously reported by our group,[99, 192] and Tb-CU-27 is a novel MOF that is a structural analogue of Y-**shp**-MOF-5.[78] Tb-UiO-66 is a lanthanoid analogue of the archetypical Zr-UiO-66, which is comprised of hexanuclear clusters bridged by ditopic linkers to give the **fcu** topology (Figure 3.1a). Tb-CU-10 and Tb-CU-27 are isoreticular and comprised of Tb_9-cluster nodes bridged by tetratopic linkers giving rise to the **shp** topology (Figure 3.1b,c).

Tb-UiO-66, Tb-CU-10, and Tb-CU-27 are synthesized under solvothermal conditions using $Tb(NO_3)_3 \cdot xH_2O$, a fluorinated modulator, and the respective organic linker. The phase purity of each MOF is confirmed by powder X-ray diffraction (PXRD) using simulated patterns as a comparison (Figure 3.3, Figure A.1). Single-crystal X-ray diffraction (SCXRD) of the novel Tb-CU-27 shows a disordered nonanuclear metal cluster node that is 12-connected (Figure 3.4), and an overall **shp** topology (Figure A.2), similar to that observed in Y-**shp**-MOF-5,[78] and Tb-CU-10.[99]
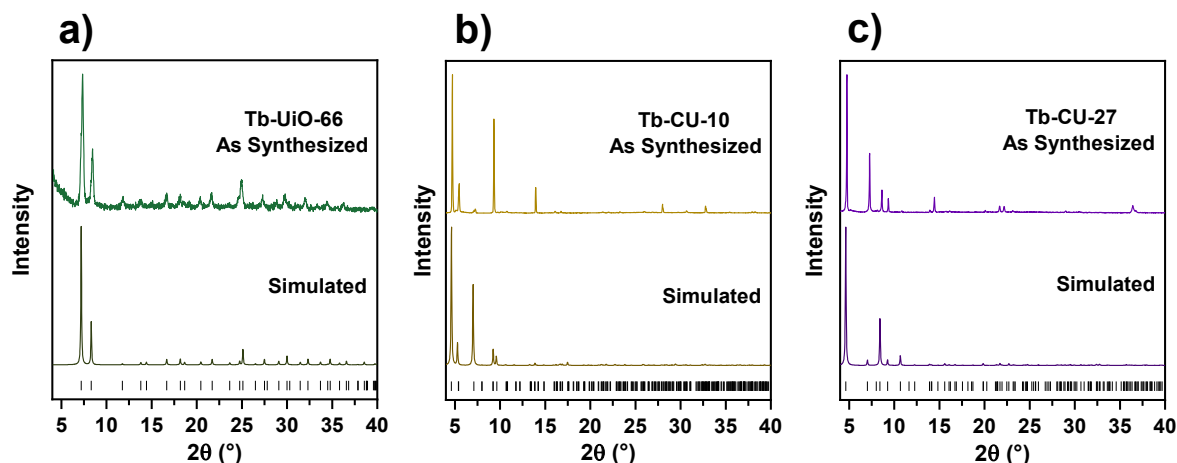
Figure 3.3. Powder X-ray diffractograms of (a) Tb-UiO-66, (b) Tb-CU-10 and (c) Tb-CU-27.
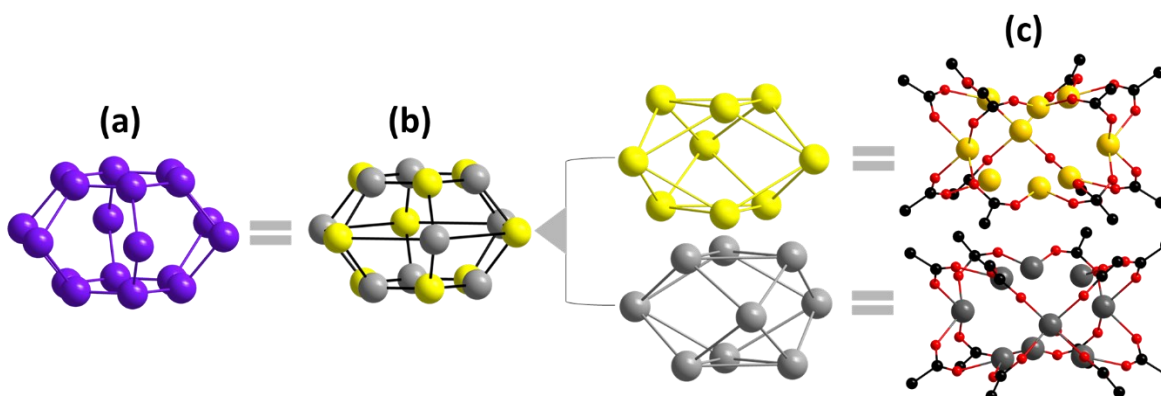
Figure 3.4. Representation of the disordered RE_9 cluster in Tb-CU-27 with the (a) observed RE_{18} cluster, (b) assignment of the two disordered RE_9 highlighting the two different orientations (yellow and grey), and (c) their corresponding individual arrangements.

SCXRD of Tb-UiO-66 reveals the expected 12-connected hexanuclear metal cluster node and **fcu** topology (Figure A.3). Scanning electron microscopy (SEM) images of Tb-CU-27 and Tb-CU-10 show hexagonal-shaped particles of 120 μm and 240 μm, respectively (Figure 3.5a,b) and Tb-UiO-66 show octahedral particles of 25 μm (Figure 3.5c).
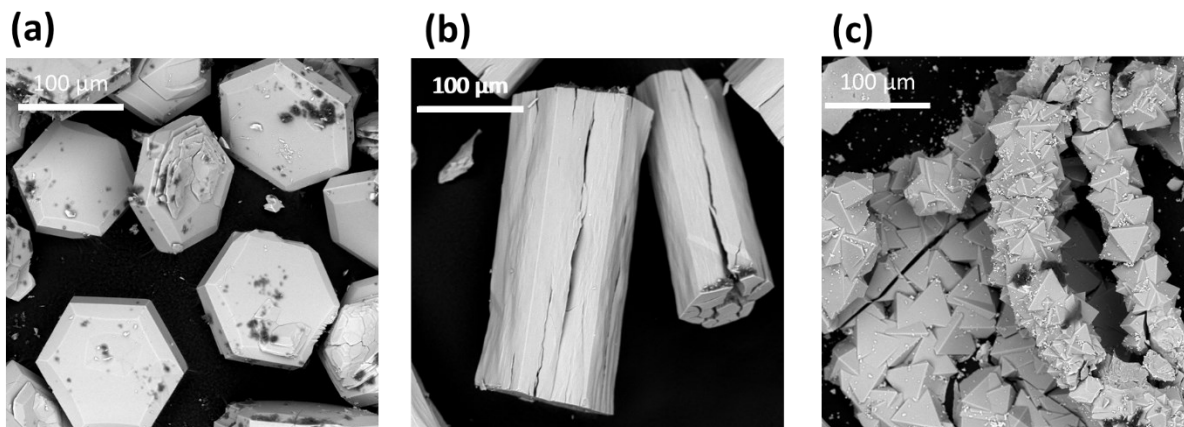
Figure 3.5. SEM micrographs of (a) Tb-CU-27, (b) Tb-CU-10, (c) Tb-UiO-66.

Nitrogen adsorption analyses of Tb-UiO-66, Tb-CU-10, and Tb-CU-27, show reversible Type-I isotherms (Figure 3.6) with calculated BET surface areas and pore diameters of 840 m^2/g and 10 Å, 1665 m^2/g and 11 Å, and 1365 m^2/g and 11 Å, respectively.
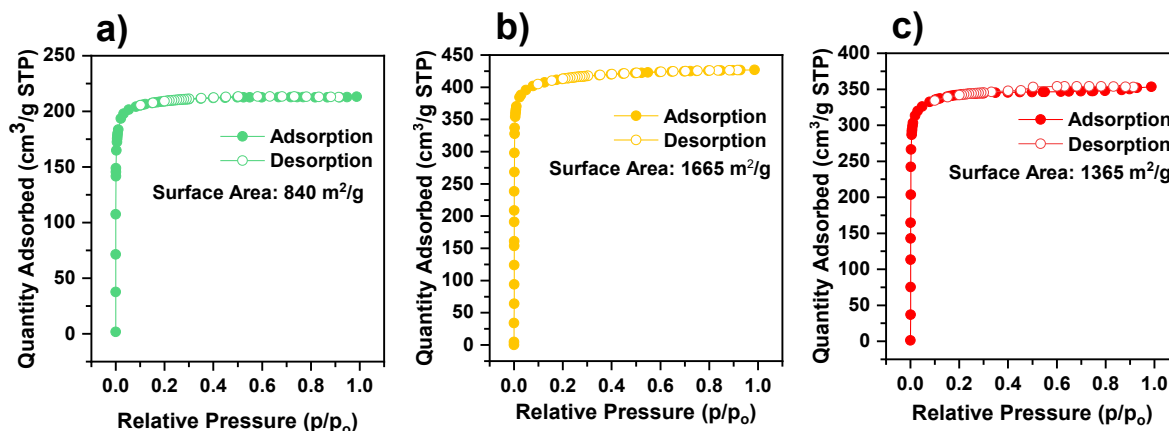
Figure 3.6. Nitrogen adsorption-desorption isotherms of (a) Tb-UiO-66, (b) Tb-CU-10 and (c) Tb-CU-27.

Diffuse reflectance infrared Fourier transform spectroscopy (DRIFTS) (Figure A.4), ^{1}H-NMR spectroscopy (Figure A.5), and thermogravimetric analysis (TGA) (Figure A.6) of Tb-CU-27 are consistent with a formula of DMA[Tb$_9$(μ_3-X)$_{12}$(μ_3-O)$_2$(TCPB)$_3$]·DMF where X = OH or F. We previously reported formulas of DMA$_2$[Tb$_6$(μ_3-OH)$_8$(BDC)$_6$] for Tb-UiO-66[192] and DMA$_3$[Tb$_9$(μ_3-OH)$_{12}$(μ_3-O)$_2$(TBAPy)$_3$(2-FBA)$_2$]·(DMF)(2-HFBA) for Tb-CU-10.[99] A recent study[82] suggested the possibility that the μ_3-OH groups in RE cluster-based MOFs synthesized using fluorinated modulators may be μ_3-F, which is difficult to distinguish crystallographically. As

such, we have solved the corresponding single-crystal X-ray structures with μ_3-F and μ_3-OH in all cases (see Table A.1 in the appendix).

The photoluminescence emission spectrum of Tb-UiO-66 upon 355 nm excitation exhibits characteristic emissions of Tb(III) corresponding to the $^5D_4 \rightarrow {}^7F_{3,4,5,6}$ transitions, respectively (Figure 3.7). Although the BDC^{2-} linker and Tb(III) are both excited at 355 nm (Figure A.7), Tb-UiO-66 exhibits no fluorescence or phosphorescence from the BDC^{2-} linker, owing to the energy of its triplet state (25 641 cm^{-1}) relative to the $^5D_4$ level of Tb(III) (20 490 cm^{-1}).[133, 195]
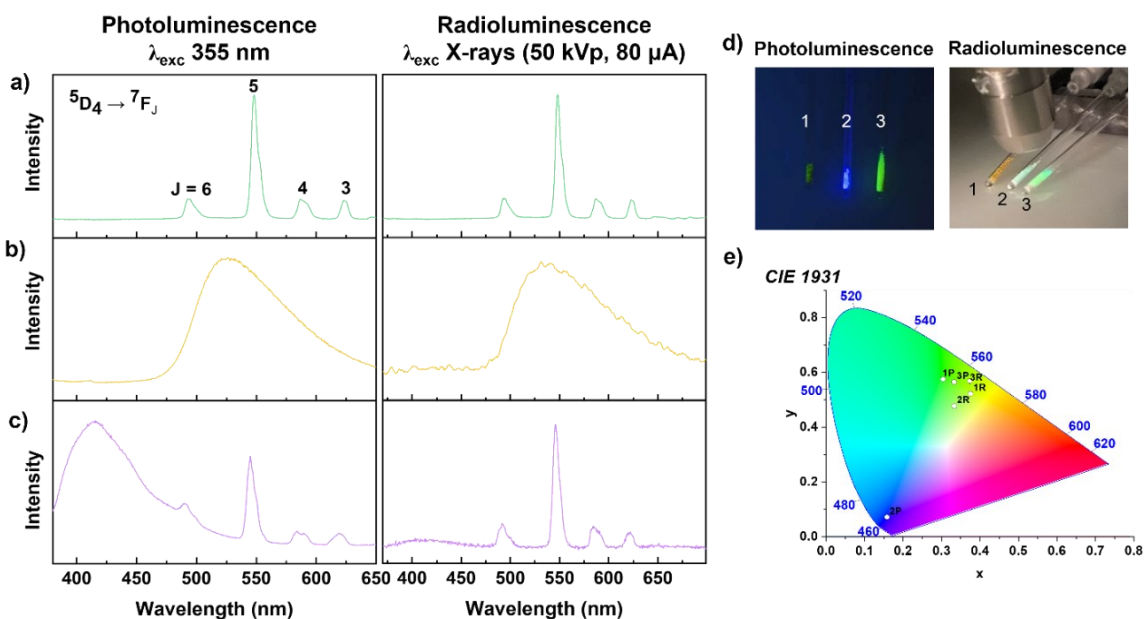
Figure 3.7. Photoluminescence (left) and radioluminescence (right) emission spectrum of (a) Tb-UiO-66, (b) Tb-CU-10, and (c) Tb-CU-27. Photographs of (1) Tb-CU-10, (2) Tb-CU-27 and (3) Tb-UiO-66 under UV (left) and X-ray (right) excitation. (e) CIE diagram of the photoluminescence (P) and radioluminescence (R) coordinates for each MOF.

Efficient intersystem crossing (ISC) and population of the T_1 state of BDC^{2-} is expected to be facilitated by the heavy atom effect, resulting in strong sensitization of Tb(III) emissions *via* the antenna effect in Tb-UiO-66. The decay time of the $^5D_4 \rightarrow {}^7F_5$ transition (545 nm) of Tb-UiO-66 upon 355 nm excitation is 1048.6 ± 6.93 μs (Figure 3.8), which is typical for Tb(III) $4f$-$4f$ transitions.[224-226]
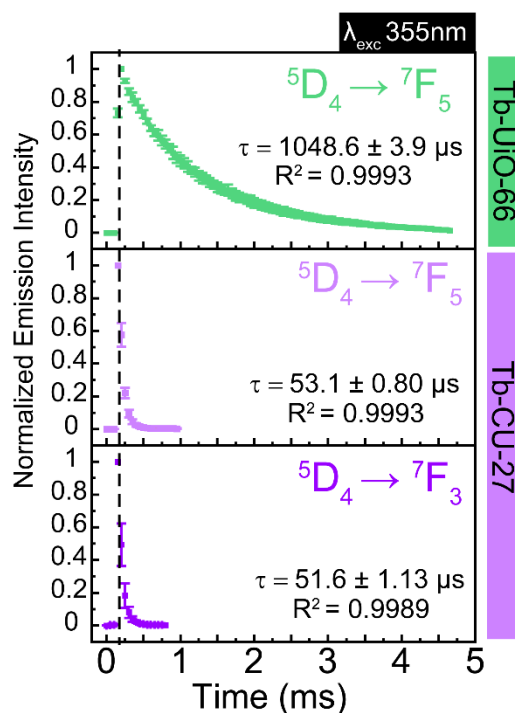
Figure 3.8. Lifetime of the $^5D_4 \rightarrow {}^7F_5$ transition of (a) Tb-UiO-66 and (b) Tb-CU-27 upon 355 nm excitation; (c) lifetime of the $^5D_4 \rightarrow {}^7F_3$ transition of Tb-CU-27 upon 355 nm excitation.

The radioluminescence emission spectrum of Tb-UiO-66 under 50 kVp, 80 μA unfiltered X-ray excitation (Au target) also exhibits characteristic Tb(III) emissions and no linker emission. Of all three MOFs, the radioluminescence intensity of Tb-UiO-66 is the most intense (Figure 3.7d, Figure A.8), indicative of high X-ray attenuation by the hexanuclear Tb(III)-clusters coupled with the highly efficient sensitization of Tb(III) from the triplet state of BDC^{2-}. The density and Z$_{eff}$ of the material (Figure A.9, Table A.2),[227] and lack of metal-to-ligand energy transfer (ET) facilitate strong X-ray attenuation and strong Tb(III)-based radioluminescence. As a control, all MOF starting materials were mixed in ratios similar to those found in each MOF, and no radioluminescence was observed, confirming that the multinuclear cluster node and overall network structure are required for efficient radioluminescence emission to occur (Figure A.10).

Tb-CU-10 exhibits a broad, featureless emission band at 525 nm upon excitation at 355 nm (into the $S_0 \rightarrow S_n$ bands of TBAPy^{4-}, Figure A.7) and upon X-ray excitation (Figure 3.7b). This broad emission band is characteristic of pyrene-based emission, with no features of Tb(III) emission observed. The triplet state of TBAPy^{4-} is significantly lower energy than the $^5D_4$ level of Tb(III), near 16 938 cm^{-1}.[222] It has been previously demonstrated that the use of ligands with low

energy triplet states in Tb(III) coordination compounds leads to quenching of Tb(III) luminescence.[228-231] Thus, the lack of Tb(III) emission in Tb-CU-10 is attributed to quenching from the pyrene linker.

The observed photo- and radioluminescence emission of Tb-CU-10, centered at 525 nm, is strongly red-shifted compared to the free linker (420 nm),[232] a commonly observed feature of excimer emission in pyrene-based MOFs.[233-235] Previous studies demonstrate that excimer formation in MOFs is favorable when the center-center distance between pyrene units is in the range of 8.8 – 11 Å, and the measured distance in Tb-CU-10 is 11 Å, in agreement with previous findings.[234] Furthermore, the pyrene-pyrene and pyrene-phenyl torsional angles are known to play a role in excimer formation,[234] where Tb-CU-10 exhibits torsional angles of 60 and 59° for pyrene-pyrene and pyrene-phenyl, respectively. These angles are similar to NU-1000 (60 and 50°), which is known to exhibit excimer emission.[234]

The weak linker-centered singlet excimer emission from Tb-CU-10 suggests efficient ISC and population of the linker triplet state may occur in the presence of Tb(III). This is corroborated by previously observed singlet oxygen production in this MOF, which is reliant on the population of the triplet state of the linker.[99] To further prove the role of the heavy atom effect on quenching the singlet excimer emission of the MOF, we synthesized Y-CU-10 and observed radioluminescence emission in the same position, but of significantly greater intensity (Figure 3.9). Since Y(III) is not considered a heavy atom compared to Tb(III), the rates of ISC are expected to be significantly reduced and thus singlet-state excimer emission becomes more favorable, resulting in the observed higher intensity.
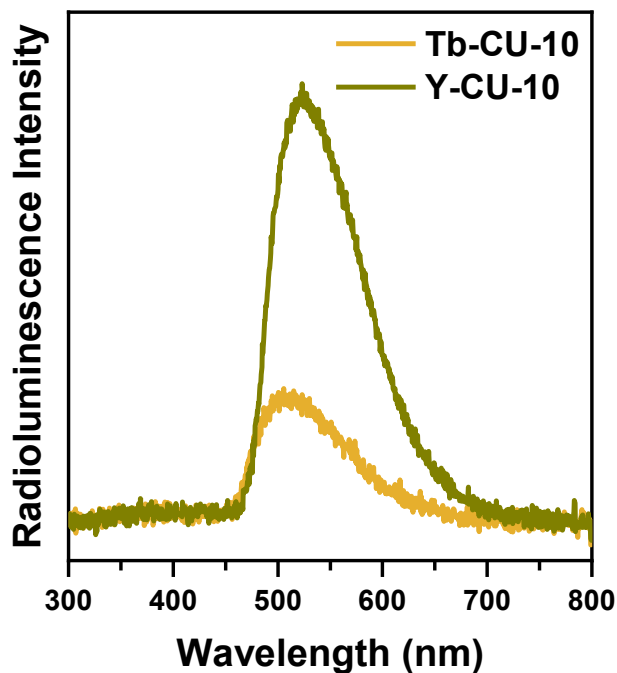
Figure 3.9. Radioluminescence emission intensities of Tb-CU-10 (yellow) and Y-CU-10 (green) under X-ray excitation (50 kVp, 80 μA, Au target, unfiltered beam).

The emission spectrum of Tb-CU-27 upon 355 nm excitation exhibits emission from both the $TCPB^{4-}$ linker and Tb(III) (Figure A.7c). Owing to the strong absorption bands of $TCPB^{4-}$ and Tb(III) at 355 nm (Figure A.7), and the potential for sensitization between $TCPB^{4-}$ and Tb(III), photoluminescence is observed from both metal and linker components. As observed with Tb-UiO-66, the population of the T_1 state of the linker leads to $T_1 \rightarrow$ Tb(III) ET and Tb(III) emission. The strong emission at 420 nm is attributed to the $S_1 \rightarrow S_0$ emission of $TCPB^{4-}$ (28 169 cm^{-1}),[223] which suggests inefficient ISC to the T_1 state, favoring radiative recombination[236] and indicating that the $S_1 \rightarrow T_1 \rightarrow$ Tb(III) ET pathway may not be the most prominent route. Interestingly, the lifetime of the $^5D_4 \rightarrow {}^7F_5$ transition of Tb(III) upon 355 nm excitation was found to be 53.1 ± 0.08 μs (Figure 3.8), which is relatively short for this transition.[224-226] Since the emission of $TCPB^{4-}$ overlaps with the $^5D_4 \rightarrow {}^7F_5$ transition at 545 nm, and has a short decay time (on the order of ps-ns), the lifetime of the $^5D_4 \rightarrow {}^7F_3$ transition of Tb(III) at 621 nm was also measured. The decay time of this transition was found to be 51.6 ± 1.13 μs, which is similar to the $^5D_4 \rightarrow {}^7F_5$ transition, and is still unexpectedly short for a Tb(III) decay time (Figure 3.8). A decreased decay time is associated with the introduction of a de-excitation pathway of the $^5D_4$ state, which can be

understood when one considers that the triplet state of $TCPB^{4-}$ is known to reside at 21 589 cm^{-1},[223] resonant with the $^5D_4$ level of Tb(III), resulting in efficient back ET from Tb(III) to $TCPB^{4-}$. Back ET from the $^5D_4$ state of Tb(III) is known to occur when the ligand triplet state energy is below 22 300 cm^{-1}, as is the case here.[146]

The radioluminescence and photoluminescence emission spectra of Tb-CU-27 are markedly different (Figure 3.7c). Upon X-ray excitation, the linker emission is less intense than the emission from Tb(III), which is in contrast to what is observed upon UV excitation. The different emission properties can also be visually observed (Figure 3.7d,e), where the MOF exhibits predominately blue photo- and green radioluminescence. This can be explained by considering the efficiency of X-ray attenuation of the Tb(III) clusters vs. the linkers. Low-energy photons are efficiently attenuated by high-density, high-Z_{eff} materials, thus the structure of a cluster-based MOF has regions of high (Tb(III) metal clusters) and low density/low Z_{eff} (pores and linkers), and it can be inferred that the majority of the incoming radiation is attenuated by the Tb(III) clusters. This is evidenced by strong Tb(III) radioluminescence and suggests the weak linker-based radioluminescence is due to secondary excitation. This postulation was confirmed by evaluating the radioluminescence spectrum of free $TCPB^{4-}$ (Figure A.11) where no radioluminescence was observed.

In order to assess the structural integrity of each MOF after extended doses of X-ray irradiation, radiation hardness measurements were performed on activated MOFs. Doses up to 200 Gy were delivered to the MOFs to evaluate their stability (Figure 3.10). Tb-UiO-66 was found to be radioresistant, exhibiting a 10 % loss of its radioluminescence intensity after exposure up to 200 Gy at a dose rate of 30 Gy/min (Figure 3.10a).
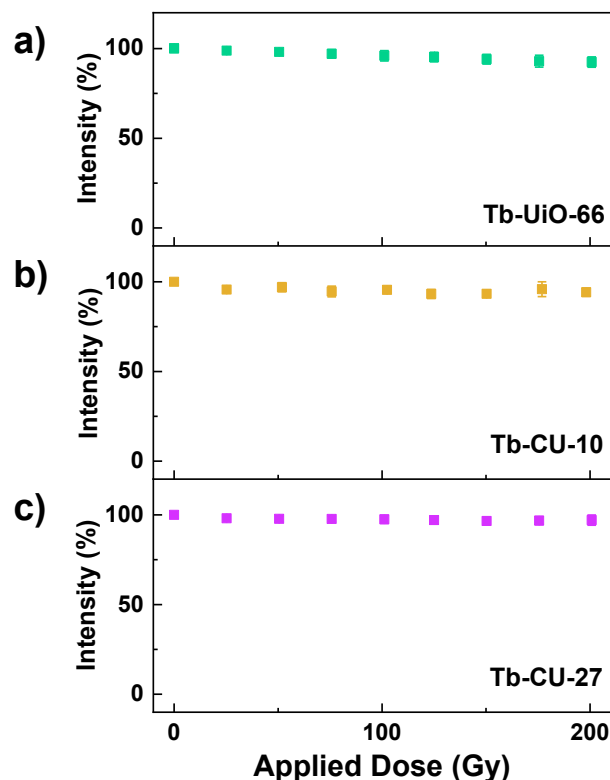
Figure 3.10. Radioluminescence intensity vs. applied X-ray dose of (a) Tb-UiO-66, (b) Tb-CU-10 and (c) Tb-CU-27.

The bulk crystallinity of Tb-UiO-66 remains intact (Figure 3.11a), although the BET surface area (Figure 3.12a) was found to decrease by approximately 24 % (from 840 to 640 m^2/g), which is consistent with previous observations related to the gradual collapse of this MOF after activation.[192] Tb-CU-10 and Tb-CU-27 were found to be highly radioresistant with minimal changes in radioluminescence intensity as a function of applied dose (Figure 3.10b,c). The bulk crystallinity of Tb-CU-10 and Tb-CU-27 remains intact after exposure to X-ray doses of 200 Gy (Figure 3.11b,c), and the BET surface areas only decreased by 5 % (from 1630 to 1540 m^2/g, Figure 3.12b) and 9 % (995 to 900 m^2/g , Figure 3.12c), respectively.
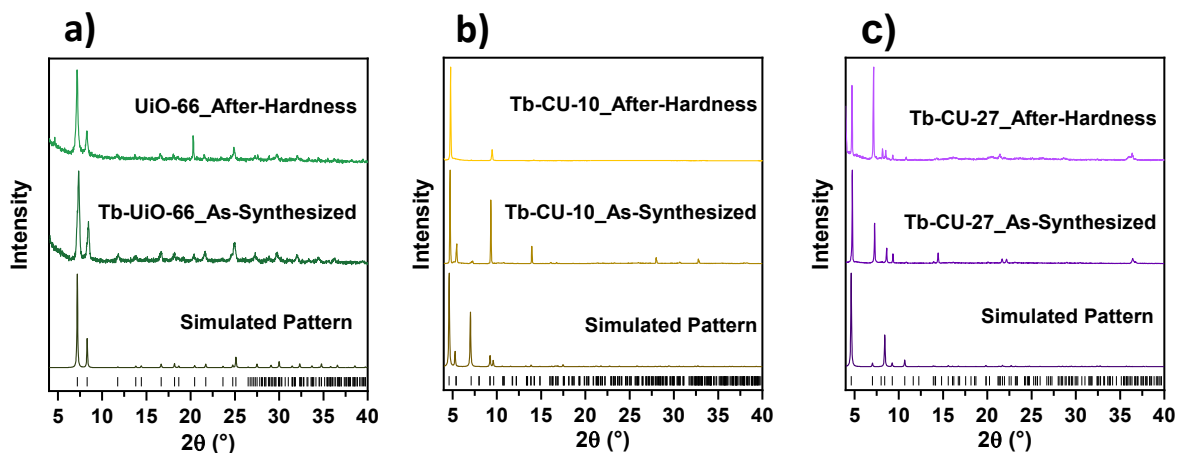
Figure 3.11. PXRD patterns (a) Tb-UiO-66 (b) Tb-CU-10, (c) Tb-CU-27 as synthesized MOFs, and after 200 Gy of irradiation at a rate of 30 Gy/min with their respective simulated patterns.
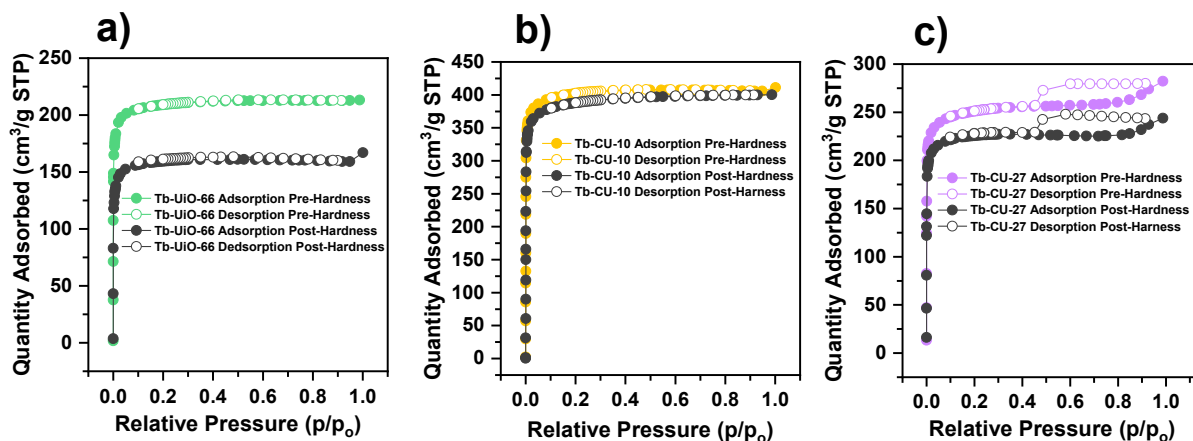
Figure 3.12. Nitrogen adsorption-desorption isotherms of (a) activated Tb-UiO-66 before irradiation (green) and after 200 Gy dose of irradiation at a rate of 30 Gy/min (black), (b) activated Tb-CU-10 before irradiation (yellow) and after 200 Gy dose of irradiation at a rate of 30 Gy/min (black), (c) activated Tb-CU-27 before irradiation (purple) and after 200 Gy dose of irradiation at a rate of 30 Gy/min (black).

3.4. Conclusions

In summary, three luminescent Tb(III)-cluster-based MOFs are reported, where the photoluminescent and radioluminescent behaviour arises from a combination of the multinuclear cluster nodes and judiciously chosen organic linkers. Each MOF demonstrates a different emission profile which is attributed to the differences in energies of the T_1 state of the organic linkers. Tb-

UiO-66 possesses strong Tb(III)-centered photo- and radioluminescence, Tb-CU-10 demonstrates weak excimer linker-based photo- and radioluminescence, and Tb-CU-27 shows linker and metal-based photo- and radioluminescence. In addition, all three MOFs remain stable upon X-ray irradiation with doses up to 200 Gy. This study highlights the utility of cluster-based MOFs in attenuating X-rays to produce radioluminescent materials, and the importance of the role of linker triplet state energies in modulating the photo- and radioluminescence properties of Tb(III)-based MOFs.

Chapter 4

Conclusions and Future Work

4.1. General Conclusions

In this work, the synthesis and characterization of RE-MOFs with multinuclear metal nodes is presented. The presence of high Z-metals in the metal cluster nodes coupled with linkers with varying triplet excited state energies, allows for a diverse set of photo- and radioluminescent MOFs to be synthesized and studied.

For the first time reported in literature, radioluminescence studies were performed on rare-earth cluster-based MOFs, where depending on the building blocks, different emission profiles were observed. In addition, the photoluminescence properties were also studied and thoroughly discussed. Two reported MOFs, Tb-UiO-66 and Tb-CU-10, were compared along with the novel MOF, Tb-CU-27. Tb-CU-27 is formed with the combination of Tb(III) and H_4TCPB in the presence of a fluorinated modulator, 2-FBA, which lead to the formation of a **shp** topology MOF. Single crystals of the MOF were also grown and allowed for a deeper analysis of the structure by SCXRD analysis. Full characterization was completed including PXRD, DRIFTS, ^{1}H-NMR, TGA, and nitrogen sorption studies by BET theory.

Using the RE-UiO-66 platform, a white light emitting MOF was synthesized. This was achieved using three different metals Gd(III), Tb(III) and Eu(III) in combination with the ditopic linker, H_2BDC. A thorough study of the photophysical properties has been completed through diffuse-reflectance UV-Vis and photoluminescence spectroscopy. Furthermore, single- and bi-metal RE-UiO-66 MOFs were also synthesized to further tune the emission window of the MOF.

4.2. Future Work

In interest of gaining a deeper insight into the photoluminescence and radioluminescence of the three MOFs (RE-UiO-66, RE-CU-10 and RE-CU-27), the whole RE series of the three MOFs should be compared. This would mean that the series of RE CU-27 MOFs should be fully synthesized and characterized. In addition, single crystals of the whole series of CU-27 should be grown for a comparison of all the RE-CU-27 family.

In order to further pursue the potential application of the white light emitting MOF, additional procedures to optimize the deposition of the MOF on the LED device should be carried out. In addition, increasing the stability of RE-UiO-66 should be pursued as to ensure a more robust

structure used in applications. An optimization of the activation conditions of RE-UiO-66 must be made to form MOFs with higher surface areas.

In regards to RE-UiO-66, RE-CU-10 and RE-CU-27, a thorough study on the photoluminescent decay times of the MOFs and their respective linkers should be completed. Furthermore, the quantum yield of the MOFs should be obtained.

With respect to the radioluminescence study, it would be interesting to take advantage of the emission observed to pursue a biological application with the radioluminescent MOFs, such as imaging.

References

1.   B. F. Hoskins and R. Robson, *J. Am. Chem. Soc.*, 1990, **112**, 1546-1554.

2.   P. Z. Moghadam, A. Li, S. B. Wiggin, A. Tao, A. G. P. Maloney, P. A. Wood, S. C. Ward and D. Fairen-Jimenez, *Chem. Mater.*, 2017, **29**, 2618-2625.

3.   O. M. Yaghi and H. Li, *J. Am. Chem. Soc.*, 1995, **117**, 10401-10402.

4.   O. M. Yaghi, G. Li and H. Li, *Nature*, 1995, **378**, 703-706.

5.   M. Kondo, T. Yoshitomi, H. Matsuzaka, S. Kitagawa and K. Seki, *Angew. Chem. Int. Ed.*, 1997, **36**, 1725-1727.

6.   H. Li, M. Eddaoudi, M. O'Keeffe and O. M. Yaghi, *Nature*, 1999, **402**, 276-279.

7.   N. L. Rosi, J. Kim, M. Eddaoudi, B. Chen, M. O'Keeffe and O. M. Yaghi, *J. Am. Chem. Soc.*, 2005, **127**, 1504-1518.

8.   N. Joseph, H. D. Lawson, K. J. Overholt, K. Damodaran, R. Gottardi, A. P. Acharya and S. R. Little, *Sci. Rep.*, 2019, **9**, 13024.

9.   L. Robison, L. Zhang, R. J. Drout, P. Li, C. R. Haney, A. Brikha, H. Noh, B. L. Mehdi, N. D. Browning, V. P. Dravid, Q. Cui, T. Islamoglu and O. K. Farha, *ACS Appl. Bio Mater.*, 2019, **2**, 1197-1203.

10.   G. Férey, M. Latroche, C. Serre, F. Millange, T. Loiseau and A. Percheron-Guégan, *Chem. Commun.*, 2003.

11.   K.-i. Otake, Y. Cui, C. T. Buru, Z. Li, J. T. Hupp and O. K. Farha, *J. Am. Chem. Soc.*, 2018, **140**, 8652-8656.

12.   D. Feng, Z.-Y. Gu, J.-R. Li, H.-L. Jiang, Z. Wei and H.-C. Zhou, *Angew. Chem. Int. Ed.*, 2012, **51**, 10307-10310.

13.   D. Feng, K. Wang, Z. Wei, Y.-P. Chen, C. M. Simon, R. K. Arvapally, R. L. Martin, M. Bosch, T.-F. Liu, S. Fordham, D. Yuan, M. A. Omary, M. Haranczyk, B. Smit and H.-C. Zhou, *Nat. Commun.*, 2014, **5**, 5723.

14.   A. Phan, C. J. Doonan, F. J. Uribe-Romo, C. B. Knobler, M. O'Keeffe and O. M. Yaghi, *Acc. Chem. Res*, 2010, **43**, 58-67.

15.   D.-X. Xue, A. J. Cairns, Y. Belmabkhout, L. Wojtas, Y. Liu, M. H. Alkordi and M. Eddaoudi, *J. Am. Chem. Soc.*, 2013, **135**, 7660-7667.

16.   E. A. Dolgopolova, A. M. Rice and N. B. Shustova, *Chem. Commun.*, 2018, **54**, 6472-6483.

17.   H. Li, K. Wang, Y. Sun, C. T. Lollar, J. Li and H.-C. Zhou, *Mater. Today*, 2018, **21**, 108-121.

18.   S.-N. Zhao, G. Wang, D. Poelman and P. V. Voort, *Materials*, 2018, **11**.

19.   F. Demir Duman and R. S. Forgan, *J. Mater. Chem. B.*, 2021, **9**, 3423-3449.

20.   O. M. Yaghi, M. O'Keeffe, N. W. Ockwig, H. K. Chae, M. Eddaoudi and J. Kim, *Nature*, 2003, **423**, 705-714.

21.   O. M. Yaghi, *J. Am. Chem. Soc.*, 2016, **138**, 15507-15509.

22.   O. M. Yaghi, *ACS Cent. Sci.*, 2019, **5**, 1295-1300.

23.   M. O'Keeffe and O. M. Yaghi, *Chem. Rev.*, 2012, **112**, 675-702.

24.   M. O'Keeffe, M. A. Peskov, S. J. Ramsden and O. M. Yaghi, *Acc. Chem. Res*, 2008, **41**, 1782-1789.

25.   M. O'Keeffe, *Chem. Soc. Rev.*, 2009, **38**, 1215-1217.

26.   L. Öhrström, *Crystals*, 2015, **5**.

27.   O. Delgado-Friedrichs, M. O'Keeffe and O. M. Yaghi, *Phys. Chem. Chem. Phys.*, 2007, **9**, 1035-1043.

28.   J.-C. G. Bünzli, *J. Coord. Chem.*, 2014, **67**, 3706-3733.

29.   T. M. Reineke, M. Eddaoudi, M. Fehr, D. Kelley and O. M. Yaghi, *J. Am. Chem. Soc.*, 1999, **121**, 1651-1657.

30.   C. Pagis, M. Ferbinteanu, G. Rothenberg and S. Tanase, *ACS Catal.*, 2016, **6**, 6063-6072.

31.   F. Saraci, V. Quezada-Novoa, P. R. Donnarumma and A. J. Howarth, *Chem. Soc. Rev.*, 2020, **49**, 7949-7977.

32.   D. J. Hoffart and S. J. Loeb, *Angew. Chem. Int. Ed.*, 2005, **44**, 901-904.

33.   Y. He, H. Furukawa, C. Wu, M. O'Keeffe and B. Chen, *CrystEngComm*, 2013, **15**, 9328-9331.

34.   M. Kumar, L.-H. Wu, M. Kariem, A. Franconetti, H. N. Sheikh, S.-J. Liu, S. C. Sahoo and A. Frontera, *Inorg. Chem.*, 2019, **58**, 7760-7774.

35.   N. E. Wong, P. Ramaswamy, A. S. Lee, B. S. Gelfand, K. J. Bladek, J. M. Taylor, D. M. Spasyuk and G. K. H. Shimizu, *J. Am. Chem. Soc.*, 2017, **139**, 14676-14683.

36.   J. Zhao, X. He, Y. Zhang, J. Zhu, X. Shen and D. Zhu, *Cryst. Growth Des.*, 2017, **17**, 5524-5532.

37.   A. Michaelides and S. Skoulika, *Cryst. Growth Des.*, 2005, **5**, 529-533.

38. Y.-Q. Sun, J. Zhang, Y.-M. Chen and G.-Y. Yang, *Angew. Chem. Int. Ed.*, 2005, **44**, 5814-5817.

39. Y. Li, S. Zhang and D. Song, *Angew. Chem. Int. Ed.*, 2013, **52**, 710-713.

40. T. Devic, C. Serre, N. Audebrand, J. Marrot and G. Férey, *J. Am. Chem. Soc.*, 2005, **127**, 12788-12789.

41. Y. Cui, H. Xu, Y. Yue, Z. Guo, J. Yu, Z. Chen, J. Gao, Y. Yang, G. Qian and B. Chen, *J. Am. Chem. Soc.*, 2012, **134**, 3979-3982.

42. Q. Tang, Y. Liu, S. Liu, D. He, J. Miao, X. Wang, G. Yang, Z. Shi and Z. Zheng, *J. Am. Chem. Soc.*, 2014, **136**, 12444-12449.

43. G. Tobin, S. Comby, N. Zhu, R. Clérac, T. Gunnlaugsson and W. Schmitt, *Chem. Commun.*, 2015, **51**, 13313-13316.

44. A. Schoedel, M. Li, D. Li, M. O'Keeffe and O. M. Yaghi, *Chem. Rev.*, 2016, **116**, 12466-12535.

45. T. M. Reineke, M. Eddaoudi, D. Moler, M. O'Keeffe and O. M. Yaghi, *J. Am. Chem. Soc.*, 2000, **122**, 4843-4844.

46. H. He, D. Yuan, H. Ma, D. Sun, G. Zhang and H.-C. Zhou, *Inorg. Chem.*, 2010, **49**, 7605-7607.

47. S.-M. Fang, E. C. Sañudo, M. Hu, Q. Zhang, S.-T. Ma, L.-R. Jia, C. Wang, J.-Y. Tang, M. Du and C.-S. Liu, *Cryst. Growth Des.*, 2011, **11**, 811-819.

48. J.-H. Liao, C.-S. Tsai and T.-K. Lin, *Inorg. Chem. Commun.*, 2010, **13**, 286-289.

49. S. Nayak, H. P. Nayek, C. Pietzonka, G. Novitchi and S. Dehnen, *J. Mol. Struct.*, 2011, **1004**, 82-87.

50. C. G. Efthymiou, E. J. Kyprianidou, C. J. Milios, M. J. Manos and A. J. Tasiopoulos, *J. Mater. Chem. A*, 2013, **1**, 5061-5069.

51. P. Mahata, K. V. Ramya and S. Natarajan, *Chem. Eur. J.*, 2008, **14**, 5839-5850.

52. N. Roques, D. Maspoch, I. Imaz, A. Datcu, J.-P. Sutter, C. Rovira and J. Veciana, *Chem. Commun.*, 2008.

53. S. Bhattacharjee, C. Chen and W.-S. Ahn, *RSC Adv.*, 2014, **4**, 52500-52525.

54. G. Férey, C. Serre, C. Mellot-Draznieks, F. Millange, S. Surblé, J. Dutour and I. Margiolaki, *Angew. Chem. Int. Ed.*, 2004, **43**, 6296-6301.

55. Y. Dezotti, M. A. Ribeiro, K. R. Pirota and W. P. Barros, *Cryst. Growth Des.*, 2019, **19**, 5592-5603.

56. A. Karmakar, S. Hazra, M. F. C. Guedes da Silva, A. Paul and A. J. L. Pombeiro, *CrystEngComm*, 2016, **18**, 1337-1349.

57. L. Zhang, T. Song, J. Xu, J. Sun, S. Zeng, Y. Wu, Y. Fan and L. Wang, *CrystEngComm*, 2014, **16**, 2440-2451.

58. A. C. Sudik, A. P. Côté and O. M. Yaghi, *Inorg. Chem.*, 2005, **44**, 2998-3000.

59. B.-Q. Ma, D.-S. Zhang, S. Gao, T.-Z. Jin, C.-H. Yan and G.-X. Xu, *Angew. Chem. Int. Ed.*, 2000, **39**, 3644-3646.

60. P. Wu, C. He, J. Wang, X. Peng, X. Li, Y. An and C. Duan, *J. Am. Chem. Soc.*, 2012, **134**, 14991-14999.

61. L. Han, S. Zhang, Y. Wang, X. Yan and X. Lu, *Inorg. Chem.*, 2009, **48**, 786-788.

62. X. Yi, K. Bernot, G. Calvez, C. Daiguebonne and O. Guillou, *Eur. J. Inorg. Chem*, 2013, **2013**, 5879-5885.

63. D. Savard, P.-H. Lin, T. J. Burchell, I. Korobkov, W. Wernsdorfer, R. Clérac and M. Murugesu, *Inorg. Chem.*, 2009, **48**, 11748-11754.

64. P. Silva, L. Cunha-Silva, N. J. O. Silva, J. Rocha and F. A. A. Paz, *Cryst. Growth Des.*, 2013, **13**, 2607-2617.

65. T.-Y. Luo, C. Liu, S. V. Eliseeva, P. F. Muldoon, S. Petoud and N. L. Rosi, *J. Am. Chem. Soc.*, 2017, **139**, 9333-9340.

66. D. Alezi, A. M. P. Peedikakkal, Ł. J. Weseliński, V. Guillerm, Y. Belmabkhout, A. J. Cairns, Z. Chen, Ł. Wojtas and M. Eddaoudi, *J. Am. Chem. Soc.*, 2015, **137**, 5421-5430.

67. L.-F. Chen, J. Zhang, G.-Q. Ren, L. Zhao-Ji, Y.-Y. Qin, P.-X. Yin, J.-K. Cheng and Y.-G. Yao, *CrystEngComm*, 2008, **10**, 1088-1092.

68. F.-N. Shi, L. Cunha-Silva, T. Trindade, F. A. A. Paz and J. Rocha, *Cryst. Growth Des.*, 2009, **9**, 2098-2109.

69. F. Gándara, E. Gutiérrez-Puebla, M. Iglesias, N. Snejko and M. Á. Monge, *Cryst. Growth Des.*, 2010, **10**, 128-134.

70. J. Demel, P. Kubát, F. Millange, J. Marrot, I. Císařová and K. Lang, *Inorg. Chem.*, 2013, **52**, 2779-2786.

71.   J. H. Cavka, S. Jakobsen, U. Olsbye, N. Guillou, C. Lamberti, S. Bordiga and K. P. Lillerud, *J. Am. Chem. Soc.*, 2008, **130**, 13850-13851.

72.   O. Yassine, O. Shekhah, A. H. Assen, Y. Belmabkhout, K. N. Salama and M. Eddaoudi, *Angew. Chem. Int. Ed.*, 2016, **55**, 15879-15883.

73.   A. H. Assen, Y. Belmabkhout, K. Adil, P. M. Bhatt, D.-X. Xue, H. Jiang and M. Eddaoudi, *Angew. Chem. Int. Ed.*, 2015, **54**, 14353-14358.

74.   R. Luebke, Y. Belmabkhout, Ł. J. Weseliński, A. J. Cairns, M. Alkordi, G. Norton, Ł. Wojtas, K. Adil and M. Eddaoudi, *Chem. Sci.*, 2015, **6**, 4095-4102.

75.   Y. Guo, L. Zhang, N. Muhammad, Y. Xu, Y. Zhou, F. Tang and S. Yang, *Inorg. Chem.*, 2018, **57**, 995-1003.

76.   W.-H. Fang, L. Cheng, L. Huang and G.-Y. Yang, *Inorg. Chem.*, 2013, **52**, 6-8.

77.   V. Guillerm, Ł. J. Weseliński, Y. Belmabkhout, A. J. Cairns, V. D'Elia, Ł. Wojtas, K. Adil and M. Eddaoudi, *Nat. Chem.*, 2014, **6**, 673-680.

78.   R. G. AbdulHalim, P. M. Bhatt, Y. Belmabkhout, A. Shkurenko, K. Adil, L. J. Barbour and M. Eddaoudi, *J. Am. Chem. Soc.*, 2017, **139**, 10715-10722.

79.   L. Feng, Y. Wang, K. Zhang, K.-Y. Wang, W. Fan, X. Wang, J. A. Powell, B. Guo, F. Dai, L. Zhang, R. Wang, D. Sun and H.-C. Zhou, *Angew. Chem. Int. Ed.*, 2019, **58**, 16682-16690.

80.   Y. Zhang, L. Huang, H. Miao, H. X. Wan, H. Mei, Y. Liu and Y. Xu, *Chem. Eur. J.*, 2015, **21**, 3234-3241.

81.   C. Liu, S. V. Eliseeva, T.-Y. Luo, P. F. Muldoon, S. Petoud and N. L. Rosi, *Chem. Sci.*, 2018, **9**, 8099-8102.

82.   J. P. Vizuet, M. L. Mortensen, A. L. Lewis, M. A. Wunch, H. R. Firouzi, G. T. McCandless and K. J. Balkus, *J. Am. Chem. Soc.*, 2021, **143**, 17995-18000.

83.   G. Calvez, C. Daiguebonne, O. Guillou and F. Le Dret, *Eur. J. Inorg. Chem.*, 2009, **2009**, 3172-3178.

84.   G. Giester, P. Unfried and Z. Žák, *J. Alloys Compd.*, 1997, **257**, 175-181.

85.   Z. Ẑák, P. Unfried and G. Giester, *J. Alloys Compd.*,, 1994, **205**, 235-242.

86.   D.-X. Xue, Y. Belmabkhout, O. Shekhah, H. Jiang, K. Adil, A. J. Cairns and M. Eddaoudi, *J. Am. Chem. Soc.*, 2015, **137**, 5034-5040.

87. M.-L. Gao, W.-J. Wang, L. Liu, Z.-B. Han, N. Wei, X.-M. Cao and D.-Q. Yuan, *Inorg. Chem.*, 2017, **56**, 511-517.

88. Y.-F. Zhang, D.-X. Xue, Z.-H. Zhang, Q. Li and Z. Gao, *Cryst. Growth Des.*, 2017, **17**, 1419-1424.

89. P. M. Bhatt, Y. Belmabkhout, A. H. Assen, Ł. J. Weseliński, H. Jiang, A. Cadiau, D.-X. Xue and M. Eddaoudi, *Chem. Eng.*, 2017, **324**, 392-396.

90. D. F. Sava Gallis, L. E. S. Rohwer, M. A. Rodriguez, M. C. Barnhart-Dailey, K. S. Butler, T. S. Luk, J. A. Timlin and K. W. Chapman, *ACS Appl. Mater. Interfaces*, 2017, **9**, 22268-22277.

91. X. Liu, B. Liu, G. Li and Y. Liu, *J. Mater. Chem. A*, 2018, **6**, 17177-17185.

92. P. De Luna, W. Liang, A. Mallick, O. Shekhah, F. P. García de Arquer, A. H. Proppe, P. Todorović, S. O. Kelley, E. H. Sargent and M. Eddaoudi, *ACS Appl. Mater. Interfaces*, 2018, **10**, 31225-31232.

93. W. Wei, X. Wang, K. Zhang, C.-B. Tian and S.-W. Du, *Cryst. Growth Des.*, 2019, **19**, 55-59.

94. D.-X. Xue, A. Cadiau, Ł. J. Weseliński, H. Jiang, P. M. Bhatt, A. Shkurenko, L. Wojtas, C. Zhijie, Y. Belmabkhout, K. Adil and M. Eddaoudi, *ChemComm.*, 2018, **54**, 6404-6407.

95. H. Jiang, J. Jia, A. Shkurenko, Z. Chen, K. Adil, Y. Belmabkhout, L. J. Weselinski, A. H. Assen, D.-X. Xue, M. O'Keeffe and M. Eddaoudi, *J. Am. Chem. Soc.*, 2018, **140**, 8858-8867.

96. L. Xu, M.-K. Zhai, F. Wang, L. Sun and H.-B. Du, *Dalton Trans.*, 2016, **45**, 17108-17112.

97. L. Zhang, S. Yuan, L. Feng, B. Guo, J.-S. Qin, B. Xu, C. Lollar, D. Sun and H.-C. Zhou, *Angew. Chem. Int. Ed.*, 2018, **57**, 5095-5099.

98. Z. Chen, Ł. J. Weseliński, K. Adil, Y. Belmabkhout, A. Shkurenko, H. Jiang, P. M. Bhatt, V. Guillerm, E. Dauzon, D.-X. Xue, M. O'Keeffe and M. Eddaoudi, *J. Am. Chem. Soc.*, 2017, **139**, 3265-3274.

99. V. Quezada-Novoa, H. M. Titi, A. A. Sarjeant and A. J. Howarth, *Chem. Mater.*, 2021, **33**, 4163-4169.

100. H. A. Bicalho, P. R. Donnarumma, V. Quezada-Novoa, H. M. Titi and A. J. Howarth, *Inorg. Chem.*, 2021, **60**, 11795-11802.

101. A. J. Howarth, A. W. Peters, N. A. Vermeulen, T. C. Wang, J. T. Hupp and O. K. Farha, *Chem. Mater.*, 2017, **29**, 26-39.

102. H. Al-Kutubi, J. Gascon, E. J. R. Sudhölter and L. Rassaei, *ChemElectroChem*, 2015, **2**, 462-474.

103. M. Li and M. Dincă, *J. Am. Chem. Soc.*, 2011, **133**, 12926-12929.

104. M. Klimakow, P. Klobes, A. F. Thünemann, K. Rademann and F. Emmerling, *Chem. Mater.*, 2010, **22**, 5216-5221.

105. S. L. James, C. J. Adams, C. Bolm, D. Braga, P. Collier, T. Friščić, F. Grepioni, K. D. M. Harris, G. Hyett, W. Jones, A. Krebs, J. Mack, L. Maini, A. G. Orpen, I. P. Parkin, W. C. Shearouse, J. W. Steed and D. C. Waddell, *Chem. Soc. Rev.*, 2012, **41**, 413-447.

106. P. J. Beldon, L. Fábián, R. S. Stein, A. Thirumurugan, A. K. Cheetham and T. Friščić, *Angew. Chem. Int. Ed.*, 2010, **49**, 9640-9643.

107. T. Friščić, *Chem. Soc. Rev.*, 2012, **41**, 3493-3510.

108. T. Friščić, D. G. Reid, I. Halasz, R. S. Stein, R. E. Dinnebier and M. J. Duer, *Angew. Chem. Int. Ed.*, 2010, **49**, 712-715.

109. K. Užarević, T. C. Wang, S.-Y. Moon, A. M. Fidelli, J. T. Hupp, O. K. Farha and T. Friščić, *Chem. Commun.*, 2016, **52**, 2133-2136.

110. N. A. Khan and S. H. Jhung, *Coord. Chem. Rev.*, 2015, **285**, 11-23.

111. J. Klinowski, F. A. Almeida Paz, P. Silva and J. Rocha, *Dalton Trans.*, 2011, **40**, 321-330.

112. B. Zheng, H. Dong, J. Bai, Y. Li, S. Li and M. Scheer, *J. Am. Chem. Soc.*, 2008, **130**, 7778-7779.

113. R. Seetharaj, P. V. Vandana, P. Arya and S. Mathew, *Arab. J. Chem.*, 2019, **12**, 295-315.

114. S. C. McKellar, A. J. Graham, D. R. Allan, M. I. H. Mohideen, R. E. Morris and S. A. Moggach, *Nanoscale*, 2014, **6**, 4163-4173.

115. R. Wei, C. A. Gaggioli, G. Li, T. Islamoglu, Z. Zhang, P. Yu, O. K. Farha, C. J. Cramer, L. Gagliardi, D. Yang and B. C. Gates, *Chem. Mater.*, 2019, **31**, 1655-1663.

116. M. Köppen, V. Meyer, J. Ångström, A. K. Inge and N. Stock, *Cryst. Growth Des.*, 2018, **18**, 4060-4067.

117. M. Ahmadi, S. M. Ayyoubzadeh, F. Ghorbani-Bidkorbeh, S. Shahhosseini, S. Dadashzadeh, E. Asadian, M. Mosayebnia and S. Siavashy, *Heliyon*, 2021, **7**, e06914-e06914.

118. H. Li, M. Eddaoudi, T. L. Groy and O. M. Yaghi, *J. Am. Chem. Soc.*, 1998, **120**, 8571-8572.

119. J. E. Mondloch, O. Karagiaridi, O. K. Farha and J. T. Hupp, *CrystEngComm*, 2013, **15**, 9258-9264.

120. A. P. Nelson, O. K. Farha, K. L. Mulfort and J. T. Hupp, *J. Am. Chem. Soc.*, 2009, **131**, 458-460.

121. K. D. M. Harris, M. Tremayne and B. M. Kariuki, *Angew. Chem. Int. Ed.*, 2001, **40**, 1626-1651.

122. D. D. Le Pevelen, in *Encyclopedia of Spectroscopy and Spectrometry (Second Edition)*, ed. J. C. Lindon, Academic Press, Oxford, 2010, pp. 2559-2576.

123. C. F. Holder and R. E. Schaak, *ACS Nano*, 2019, **13**, 7359-7365.

124. S. Øien-Ødegaard, G. C. Shearer, D. S. Wragg and K. P. Lillerud, *Chem. Soc. Rev.*, 2017, **46**, 4867-4876.

125. K. Sing, *Colloid Surf. A-Physicochem. Eng. Asp.*, 2001, **187-188**, 3-9.

126. M. Thommes, K. Kaneko, A. V. Neimark, J. P. Olivier, F. Rodriguez-Reinoso, J. Rouquerol and K. S. W. Sing, *Pure Appl. Chem.*, 2015, **87**, 1051-1069.

127. M. Thommes, *Chem. Ing. Tech.*, 2010, **82**, 1059-1073.

128. S. Brunauer, P. H. Emmett and E. Teller, *J. Am. Chem. Soc.*, 1938, **60**, 309-319.

129. J. I. Goldstein, D. E. Newbury, P. Echlin, D. C. Joy, A. D. Romig, C. E. Lyman, C. Fiori and E. Lifshin, in *Scanning Electron Microscopy and X-Ray Microanalysis: A Text for Biologists, Materials Scientists, and Geologists*, eds. J. I. Goldstein, D. E. Newbury, P. Echlin, D. C. Joy, A. D. Romig, C. E. Lyman, C. Fiori and E. Lifshin, Springer US, Boston, MA, 1992, pp. 671-740.

130. I. M. Klotz, *J. Chem. Educ.*, 1945, **22**, 328.

131. L. Yang and S. J. Miklavcic, *J. Opt. Soc. Am. A*, 2005, **22**, 1866-1873.

132. J. Yang, W. Ni, B. Ruan, L.-C. Tsai, N. Ma, D. Shi, T. Jiang and F.-C. Tsai, *ECS J. Solid State Sci. Technol.*, 2021, **10**, 056003.

133. S. Kuno, H. Akeno, H. Ohtani and H. Yuasa, *Phys. Chem. Chem. Phys.*, 2015, **17**, 15989-15995.

134. D. L. Dexter, *J. Chem. Phys.*, 1953, **21**, 836-850.

135. T. Förster, *Ann. Phys.*, 1948, **437**, 55-75.

136. W. Cao, Y. Tang, Y. Cui and G. Qian, *Small Structures*, 2020, **1**, 2000019.

137. E. G. Moore, A. P. S. Samuel and K. N. Raymond, *Acc. Chem. Res*, 2009, **42**, 542-552.

138. I. Obodovskiy, in *Radiation*, ed. I. Obodovskiy, Elsevier, 2019, pp. 207-220.

139. M. D. Allendorf, C. A. Bauer, R. K. Bhakta and R. J. T. Houk, *Chem. Soc. Rev.*, 2009, **38**, 1330-1352.

140. C. Janiak, *Dalton Trans.*, 2003.

141. M. Zhu, Z.-M. Hao, X.-Z. Song, X. Meng, S.-N. Zhao, S.-Y. Song and H.-J. Zhang, *Chem. Commun.*, 2014, **50**, 1912-1914.

142. R. Medishetty, V. Nalla, L. Nemec, S. Henke, D. Mayer, H. Sun, K. Reuter and R. A. Fischer, *Adv. Mater.*, 2017, **29**, 1605637.

143. R. C. Leif, L. M. Vallarino, M. C. Becker and S. Yang, *Cytometry Part A*, 2006, **69A**, 767-778.

144. J.-C. G. Bünzli and C. Piguet, *Chem. Soc. Rev.*, 2005, **34**, 1048-1077.

145. S. I. Weissman, *J. Chem. Phys.*, 1942, **10**, 214-217.

146. M. Latva, H. Takalo, V.-M. Mukkala, C. Matachescu, J. C. Rodríguez-Ubis and J. Kankare, *J. Lumin.*, 1997, **75**, 149-169.

147. M. J. Neufeld, A. Lutzke, G. Pratx and C. Sun, *Chemistry*, 2021, **27**, 3229-3237.

148. H. Liu, H. Qin, N. Shen, S. Yan, Y. Wang, X. Yin, X. Chen, C. Zhang, X. Dai, R. Zhou, X. Ouyang, Z. Chai and S. Wang, *Angew. Chem. Int. Ed.*, 2020, **59**, 15209-15214.

149. C. A. Bauer, T. V. Timofeeva, T. B. Settersten, B. D. Patterson, V. H. Liu, B. A. Simmons and M. D. Allendorf, *J. Am. Chem. Soc.*, 2007, **129**, 7136-7144.

150. S. R. Mathis Ii, S. T. Golafale, J. Bacsa, A. Steiner, C. W. Ingram, F. P. Doty, E. Auden and K. Hattar, *Dalton Trans.*, 2017, **46**, 491-500.

151. C. Wang, O. Volotskova, K. Lu, M. Ahmad, C. Sun, L. Xing and W. Lin, *J. Am. Chem. Soc.*, 2014, **136**, 6171-6174.

152. J. J. Perry Iv, P. L. Feng, S. T. Meek, K. Leong, F. P. Doty and M. D. Allendorf, *J. Mater. Chem.*, 2012, **22**, 10235-10248.

153. M. J. Neufeld, H. Winter, M. R. Landry, A. M. Goforth, S. Khan, G. Pratx and C. Sun, *ACS Appl. Mater. Interfaces*, 2020, **12**, 26943-26954.

154. X. Wang, Y. Wang, Y. Wang, H. Liu, Y. Zhang, W. Liu, X. Wang and S. Wang, *Chem. Commun.*, 2020, **56**, 233-236.

155. R. Pode, *Renew. Sust. Energ. Rev.*, 2020, **133**, 110043.

156. D. F. de Souza, P. P. F. da Silva, L. F. A. Fontenele, G. D. Barbosa and M. de Oliveira Jesus, *Energy Rep.*, 2019, **5**, 409-424.

157. A. Bergh, G. Craford, A. Duggal and R. Haitz, *Phys. Today*, 2001, **54**, 42-47.

158. J. Cho, J. H. Park, J. K. Kim and E. F. Schubert, *Laser Photonics Rev.*, 2017, **11**, 1600147.

159. T. Taguchi, *J. Light Vis. Environ.*, 2003, **27**, 131-139.

160. P. Pust, P. J. Schmidt and W. Schnick, *Nat. Mater.*, 2015, **14**, 454-458.

161. J. W. Stinson, *US Pat.*, US6600175B1, 1991, 992.

162. A. Mills, *III-Vs rev.*, 2005, **18**, 32-34.

163. S. Tabuchis, *Japanese Pat.*, S50-79379, 1973.

164. Y. Shimizu, *Japanese Pat.*, H08-7614, 1996.

165. C. S. McCamy, *Color Res. Appl.*, 1992, **17**, 142-144.

166. Y. Yang, M. Lowry, C. M. Schowalter, S. O. Fakayode, J. O. Escobedo, X. Xu, H. Zhang, T. J. Jensen, F. R. Fronczek, I. M. Warner and R. M. Strongin, *J. Am. Chem. Soc.*, 2006, **128**, 14081-14092.

167. S. Mukherjee and P. Thilagar, *Dyes Pigm.*, 2014, **110**, 2-27.

168. Y. Yang, L. Chen, F. Jiang, M. Yu, X. Wan, B. Zhang and M. Hong, *J. Mater. Chem. C.*, 2017, **5**, 1981-1989.

169. Y. Wang, J. Ding, Y. Wang, X. Zhou, Y. Cao, B. Ma, J. Li, X. Wang, T. Seto and Z. Zhao, *J. Mater. Chem. C.*, 2019, **7**, 1792-1820.

170. P. Coppo, M. Duati, V. N. Kozhevnikov, J. W. Hofstraat and L. De Cola, *Angew. Chem. Int. Ed.*, 2005, **44**, 1806-1810.

171. M. J. Bowers, J. R. McBride and S. J. Rosenthal, *J. Am. Chem. Soc.*, 2005, **127**, 15378-15379.

172. Y. Hu, X. Liang, D. Wu, B. Yu, Y. Wang, Y. Mi, Z. Cao and Z. Zhao, *J. Mater. Chem. C.*, 2020, **8**, 734-741.

173.   J. Cornil, D. Beljonne, J. P. Calbert and J. L. Brédas, *Adv. Mater.*, 2001, **13**, 1053-1067.

174.   F. So, J. Kido and P. Burrows, *MRS Bull.*, 2008, **33**, 663-669.

175.   F. Serpaggi and G. Férey, *J. Mater. Chem.*, 1998, **8**, 2737-2741.

176.   M.-S. Wang, S.-P. Guo, Y. Li, L.-Z. Cai, J.-P. Zou, G. Xu, W.-W. Zhou, F.-K. Zheng and G.-C. Guo, *J. Am. Chem. Soc.*, 2009, **131**, 13572-13573.

177.   M.-S. Wang, G.-C. Guo, W.-T. Chen, G. Xu, W.-W. Zhou, K.-J. Wu and J.-S. Huang, *Angew. Chem. Int. Ed.*, 2007, **46**, 3909-3911.

178.   D. F. Sava, L. E. S. Rohwer, M. A. Rodriguez and T. M. Nenoff, *J. Am. Chem. Soc.*, 2012, **134**, 3983-3986.

179.   J. He, M. Zeller, A. D. Hunter and Z. Xu, *J. Am. Chem. Soc.*, 2012, **134**, 1553-1559.

180.   C.-Y. Sun, X.-L. Wang, X. Zhang, C. Qin, P. Li, Z.-M. Su, D.-X. Zhu, G.-G. Shan, K.-Z. Shao, H. Wu and J. Li, *Nat. Commun.*, 2013, **4**, 2717.

181.   C. Peng, X. Song, J. Yin, G. Zhang and H. Fei, *Angew. Chem. Int. Ed.*, 2019, **58**, 7818-7822.

182.   L. Qiu, C. Yu, X. Wang, Y. Xie, A. M. Kirillov, W. Huang, J. Li, P. Gao, T. Wu, X. Gu, Q. Nie and D. Wu, *Inorg. Chem.*, 2019, **58**, 4524-4533.

183.   S. Dang, J.-H. Zhang and Z.-M. Sun, *J. Mater. Chem.*, 2012, **22**, 8868-8873.

184.   K. Liu, H. You, Y. Zheng, G. Jia, Y. Huang, M. Yang, Y. Song, L. Zhang and H. Zhang, *Cryst. Growth Des.*, 2010, **10**, 16-19.

185.   R. Peña-Rodríguez, J. A. Molina-González, H. Desirena-Enrriquez, E. Armenta-Jaime, J. M. Rivera and S. E. Castillo-Blum, *J. Mater. Chem. C.*, 2021.

186.   L. H. Slooff, A. Polman, S. I. Klink, L. Grave, F. C. J. M. van Veggel and J. W. Hofstraat, *J. Opt. Soc. Am. B*, 2001, **18**, 1690-1694.

187.   A. Dhakshinamoorthy, A. Santiago-Portillo, A. M. Asiri and H. Garcia, *ChemCatChem*, 2019, **11**, 899-923.

188.   A. Shaabani, R. Mohammadian, S. E. Hooshmand, A. Hashemzadeh and M. M. Amini, *ChemistrySelect*, 2017, **2**, 11906-11911.

189.   Y. Jiao, Y. Liu, G. Zhu, J. T. Hungerford, S. Bhattacharyya, R. P. Lively, D. S. Sholl and K. S. Walton, *J. Phys. Chem. C*. 2017, **121**, 23471-23479.

190. S. Chavan, J. G. Vitillo, D. Gianolio, O. Zavorotynska, B. Civalleri, S. Jakobsen, M. H. Nilsen, L. Valenzano, C. Lamberti, K. P. Lillerud and S. Bordiga, *Phys. Chem. Chem. Phys.*, 2012, **14**, 1614-1626.

191. X. Yang, Z. Li and S. Tang, *Cryst. Growth Des.*, 2021, **21**, 6092-6100.

192. P. R. Donnarumma, S. Frojmovic, P. Marino, H. A. Bicalho, H. M. Titi and A. J. Howarth, *Chem. Commun.*, 2021, **57**, 6121-6124.

193. M. H. V. Werts, R. T. F. Jukes and J. W. Verhoeven, *Phys. Chem. Chem. Phys.*, 2002, **4**, 1542-1548.

194. G. Deng, *Nat. Chem.*, 2018, **10**, 110-110.

195. D. Briones, P. Leo, J. Cepeda, G. Orcajo, G. Calleja, R. Sanz, A. Rodríguez-Diéguez and F. Martínez, *CrystEngComm*, 2018, **20**, 4793-4803.

196. T. Tachikawa, J. R. Choi, M. Fujitsuka and T. Majima, *J. Phys. Chem. C*. 2008, **112**, 14090-14101.

197. S. Bordiga, C. Lamberti, G. Ricchiardi, L. Regli, F. Bonino, A. Damin, K. P. Lillerud, M. Bjorgen and A. Zecchina, *Chem. Commun.*, 2004.

198. J.-K. Cheng, P.-X. Yin, Z.-J. Li, Y.-Y. Qin and Y.-G. Yao, *Inorg. Chem. Commun.*, 2007, **10**, 808-810.

199. W. Chen, J.-Y. Wang, C. Chen, Q. Yue, H.-M. Yuan, J.-S. Chen and S.-N. Wang, *Inorg. Chem.*, 2003, **42**, 944-946.

200. H.-Q. Yin, X.-Y. Wang and X.-B. Yin, *J. Am. Chem. Soc.*, 2019, **141**, 15166-15173.

201. Z. Ajoyan, G. A. Mandl, P. R. Donnarumma, V. Quezada-Novoa, H. A. Bicalho, H. M. Titi, J. A. Capobianco and A. J. Howarth, *Chem Rxiv*, 2021.

202. D. Parker, *Coord. Chem. Rev.*, 2000, **205**, 109-130.

203. Y. Zhang, W. Thor, K.-L. Wong and P. A. Tanner, *J. Phys. Chem. C*. 2021, **125**, 7022-7033.

204. M. W. Mara, D. S. Tatum, A.-M. March, G. Doumy, E. G. Moore and K. N. Raymond, *J. Am. Chem. Soc.*, 2019, **141**, 11071-11081.

205. A. N. Carneiro Neto, R. T. Moura, A. Shyichuk, V. Paterlini, F. Piccinelli, M. Bettinelli and O. L. Malta, *J. Phys. Chem. C*. 2020, **124**, 10105-10116.

206. Y. Zhang, S. Yuan, G. Day, X. Wang, X. Yang and H.-C. Zhou, *Coord. Chem. Rev.*, 2018, **354**, 28-45.

207. J. Liu, Y. Zhuang, L. Wang, T. Zhou, N. Hirosaki and R.-J. Xie, *ACS Appl. Mater. Interfaces*, 2018, **10**, 1802-1809.

208. D.-H. Chen, A. E. Sedykh, G. E. Gomez, B. L. Neumeier, J. C. C. Santos, V. Gvilava, R. Maile, C. Feldmann, C. WÖll, C. Janiak, K. Müller-Buschbaum and E. Redel, *Adv. Mater. Interfaces*, 2020, **7**, 2000929.

209. H. Liu, H. Qin, N. Shen, S. Yan, Y. Wang, X. Yin, X. Chen, C. Zhang, X. Dai, R. Zhou, X. Ouyang, Z. Chai and S. Wang, *Angew. Chem. Int. Ed.*, 2020, **59**, 15209-15214.

210. Y. Wang, X. Liu, X. Li, F. Zhai, S. Yan, N. Liu, Z. Chai, Y. Xu, X. Ouyang and S. Wang, *J. Am. Chem. Soc.*, 2019, **141**, 8030-8034.

211. J. S. Klein, C. Sun and G. Pratx, *Phys. Med. Biol.*, 2019, **64**, 04TR01.

212. F. Maddalena, L. Tjahjana, A. Xie, Arramel, S. Zeng, H. Wang, P. Coquet, W. Drozdowski, C. Dujardin, C. Dang and M. D. Birowosuto, *Crystals*, 2019, **9**.

213. H. Furukawa, K. E. Cordova, M. O'Keeffe and O. M. Yaghi, *Science*, 2013, **341**, 1230444.

214. D. T. de Lill and C. L. Cahill, *Chem. Commun.*, 2006.

215. V. Kiritsis, A. Michaelides, S. Skoulika, S. Golhen and L. Ouahab, *Inorg. Chem.*, 1998, **37**, 3407-3410.

216. Y. Wang, L. Feng, W. Fan, K.-Y. Wang, X. Wang, X. Wang, K. Zhang, X. Zhang, F. Dai, D. Sun and H.-C. Zhou, *J. Am. Chem. Soc.*, 2019, **141**, 6967-6975.

217. Y. Cui, Y. Yue, G. Qian and B. Chen, *Chem. Rev.*, 2012, **112**, 1126-1162.

218. T. C. Wang, N. A. Vermeulen, I. S. Kim, A. B. F. Martinson, J. F. Stoddart, J. T. Hupp and O. K. Farha, *Nat. Protoc.*, 2016, **11**, 149-162.

219. G. Sheldrick, *Acta Crystallogr. A*, 2015, **71**, 3-8.

220. G. Sheldrick, *Acta Crystallogr. Sect. C Struct. Chem.*, 2015, **71**, 3-8.

221. A. Spek, *Acta Crystallogr. Sect. C Struct. Chem.*, 2015, **71**, 9-18.

222. A. J. Howarth, PhD Thesis, University of British Columbia, 2014.

223. R. G. Surbella III, K. P. Carter, T. D. Lohrey, D. Reilly, M. Kalaj, B. K. McNamara, J. Schwantes and R. J. Abergel, *Chem. Eur. J.*, 2020, **26**, 13819-13825.

224. G. Tessitore, S. L. Maurizio, T. Sabri and J. A. Capobianco, *Angew. Chem. Int. Ed.*, 2019, **58**, 9742-9751.

225. D. F. Parra, A. Mucciolo and H. F. Brito, *J. Appl. Polym. Sci.*, 2004, **94**, 865-870.

226. D. Ananias, A. D. G. Firmino, R. F. Mendes, F. A. A. Paz, M. Nolasco, L. D. Carlos and J. Rocha, *Chem. Mater.*, 2017, **29**, 9547-9554.

227. M. L. Taylor, R. L. Smith, F. Dossing and R. D. Franich, *Med Phys*, 2012, **39**, 1769-1778.

228. M. Kleinerman, *J. Chem. Phys.*, 1969, **51**, 2370-2381.

229. B. S. Santos, C. de Mello Donegá and G. F. de Sá, *J. Lumin.*, 1997, **72-74**, 535-537.

230. B. S. Santos, C. de Mello Donegá, G. F. de Sá, L. F. C. de Oliveira and P. S. Santos, *Spectrochim. Acta A Mol. Biomol. Spectrosc.*, 1998, **54**, 2237-2245.

231. G. F. de Sá, O. L. Malta, C. de Mello Donegá, A. M. Simas, R. L. Longo, P. A. Santa-Cruz and E. F. da Silva, *Coord. Chem. Rev.*, 2000, **196**, 165-195.

232. E. Caballero-Mancebo, B. Cohen, S. Smolders, D. E. De Vos and A. Douhal, *Adv. Sci.*, 2019, **6**, 1901020.

233. M. Gutierrez, B. Cohen, F. Sánchez and A. Douhal, *Phys. Chem. Chem. Phys.*, 2016, **18**, 27761-27774.

234. P. Deria, J. Yu, T. Smith and R. P. Balaraman, *J. Am. Chem. Soc.*, 2017, **139**, 5973-5983.

235. F. P. Kinik, A. Ortega-Guerrero, D. Ongari, C. P. Ireland and B. Smit, *Chem. Soc. Rev.*, 2021, **50**, 3143-3177.

236. S. P. Vila-Nova, G. A. L. Pereira, R. Q. Albuquerque, G. Mathis, H. Bazin, H. Autiero, G. F. d. Sá and S. Alves, *J. Lumin.*, 2004, **109**, 173-179.

Appendix

Single Crystal X-Ray Diffraction (SCXRD) Analysis

Table A.1. Crystallographic data for Tb-UiO-66, Tb-CU-27, Tb(F)-UiO-66, Tb(F)-CU-10, and Tb(F)-CU-27.

Identification code	Tb-UiO-66	Tb-CU-27	Tb(F)-UiO-66	Tb(F)-CU-10	Tb(F)-CU-27
CSD numbers	2120961	2120959	2120962	2120963	2120960
Empirical formula	$C_{24}H_{12}O_{16}Tb_3$	$C_{17}H_9O_{5.33}Tb_{1.49}$	$C_{24}H_{12}F_4O_{12}Tb_3$	$C_{68}H_{36}F_4O_{18}Tb_{4.59}$	$C_{17}H_9F_{1.33}O_4Tb_{1.49}$
Formula weight	1033.10	535.28	1045.10	1946.96	539.33
Temperature/K	298(2)	298(2)	298(2)	298(2)	298(2)
Crystal system	cubic	trigonal	cubic	trigonal	trigonal
Space group	Fm-3m	P-3m1	Fm-3m	P-3m1	P-3m1
a/Å	21.5263(4)	22.0489(5)	21.5263(4)	22.0962(6)	22.0489(5)
b/Å	21.5263(4)	22.0489(5)	21.5263(4)	22.0962(6)	22.0489(5)
c/Å	21.5263(4)	12.5603(3)	21.5263(4)	16.7081(5)	12.5603(3)
α/°	90	90	90	90	90
β/°	90	90	90	90	90
γ/°	90	120	90	120	120
Volume/Å^3	9974.9(6)	5288.2(3)	9974.9(6)	7064.7(4)	5288.2(3)
Z	8	6	8	2	6
ρ_{calc}g/cm^3	1.376	1.009	1.392	0.915	1.016
μ/mm^{-1}	20.943	14.672	21.005	11.399	14.704
F(000)	3832.0	1503.0	3864.0	1845.0	1511.0
2Θ range for data collection/°	7.112 to 144.43	9.262 to 145.498	7.112 to 144.43	8.002 to 146.058	9.262 to 145.498
Index ranges	-26 ≤ h ≤ 26, -25 ≤ k ≤ 26, -26 ≤ l ≤ 26	-27 ≤ h ≤ 27, -27 ≤ k ≤ 22, -15 ≤ l ≤ 15	-26 ≤ h ≤ 26, -25 ≤ k ≤ 26, -26 ≤ l ≤ 26	-26 ≤ h ≤ 27, -27 ≤ k ≤ 27, -20 ≤ l ≤ 20	-27 ≤ h ≤ 27, -27 ≤ k ≤ 22, -15 ≤ l ≤ 15
Reflections collected	51261	86090	51251	54311	86055
Independent reflections	556 [R_{int} = 0.1629, R_{sigma} = 0.0200]	3800 [R_{int} = 0.1066, R_{sigma} = 0.0338]	555 [R_{int} = 0.1629, R_{sigma} = 0.0200]	5053 [R_{int} = 0.0471, R_{sigma} = 0.0234]	3797 [R_{int} = 0.1066, R_{sigma} = 0.0338]
Data/restraints/parameters	556/0/27	3800/31/178	555/0/27	5053/260/212	3797/30/178
Goodness-of-fit on F^2	1.030	1.088	1.065	1.073	1.077
Final R indexes [I>=2σ (I)]	R_1 = 0.0618, wR_2 = 0.1760	R_1 = 0.0590, wR_2 = 0.1504	R_1 = 0.0384, wR_2 = 0.1027	R_1 = 0.0313, wR_2 = 0.0909	R_1 = 0.0569, wR_2 = 0.1402
Final R indexes [all data]	R_1 = 0.0800, wR_2 = 0.2856	R_1 = 0.0821, wR_2 = 0.1768	R_1 = 0.0589, wR_2 = 0.1399	R_1 = 0.0345, wR_2 = 0.0939	R_1 = 0.0802, wR_2 = 0.1650

Largest diff. peak/hole / e Å⁻³	5.54/-1.46	2.05/-0.86	1.31/-0.82	1.91/-0.80	1.89/-0.84
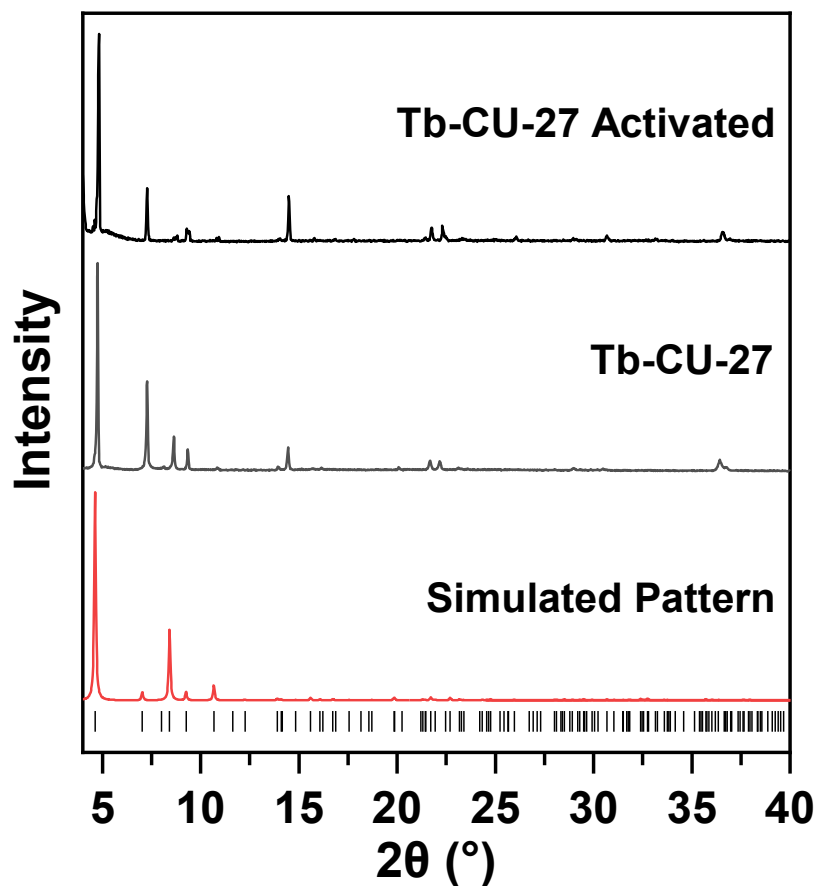
Figure A.2. Powder X-ray diffraction (PXRD) patterns of simulated, as-synthesized, and activated Tb-CU-27.
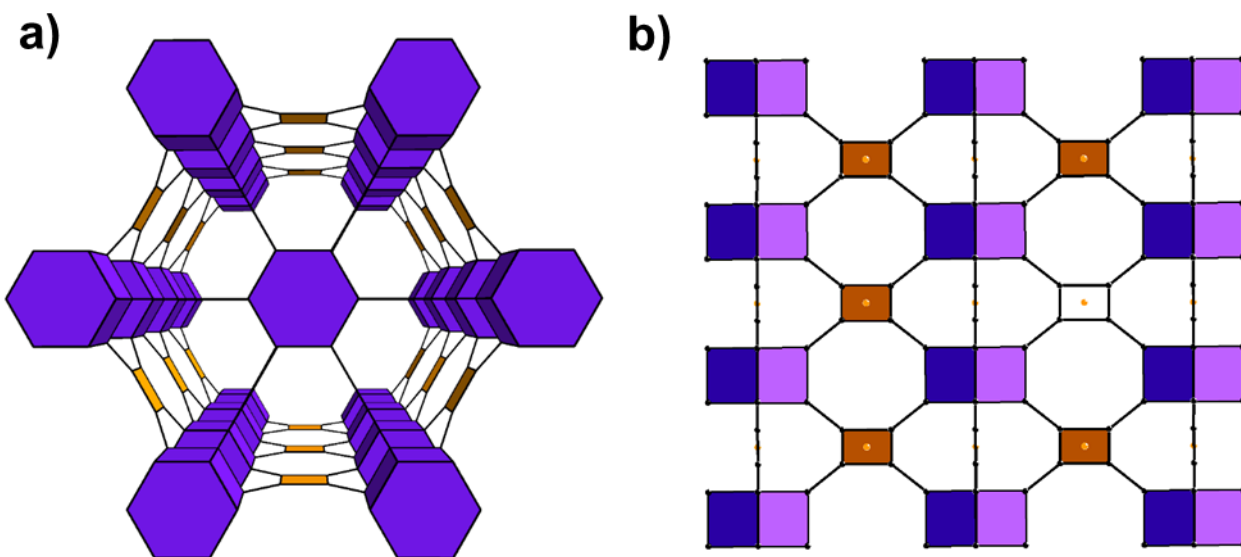
Figure A.2. Representation of **shp** topology of Tb-CU-27 (a) down the c-axis, highlighting the d6R nonanuclear cluster nodes (purple hexagonal prisms) and (b) down the a-axis, highlighting the d6R nonanuclear cluster nodes (purple hexagonal prisms).
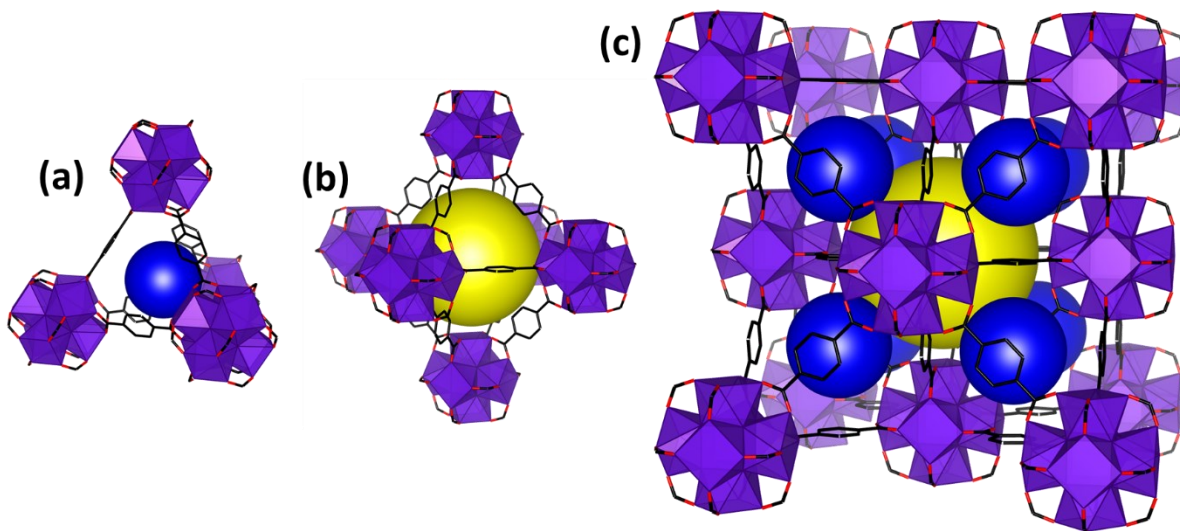
Figure A.3. Structure of Tb-UiO-66 depicting the (a) tetrahedral cage (blue sphere), (b) octahedral cage (yellow sphere) and (c) **fcu** net.
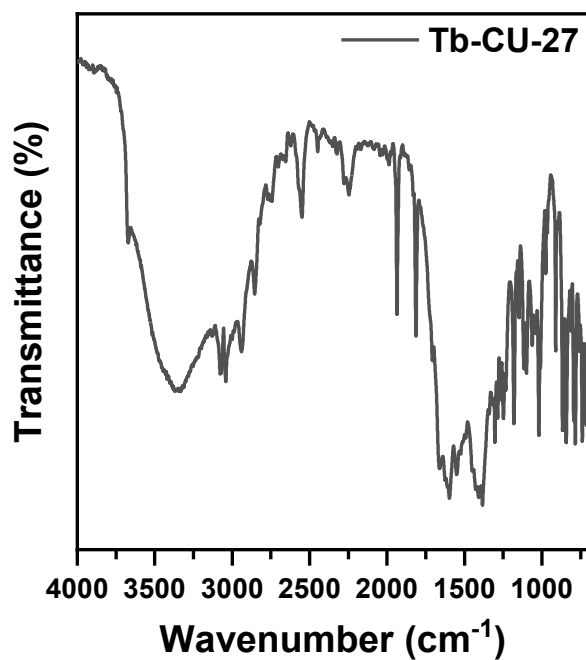
Figure A.4. Diffuse reflectance infrared Fourier transform spectrum of Tb-CU-27 with peaks at 1390 and 1595 cm^{-1} corresponding to the carbonyl group of the organic linker, at 3675 cm^{-1} corresponding to the bridging -OH group in the Tb$_9$-cluster node, a broad stretch centered around 3350 cm^{-1} due to residual water, and stretches from 3080-2840 cm^{-1} corresponding to C-H groups of the organic linker.
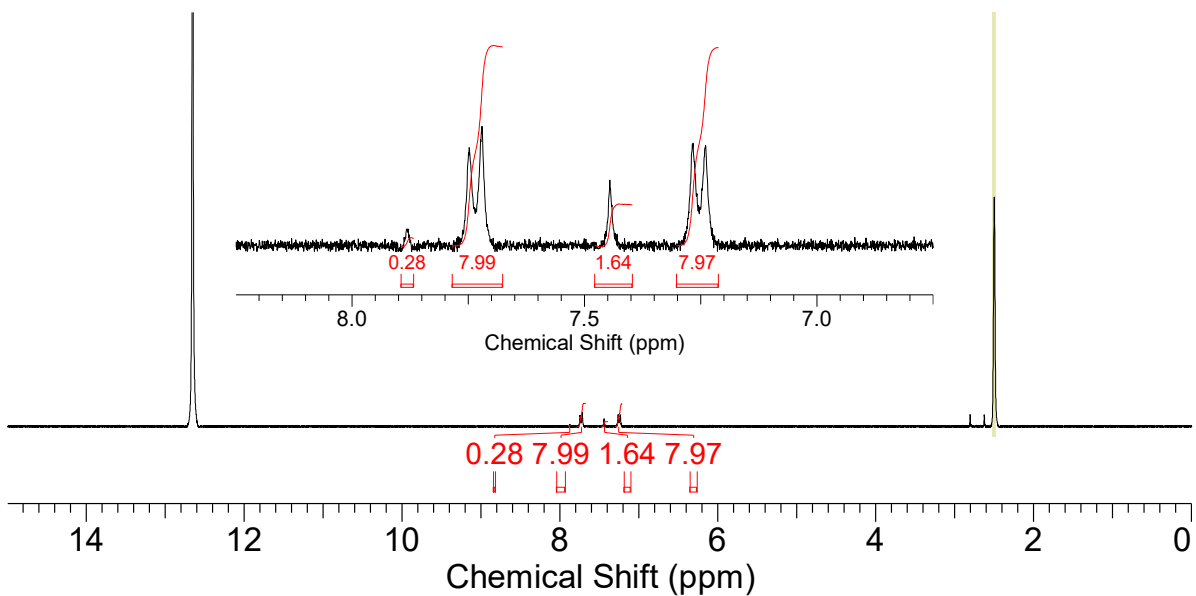
Figure A.5. ^{1}H-NMR spectrum of Tb-CU-27 digested using 10 drops of D_2SO_4 and solubilized in DMSO-d_6.
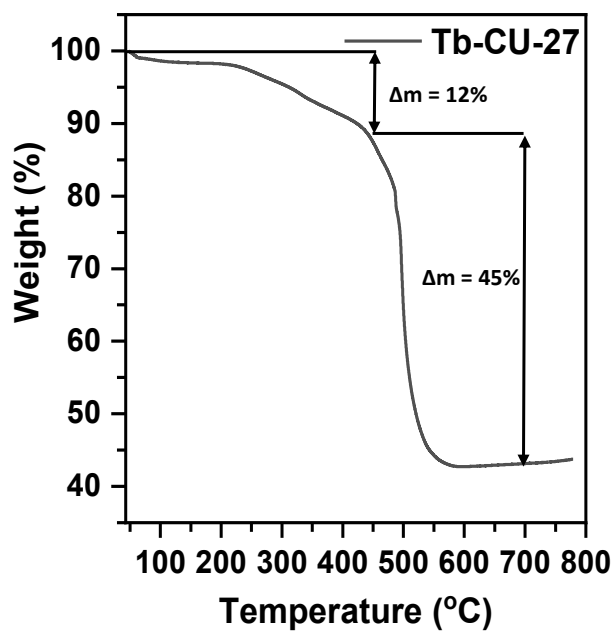
Figure A.6. Thermogravimetric analysis (TGA) data for Tb-CU-27 showing a residual mass of 43% corresponding to Tb_2O_3.
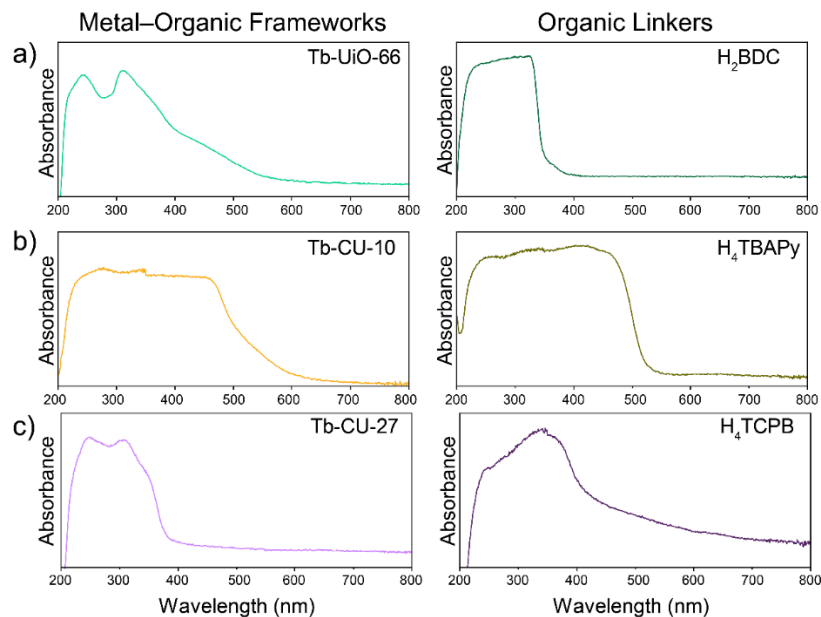
Figure A.7. Diffuse reflectance UV-Vis spectrum of (a) Tb-UiO-66 and H_2BDC (b) Tb-CU-10 and H_4TBAPy (c) Tb-CU-27 and H_4TCPB showing π to π^* absorptions of the organic linkers.
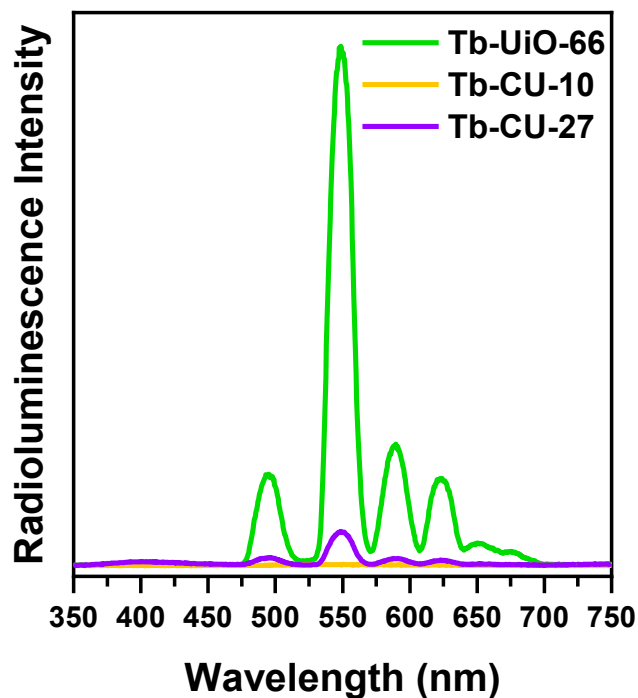
Figure A.8. Radioluminescence emission intensities of Tb-UiO-66 (green), Tb-CU-10 (yellow) and Tb-CU-27 (purple) under identical detection conditions for comparison of luminescence intensities. All spectra performed under X-ray excitation (50 kVp, 80 µA, Au target, unfiltered beam).
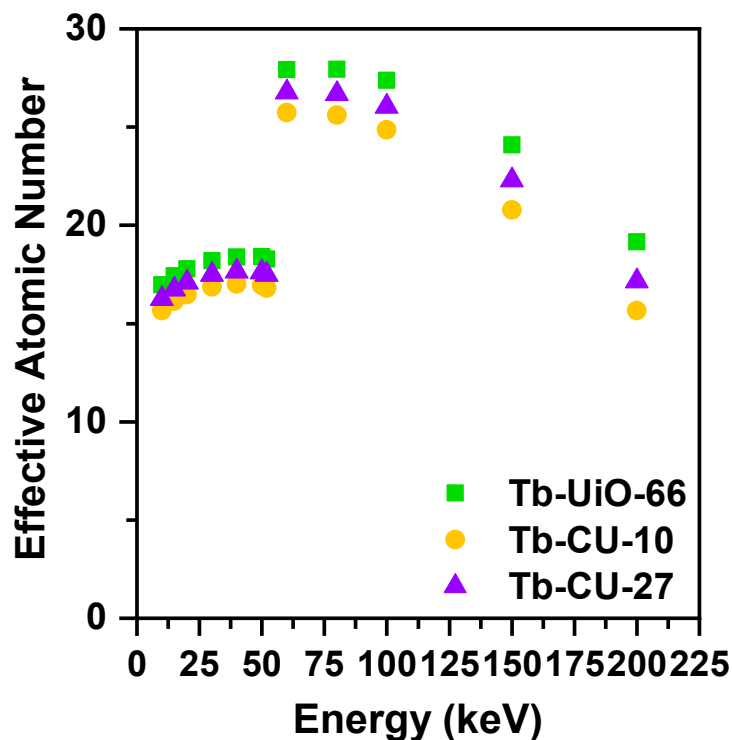
Figure A.9. Spectrum-weighted effective atomic number (Z_{eff}) of Tb-UiO-66 (green), Tb-CU-10 (yellow), and Tb-CU-27 (purple) as a function of energy in keV based on a 50 kVp INTRABEAM source. Data generated using Auto-Zeff software.[227]

Table A.2. Spectrum-weighted effective atomic number (Z_{eff}) and mean Z_{eff} of Tb-UiO-66, Tb-CU-10, Tb-CU-27, and as a function of energy in keV based on a 50 kVp INTRABEAM source. Data generated using Auto-Zeff software.[227]

MOF	Spectrum Weighted Zeff	Mean Zeff
Tb-UiO-66	17.0519	16.0550
Tb-CU-10	15.7765	14.8477
Tb-CU-27	16.3731	15.4111
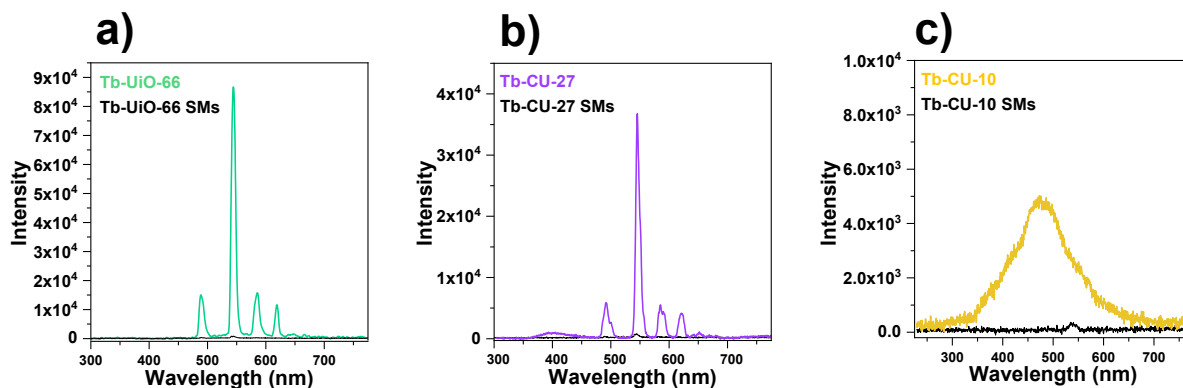
Figure A.10. Radioluminescence emission intensities of starting material mixtures for Tb-CU-27 (purple), Tb-CU-10 (yellow), Tb-UiO-66 (green), and Tb(NO$_3$)$_3$•xH$_2$O (black) under X-ray excitation (50 kVp, 80 μA, Au target, unfiltered beam). Starting materials were gently mixed around with a spatula with the following quantities for Tb-UiO-66, Tb-CU-10 and Tb-CU-27.

Tb(NO$_3$)$_3$•xH$_2$O (0.0348 mmol, 75.5 mg), H$_2$BDC (0.0.342 mmol, 5.7 mg)

Tb(NO$_3$)$_3$•xH$_2$O (0.0294 mmol, 63.8 mg), H$_4$TBAPy (0.00734 mmol, 5.0 mg)

Tb(NO$_3$)$_3$•xH$_2$O (0.01474 mmol, 6.4 mg), H$_4$TCPB (0.00358 mmol, 2.0 mg)
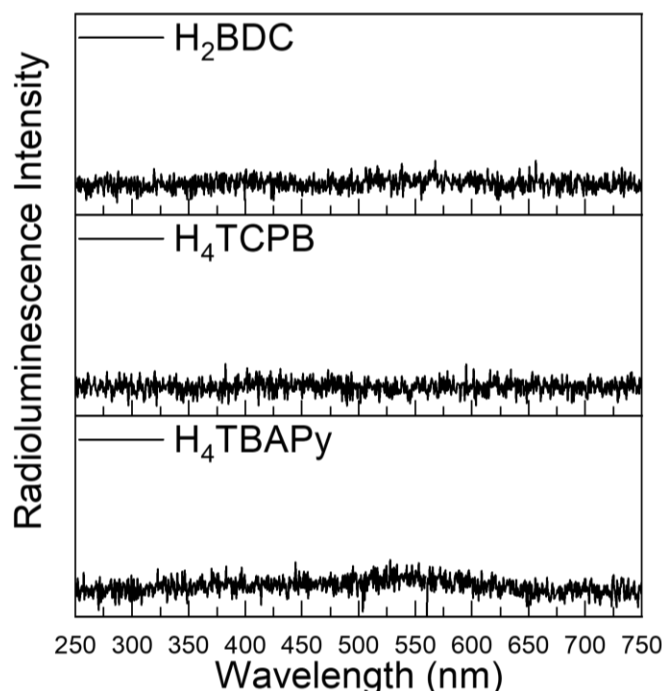
Figure A.11. Radioluminescence emission intensities of H$_2$BDC, H$_4$TBAPy, and H$_4$TCPB under X-ray excitation (50 kVp, 80 μA, Au target, unfiltered beam).